Final Report

Novel High-Temperature Proton and Mixed-Proton Electron Conductors for Fuel Cells and H_2-Separation Membranes

Maryia Ivanova, Sandrine Ricote, Habibur Rhaman, Morten Huse and Reidar Haugsrud

August 2011

Participants:

Centre for Materials Science and Nanotechnology, Dept. of Chemistry, FERMIO, University of Oslo, Norway.
Principal investigators: Prof. Truls Norby and Assoc. Prof. Reidar Haugsrud;
Employed as PhD student: Morten Huse

Sintef Materials and Chemistry, Dept. of Energy Conversion and Materials, Norway
Principal investigator: Dr. Yngve Larring

Risø National Laboratory, Technical University of Denmark
Principal investigator: Dr. Nikolaos Bonanos;
Employed Post doc.: Dr. Sandrine Ricote

Chalmers University of Technology, Sweden,
Pri,cipal investigator: Prof. Sten Eriksson;
Employed as Ph.D studet: Sheik Habibur Rhaman

Research Centre Jülich GmbH, Germany
Principal investigator: Dr. Wilhelm Meulenberg;
Employed Post doc.: Dr. Mariya Ivanova

Steering commitee: Norby (UiO), Larring (Sintef), Bonanos (Risø-DTU), Eriksson (CTH) and Meulenberg (FZ-Jülich)

Novel High-Temperature Proton and Mixed-Proton Electron Conductors for Fuel Cells and H_2-Separation Membranes

Maryia Ivanova, Sandrine Ricote, Habibur Rhaman, Morten Huse and Reidar Haugsrud
Department of Chemistry, University of Oslo, FERMiO, Gaustadalléen 21, NO-0349 Oslo, Norway
reidarha@kjemi.uio.no

Key words: Energy technology; Fuel cells, gas separation membranes, proton conductors, mixed proton electron conductors, hydration thermodynamics, transport parameters,

Abstract:

Focus in the present project has been to develop high-temperature proton and mixed proton electron conductors for solid oxide fuel cells and hydrogen gas separation membranes. Various oxidic materials have been synthesized and their transport properties characterized with emphasis on effects of protons. Materials within the series of rare-earth niobates and tungstates, perovskite structured alkaline earth cerates-zirconates, metallic perovskites, and silicates have been investigated. The transport properties of the rare-earth niobates were sought optimized by means of acceptor doping on the A- and B-site, as well as, with co-doping on both the A and B-site. It was shown that the solubility of acceptors in the system is low and do not exceed 1 mol%. Physico chemical parameters representing the conductivity behavior of the different materials were extracted by fitting models derived from point defect chemistry and transport theory to the conductivity data. The maximum in proton and mixed proton-electron conductivity was x and a respectively. These are values that require thin films in the order of 1 to 10 μm of the materials to be applied as the core component in any of the abovementioned processes. Empirical relations between the thermodynamic and transport parameters derived and physical and chemical properties of the materials under investigation have been obtained. These are invaluable to increase the fundamental understanding of functional properties and to search for material candidates with improved behavior.

Contributions from principal investigators and co-workers in other related projects, as well as, the financial support from the national financial agencies, are gratefully acknowledged.

Executive summary:

High temperature proton conductors and mixed proton-electron conductors have potential to become important components in future clean and efficient energy technologies. This may either be as an electrolyte membrane in a Proton Ceramic Fuel Cell (PCFC) converting chemical energy to electricity or as a hydrogen gas separation membranes e.g. producing CO_2-free H_2 from natural gas or in processes related to conversion of natural gas to added-value chemicals. Challenges in the development of these technologies have been to derive materials that combine the required functional properties with sufficient chemical and mechanical stability. New classes of proton conductors, rare earth niobates and tantalates ($LnNbO_4$ and $LnTaO_4$) and tungstates (Ln_6WO_{12}) with improved stability in CO_2 were uncovered and published around 2006-7. However, the maximum proton conductivities of these were still lower than for the best alkaline-earth cerate and zirconate based perovskites, typically 0.0005 to 0.005 S/cm. Consequently, thin membranes are required to reach the targeted area specific resistance of 0.1 Ωcm^2 for application in high-drain processes. The major focus in the present project has been to improve the performance of these niobates and tungstate based proton conductors and the properties of the alkaline-earth perovskites, and moreover, to develop and investigate novel high temperature proton and mixed proton electron conductors. The present project, "Novel High-Temperature Proton and Mixed-Proton Electron Conductors for Fuel Cells and H_2-Separation Membranes**",** was granted through the first call of the Northern European Innovative Energy Research (N-INNER, 2007), a consortium coordinated by University of Oslo (Norway) with Chalmers University of Technology (Sweden), Risø-DTU (Denmark), FZ-Jülich (Germany) and Sintef (Norway) as the other partners.

The principal objective has been to improve the transport properties of compounds within the rare-earth niobates/tantalates and tungstates through optimized traditional acceptor doping and novel schemes for co-doping on A and B sites of the materials. In addition, several perovskite structured materials were studied with emphasis on compounds within the solid solubility range of the system $BaCeO_3$-$BaZrO_3$. In addition, novel metallic perovskite materials were investigated for mixed ionic electronic conductivity. A family of silicates was given attention early in the project as some reports in literature indicated promising proton conductivity. Overall, the experimental and theoretical approaches were designed so as to strengthen the understanding of the relation between structural and functional properties of the materials investigated.

The various ternary oxides have been synthesized according to either solid state reaction or wet chemical routes. Depending on the purpose of the fabrication, different treatments were applied to the powders. Ink and slurry recipes were developed for the film deposition during the in-situ solid state transformation approach. For characterization of bulk and grain boundary properties of the materials, conventional high temperature sintering was applied. The composition and structure of the materials under investigation were characterized by means of the extensive facilities available to the partners within the consortium. Notably, one of the partners actively pursue development of novel structural in situ characterization with high flux neutron source at the ISIS beam line for reaction conditions representing solid oxide fuel cell operating conditions. The functional properties of the materials have been investigated primarily by determining the materials electrical properties as a function of temperature under controlled atmospheres of oxygen- and water vapor partial pressures. The effects of protons have been elucidated by shifting between hydrogen and deuterium containing atmospheres, e.g. by shifting from H_2O to D_2O. Partial conductivities have been extracted from the EMF method. Computational approaches by Density Functional Theory (DFT) and Reverse Monte Carlo simulations (RMC) have been implemented.

The structure and transport properties of several A-, B- and A- and B-site co doped $LaNbO_4$ based materials (A=Ca, Sr, and Ba; B= Ti, In, Ga, Ge) were characterized as a function of reaction conditions. The solubility limit of the acceptors in the materials was concluded to be low based on the insignificant change in the lattice parameters as a function of increasing doping level and, moreover, from observations of secondary phases with microscopy. The reason for the low acceptor solubility in these materials is that formation of the charge compensating defect occurs by coalescence of several tetrahedral NbO_4 units, a process which requires relatively high energy. This has been concluded based on DFT approaches and has also been verified by means of neutron diffraction studies. The conductivity behavior of the materials was interpreted by means of models based on point defect chemistry developed and adapted for ABO_4 materials with tetrahedral moieties. On basis of the relatively strong temperature dependence of the conductivity, in particular for materials with B-site doping, it was concluded that association between the acceptor and protons and oxygen vacancies, forming a neutral defect complex, strongly influences the transport properties of the materials. To derive thermodynamic and transport parameters representing the behavior of the system, formalism taking also these defect associates into account was derived. The proton trajectories have been discussed in view of computational and neutron diffraction results.

Another material in the ABO_4 family, $LaVO_4$, was for the first time recognized as a high temperature proton conductor. Also for this material some of the La was substituted with lower valent Ca ions to increase the concentration of effectively charged defects. The material was an essentially pure ionic conductor. Thermodynamic and transport parameters were derived following the same approach as for the niobates.

Increasing the fundamental understanding of the processes which determine the functional properties of materials, physicochemical data are invaluable and where relations between physical and chemical properties are sought correlated empirically. In the present project this was done for ABO_4 (A=La and B= Nb, Ta, P, V, and As) materials with relatively similar structures. No correlation was encountered for the hydration thermodynamics, but it was shown that the enthalpy of mobility for protons increases with the volume of the B-site tetrahedral units, from 55 kJ/mol for $LaNbO_4$ to 95 kJ/mol for $LaPO_4$.

Among the perovskite structured materials, the relative influence of the different charge carries was determined in order to evaluate their potential to be used as electrolyte materials in SOFCs. Several of the materials exhibit relatively high proton conductivity and show promise in future fuel cell technologies. Notably, for some of the materials within the $BaZr_{1-x}Ce_xO_3$ based system (acceptor doped) improved fabrication routes were worked out by adding small amounts of Ni to enhance the sintering properties of the materials. It was found that the Ni addition does not change the conductivity characteristics of the material. For the perovskites it was successfully fabricated films of thickness in the order of 10 μm by means of the solid state reaction approach. One of the most challenging tasks taken on in the project was to look for ionic conductivity in some metallic perovskites. Membrane tests are the only way to measure ionic conduction in these materials, which will require specimens with a relative density above 93%. This has so far not been accomplished.

Several compositions in the family of silicates that was claimed to exhibit considerably high temperature proton conductivity was tried synthesized with several approaches. However, single-phase materials were not obtained, neither was any of the promising behavior of these materials reproduced.

Lanthanum tungstate related materials are presently under heavy investigation worldwide due to its interesting and promising properties as a high temperature proton and mixed proton electron conduction properties. Along in the present N-INNER project this material has been in focus and we have taken an important part in elucidating the materials structure by in situ ND studies at ISIS, and through characterizing the hydrogen flux. Probably most importantly these measurements have contributed to understand and relate the materials structure and point defect structure. Lanthanum tungstate now is the major electrolyte candidate in the present EU-FP7, EffiPro, and is and will be the bases in several forth coming applications, nationally as well as for present and coming EU calls.

In Norway, the present project has been one in a cluster of project, with the objective to develop proton ceramic fuel cells. Also the previously mentioned EU project was initiated and got funding with 4 out of the 5 N-INNER partners present. The synergy between, all these projects, and, in particular the two international ones, has been particularly fruitful. Several joint project meetings have been organized, also including more workshop-like sessions with invited tutorial lectures. The "N-INNER Symposium on High Temperature Proton and Mixed Proton Electron was organized by the coordinator, UiO, at Storaas Gjestegård near Kongsberg, from April 12- 15, 2010. The event had approximately 60 attendees from all over Europe and counting 20 oral presentations approximately the same number of posters it became a success. In addition also sessions with project meetings were organized.

The spin-off, Protia AS, was started in Norway early 2008, jointly by the UiO and NTNU, with the purpose to commercialize research based on high-temperature proton conductors and mixed proton electron conductors. $LaNbO_4$ and lanthanum tungstate based materials have been, and still are, important to technologies where Protia has interest. The insight gained through the present project has as such been very valuable to Protia as a potential end user of the technology.

Overall the scientific insight obtained in the present project has, first and foremost, contributed to increase the fundamental comprehension of the functional properties of the materials under investigation. The importance of acceptor doping has been shown and the difficulties of doping materials with tetrahedral moieties in ABO_4 compounds are addressed. It was found that the solubility limit in these materials is low and, moreover, that the B-site acceptor forms complexes with the charge carriers, decreasing the conductivity. Consequently, there is an optimal level of acceptor doping. For the $LaNbO_4$ system this level is as low as 0.3-0.5 mol % on the A-site and probably even lower at the B-site. Important relations between the materials functional and physical and chemical properties have been derived that will contribute significantly as a basis to derive new materials with improved properties. The level of conductivity reached for the materials investigated still requires relatively thin membranes, in the order of 1 to 10 μm, to be applied as components under high drain applications. This is challenging from a fabrication point of view, and approaches such as "in-situ solid state transformation" therefore become particularly valuable.

The present project has been important to establish the potential of materials in the rare-earth ortho-niobate for PCFC electrolyte membranes. A low solubility of acceptors and an apparent association between these acceptors and the proton have made us conclude that development of these materials for technological application will probably be too challenging. On bases of the improved understanding of structural and functional characteristics of the rare-earth tungstates, the interest in this class of materials has increased and generating patents and new projects and applications for new projects among the partners in the present N-INNER project and also at other research institutions around Europe.

The present project has educated two PhDs and trained two post docs/researchers. One of the PhDs will be defended on September 13, 2011, whereas the second one will be defended in 2012-13 due to late start and 4 years PhD period. Results from the project have been, and will be, actively presented to the international scientific community. So far this has and will (based on working titles) resulted in 11 posters, 24 oral presentations, and 21 papers in peer reviewed international journals. An international workshop was organized within the framework of the project gathering more than 50 scientists within the field of solid state protonics from all over Europe.

Table of Contents

1. INTRODUCTION

Proton Conducting Solid Oxide Fuel Cells, PC-SOFC, have important advantages compared to other fuel cell alternatives. Where fuel cells with electrolytes of polymers (e.g., Nafion), solid acids (e.g. $CsHSO_4$), and oxide ion conducting oxides (YSZ), face major challenges with respect to stability, electrode kinetics, overall efficiency, and expensive electrode materials, PC-SOFCs offer possible solutions to all of these. Chemical stability of the electrolyte materials has been the major show stopper for commercial realization of PC-SOFCs using state-of-the-art proton conductors such as Y-doped $BaCeO_3$. However, new materials have recently been identified combining the required mechanical and chemical properties and with appreciable high temperature proton conductivity

1.1. High-temperature Proton Conducting SOFC (PC-SOFC) – the "Turbo" SOFC

Ceramic proton conductors work in the temperature range 300 to 1000 °C, generally reaching a maximum in the proton conductivity between 400 and 800 °C. These materials are truly solid which enable higher operating temperature of PC-SOFCs than for Polymer Electrolyte- and the Solid Acids Fuel Cells (PEMFC and SAFC), but still lower than the traditional SOFCs. This makes the design of the overall assembly and choice of materials in the fuel cells easier. The most important advantages of PC-SOFCs compared to conventional SOFCs, however, rest on the fundamentally different working principles: In PC-SOFCs, protons migrate through the electrolyte from the anode to the cathode, react with oxygen and form water. That water forms at the cathode and not at the anode as for a conventional SOFC is important. Firstly because the dilution of the fuel at the anode is avoided, and secondly, that the anode environment remains reducing and independent of the fuel cell load. Absence of fuel dilution and the possibility to operate under higher loads without jeopardizing the anode, yield potentially higher efficiency and maximum power for PC-SOFCs, the "Turbo" SOFC.

1.2. Ceramic H_2 separation membranes

Hydrogen separation and production are technologies that will require further development if hydrogen is going to be the main future energy carrier. This is one important focus within membrane science, and several potential routes are followed. Just as ceramic proton conductors in PC-SOFCs will be important to the processes of converting hydrogen as fuel to electricity, they also have potential to play a major role in hydrogen production and purification. Provided that the ceramic also conducts electrons or electron holes, ambipolar transport of protons and electrons gives rise to a net hydrogen flux under gradients in the chemical potential of hydrogen. Materials that combine these two functional properties are, therefore, candidates for dense hydrogen gas separation membranes. The advantages of these membranes compared to other alternatives (microporous silica- or Ag-Pd-based membranes) are 100 % selectivity and stability to higher operating temperatures. Today there are only a hand-full of materials possessing these properties.

1.3. "Novel High-Temperature Proton and Mixed-Proton Electron Conductors for Fuel Cells and H_2-Separation Membranes" – Prospects of the project

New classes of proton conductors, rare earth niobates and tantalates ($LnNbO_4$ and $LnTaO_4$) and tungstates (Ln_6WO_{12}) with improved stability in CO_2 was uncovered by one of the partners in the project and published around 2006 [1, 2]. The maximum proton conductivities of these compounds were still lower than for the best perovskites, typically 0.005 S/cm or less, requiring very thin membranes to reach the target-area-specific resistance for application in high-drain technologies of 0.1 Ωcm^2. On this basis the focus in the project was a concerted effort to improve the performance of, in particular these niobates and tungstates, but also other chemically stable candidates with perovskite related structure.

The principal objective of this N-INNER project has been to develop CO_2-stable HTPC and HTMPEC membranes for fuel cells and H_2 separation membranes with area specific proton or ambipolar resistances below 0.1 Ωcm^2. The approach has been to improve the transport properties of compounds within the rare-earth niobates/tantalates and tungstates through optimized traditional acceptor doping and novel schemes for co-doping on A and B sites. Moreover, developing novel routes for thin, dense films on porous substrates of the new classes of the HTPC and HTMPEC materials has been focus.

Experimental and theoretical approaches have been designed so as to strengthen the understanding of the relation between structural and functional properties of the high-temperature proton conductors investigated. One aim has been to develop in-situ neutron and X-ray powder diffraction on bulk systems and on designed electrochemical cells under fuel cell simulated conditions.

The Scandinavian countries and Germany (MPI-Stuttgart and FZ Jülich) have always been in the lead in HTPCs internationally, together with a handful of groups in USA, Japan, and Russia. The present project has been unique in that it brought together the undisputed four centers of excellence in North-Europe when it comes to the combination of fuel cells, gas separation membranes, and proton conductors: UiO, SINTEF, Risø-DTU and FZ-Jülich all represent pioneers and leaders in HTPC research, and have complementary expertise in transport characterization, H_2 membrane technology, SOFC analysis and testing, and thin film fabrication. The Swedish group from Chalmers entered more recently with high quality work on structure and dynamics of HTPCs based on experimental and computational studies.

The focus on optimizing membrane transport properties was complementary to national and EU projects in which electrode development, interconnects, stability, and cost were emphasized. It has also been important to raise the critical mass of research supporting Protias AS (spin-off established early 2008) efforts to commercialize HTPCs. The project has been important in contributing to increase the knowledge transfer between the partners and to strengthen the high international standing of the northern European countries within energy related solid state ionics - and high temperature proton conductors in particular. Instruments to realize this was the hosting of an international symposium on HTPC and HTMPEC within the framework of the project, and to promote mobility of researcher between the partners. When all partners finish their project period, two PhDs will have been educated and two post docs trained within the project and also playing as important contributors in the framework on complementary projects with national and international partners.

1.4. Choice of materials

As briefly touched upon during the introduction, state-of-the-art high temperature proton conductors are troubled with reactivity towards CO_2 and a relatively high grain boundary resistivity. This limits the use of proton conductors as electrolytes in solid oxide fuel cells. Moreover, very few materials are available combining proton conductivity with sufficient electronic conductivity to induce decent hydrogen fluxes under operation as a hydrogen gas separation membrane. On this basis the UiO group in 2000-1 evaluated more than 200 materials and ranked them based on available literature and empirical relations expected to result in proton and mixed proton electron conductivity. The top candidates were studied in projects preceding the N-INNER call. Several promising classes of materials were uncovered, and the two top candidates, rare-earth niobates and rare-earth tungstates, were chosen as “core” materials for the N-INNER project. The aim was to improve their conductivity properties and also to reach a more complete understanding of their transport properties.

In addition to these two classes of oxides, materials in the solid solubility range between $BaCeO_3$ and $BaZrO_3$ has been in focus. These compounds show better stability and relatively lower grain boundary resistances than their parent oxides.

Brownmillerites are another interesting class of materials where some compositions in the system B-site substituted barium indate, $Ba_2In_2O_5$ e.g. ref [3] have been reported with high proton conductivity at temperatures below 500°C and with alleged chemical stability. In this project Ti and Sc substituted materials were synthesized and investigated.

Silica is one of the most abundant oxides on earth and, accordingly, present everywhere. Silica impurities have been blamed as a potential reason for blocking the grain boundaries to ionic transport as siliceous phases often are observed along interphases and grain boundaries. In 2002, J.M. Porras-Vàzquez *et al.* [4, 5] and A.G. De la Torre *et al.* [6] reported a new class of oxide ion conductors based on tricalcium oxy-silicate Ca_3SiO_5 (called C_3S in the cement nomenclature), and that the conductivity increases with additions of water vapor showing effects of protons. With silica as the one of the most abundant oxides and also, generally, being a challenge to avoid during fabrication with silica containing heating elements yielding detrimental effects on functional properties on non-silicon containing materials, a silica based functional material would be ideal. The aim here was to, based on the material of the Spanish group, find a stable subsituted C_3S compounds, with high oxygen defiency and symmetry to increase, respectively, the proton concentration and mobility.

Probably the most high risk part of the project was to try to determine the ionic transport of some perovskite related metallic oxides. These are oxides with extremely high electronic conductivity and whether they possess any ionic contribution was yet to be established. The reason for this is the difficulty to characterize minor partial ionic conductivities by means of standard methods, and flux measurements are probably the best alternative. Within the project, there have been (still on-going) an activity on the structural and functional properties of one class of metallic perovskites, with emphasis on potential effects of protons.

2. METHODOLOGY and EXPERIMENTAL PROCFEDURE

The following section describes some of the experimental approaches used as standard techniques in the project. **In-situ solid state transformation approach** is described more thoroghly in the appendix, since this novel approach was implemented to grow thin films for some of the proton conductors under discussion.

2.1. Powder Synthesis and fabrication of ceramics for characterization of transport properties

The materials have been synthesized according to either the solid state reaction route or by means of wet chemical complexation methods.

In the solid state reaction route powders of the parent oxides (precursors) of a compound are intimately mixed by milling. The mixture is then heat-treated (calcined) at high temperature upon which the materials react to form the desired product. The product is examined by powder X-Ray Diffraction. In case there are residual parent oxides or secondary phases present, remilling followed by new heat treatment and milling steps are repeated until a single phase product is obtained.

In the wet chemical methods, the parent oxides are instead dissolved and the solutions are mixed together. The cations are stabilized in solution with an organic complexing agent, e.g. citric acid or EDTA, or a combination of the two. The fact that the cations are in solution promotes a well-mixed, homogenous distribution and, as such, a single-phase product. After stabilizing the cations together the solutions are slowly evaporated under the formation of a so-called XEROX-gel. This organic crispy sponge is heat treated at 4-600C to burn-off carbon. The next step is usually to calcine the material similarly as in the solid state method, but at a considerably lower temperature due to the already well mixed precursor). Verification of the products follows the same procedure as for the solid-state reaction synthesis route.

When PXRD shows a single-phase product the powders are usually compacted by pressing techniques and sintered at high temperatures (2/3 of melting temperature as guide-line). The sintering properties of the different powders vary and the ideal conditions to densify a ceramic green body are studied by dilatometry.

For more details on the synthesis routes, the reader should consult the specific papers listed in the appendix A.1.

2.2 Structural, microstructural and compositional characterization.

The structure, microstructure and chemical composition have been carefully monitored under all the different stages in the syntheses, the manufacturing of specimens for transport characterization, pre and post transport characterization. Within the framework of the consortium, virtually all relevant characterization techniques are available and consequently many of these have been used. Here we rest with just listing them and referring to more elaborate reviews and the individually published papers for concrete details. The following techniques have been applied : Powder X-rays Diffraction (PXRD), Neutron Diffraction (ND), Scanning Electron Microscopy (SEM), Energy Dispersive Spectroscopy (EDS), Electron Probe Micro Analysis (EPMA), High Resolution Transmission Electron Microscopy (HR-TEM), X-rays Photo Electron Spectroscopy (XPS), Secondary Ion Mass Spectrometry (SIMS), Impedance Spectroscopy, EMF measurements, Thermogravimetry (TG), Mass Spectrometry, Gas Chromatography, Raman Spectroscopy, Infra Red Spectroscopy etc.

In addition to the experimental approaches, there have also been major computational efforts in this and complementary projects where the personnel of the present project have been involved.

These approaches include packages based on DFT, Molecular Dynamics Simulations, Reverse Montecarlo Simulations, etc.

2.3 Conductivity characterization

The electrical conductivity of the materials has been extensively characterized and this technique certainly forms the basis for a major part of the results generated within the project. Several approaches have been followed in order to determine the materials transport properties.

Typically these measurements have been performed in a sample holder like the one illustrated in Figure 1 a ProboStat^{TM} (Norecs AS). With this assembly one may perform electrical characterization in controlled atmospheres at elevated temperatures. The Probostat's top part is placed in a vertical tube furnace where the temperature next to the specimen is controlled usually with an S-type thermocouple placed close to the sample. This thermocouple also controls the furnace system. A frequency response analyzer (e.g. SI 1260, Solartron) is connected to the sample either by four probes directly pressed down on the specimens surface, as for van der Pauw type measurements, or the voltage and current probes are connected to the porous Pt-electrodes in a 2-point (usually 4-wire) setup, as for the configuration in the schematics.

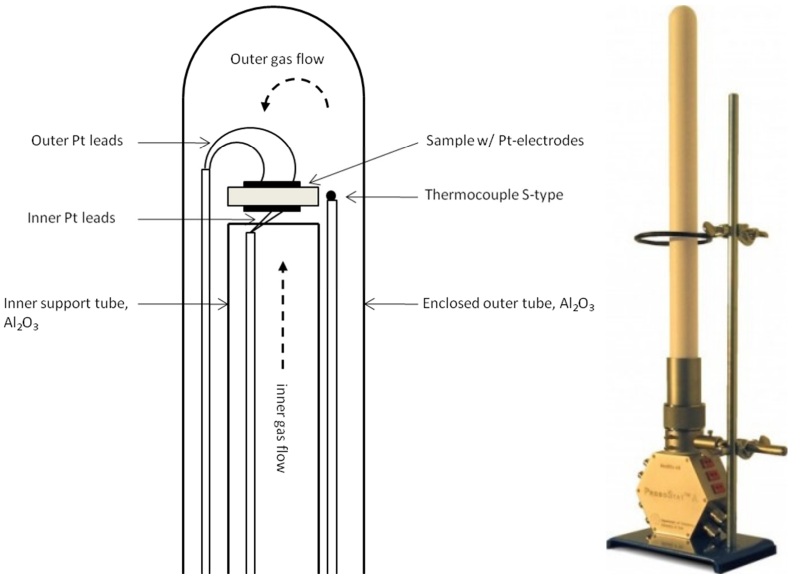

Figure 1. Left: Sketch of sample holder's top part. Right: Photo of ProboStat^{TM} sample holder used for all samples during electrical characterization (Photo: courtesy of NorECs AS). The spring load assembly, used to keep the sample fixed to the inner support tube, is omitted for better view of the key components.

Determination of partial conductivities has been accomplished by calculating transport numbers using the so-called EMF technique. Samples used for transport number measurements were sealed to the alumina support tube of the measurement cell with a gold gasket. Possible leakage between the two chambers was measured by a quadropole mass spectrometer. Since the chambers could be fed with different gas mixtures, gradients in well-defined p_{O_2} or p_{H_2O} were set up across the specimen and the resulting voltage measured. Solving the EMF equation with the voltage and gradients in a partial pressure as known parameters, the transport number of the charge carriers can be extracted.

The general EMF equation is given as:

$$E_{II-I} = \left[t_{O^{2-}} + t_{H^+} + t_{OH^-} + t_{H_3O^+}\right]\frac{RT}{4F}\ln\frac{p_{O2}^{II}}{p_{O2}^{I}} - \left[t_{H^+} - t_{OH^-} + 3t_{H_3O^+}\right]\frac{RT}{2F}\ln\frac{p_{H2O}^{II}}{p_{H2O}^{I}}$$

Where t_i is the transport number of species i, $p_{O_2}^{I}$ and $p_{O_2}^{I}$ are oxygen partial pressures and $p_{H_2O}^{I}$ and $p_{H_2O}^{II}$ are water vapor pressures in chambers I and II, e.g. the inner and outer chambers of the measurement cell.

Impedance spectroscopy has been widely used during the electrical characterization to separate the total conductivity into its contribution from bulk and grain boundaries. Modeling of the equivalent circuits has followed the standard procedures applying the so-called Brick-Layer model. For more input, the reader should consult the vast and complex literature on these measurement techniques in general, and the papers published from the project, for more specific interest.

2.4. The development of atmospheres for characterization of transport properties.

As seen from the sections above, it is essential during electrical characterization to control and, moreover, to have the possibility to vary the gas composition surrounding the specimen. This may be accomplished by mixing "reactive" and inert gases to vary the partial pressures of interest. There are several possible ways of doing this of which the one use mostly in this project is briefly described in A3.

2.5. H_2 flux measurements

There have been direct measurements of H_2 flux across rare-earth tungstate based materials. The experimental setup for flux measurements is very similar to the EMF setup except that there is no need for electrodes and the specimen is simply sealed to the alumina support tube. By feeding H_2 containing gases on one side and inert gas, Ar in our case, on the other side of the membrane, the flux of hydrogen from the feed side to the permeate side can be measured. The concentration of hydrogen in the permeate is determined using a micro-GC.

2.6. Development of Novel Methods for in-situ Structural Characterization

Insight to the materials structure is invaluable to understand the transport properties and how these vary with reaction conditions. However, routine structural investigations are performed at room temperature, and the room temperature structure does not necessarily represent the same actually present at high temperature under a given gas atmosphere. Consequently, it is desirable to do structural investigations in-situ, and even more so, simultaneously probing e.g. the conductivity of the material under investigation. In the present project an important accomplishment has been to take part in the development of such methodologies at the ISIS neutron spallation source in UK. We have been involved in the upgrade of the POLARIS neutron powder diffractometer and a suite of sample environment cells in order to carry out structure characterizing studies in the neutron beam as a function of temperature and oxygen partial pressure or humidity. Figure 2 shows the conductivity cell and gas-mixer developed to do these types of measurements along with an example of lattice parameter variations as a function of temperature.

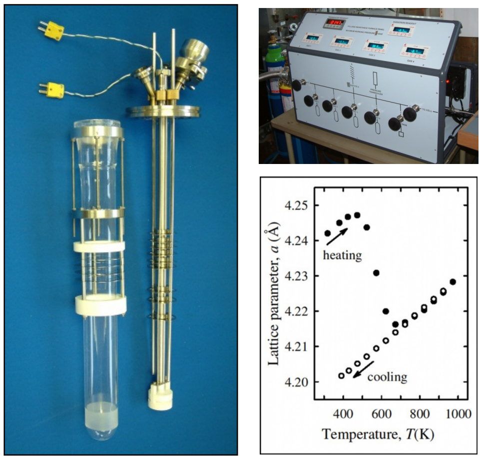

Figure 2. Left part shows a sample holder designed for in-situ neutron and conductivity measurements. In the upper right hand part a computer controlled gas mixer is presented and below we see examples of results from in-situ neutron diffraction.

Recent data has shown that unique *in-situ* studies can be performed in the neutron beam to study fuel cells materials under real working conditions and that this approach can be really valuable to the understanding of the materials behavior.

3. RESULTS and DISCUSSION.

As outlined during the previous sections the materials chosen to be focused in the project were among state-of-the art high temperature proton and mixed proton-electron conductors. The present paragraph treats some of the results and the most important discussion for the different materials studied. Only those results most relevant to the understanding of the materials behavior are included in the paragraphs. Details of some of the different studies are available in the publications listed in the Appendices.

3.1. Properties of some perovskites and perovskite related materials

3.1.1. Fabrication of dense alkaline-earth based cerate membranes via the In-situ solid state transformation route

The in-situ solid state transformation route was tested for Y-doped $BaCeO_3$, $SrCeO_3$ and $CaCeO_3$ membranes. The procedure making the powders and the processing of the different layers are described in A2. Here we will briefly show some results from the most successful manufacturing of Y-doped $BaCeO_3$ layers.

After powder synthesis and screen printing, described in the A2, laser topography was used to investigate the dried and sintered first layer of CeY10. Using these results, the average thickness was determined to ~15 µm. After sintering, the thickness was reduced to ~10 µm. There was also noticeable bending of the substrate. SEM cross-sectional micrographs are shown in Figure 3**.** The SEM images clearly show three distinct layers on top of the porous substrate. The top layer (I) corresponds to the screen printed CeY10 layer and it can be seen that although the layer is very porous, a uniform thickness and flat surface was achieved. The application of a thick layer on a pre-sintered substrate resulted in the electrolyte being sintered under constraint and this could be the reason for limited densification that occurred during the sintering. The second layer (II) is the gas tight 8YSZ layer which rests on top of the functional anode layer (III) composed of NiO and 8YSZ grains.

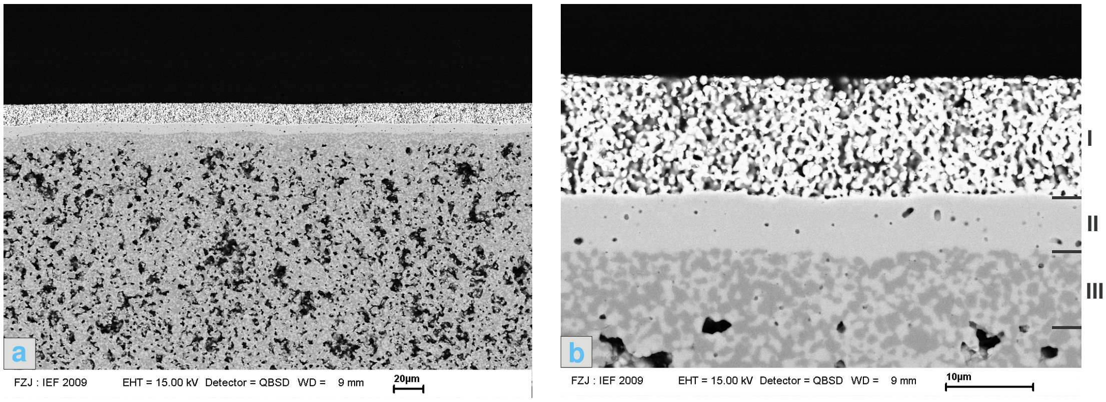

Figure 3 SEM cross-sections of sintered CeY10 first layer on NiO-8YSZ substrate

Figure 4 shows SEM cross-sectional micrographs of (a-b) sample BCY10-2020-YSZ and (c-d) BCY10-2040-YSZ. There are some noticeable cracks, however, these could have been formed when the samples were fractured before polishing. Four different regions are noticed on top of the porous NiO-8YSZ substrate. Section I is very dense and composed of $BaCe_{1-x}Y_xO_{3-\delta}$ with the x value most likely being approximately 0.10. It can be noticed that the first section becomes much thicker with an increased amount of $BaCO_3$ which could mean that there remains some unreacted BaO. Section I* is made up principally of the same composition as section I, but with Zr- enriched grains. The Zr enrichments originate from the extended diffusion from the YSZ layer. Section II in sample BCY10-2020-YSZ (Figure 4.) contains Ba, Ce and Zr and is most likely of the composition $BaCe_{1-x-y}Zr_xY_yO_{3-\delta}$ with the Ce- fraction decreasing towards the YSZ layer (III). These Zr-substituted barium cerates have shown greatly improved stability with only a minor decrease in conductivity and some future investigations should focus on the manufacture of these types of membranes. Section II in sample BCY10-2040-YSZ (Figure 4d) is much thicker and similarly composed exclusively of Y-doped $BaZrO_3$ which is most likely due to the larger amount of BaO available for reaction with the 8YSZ layer. Section III is composed of the remaining unreacted YSZ gas tight layer and again in section IV, the anode functional layer can be seen.

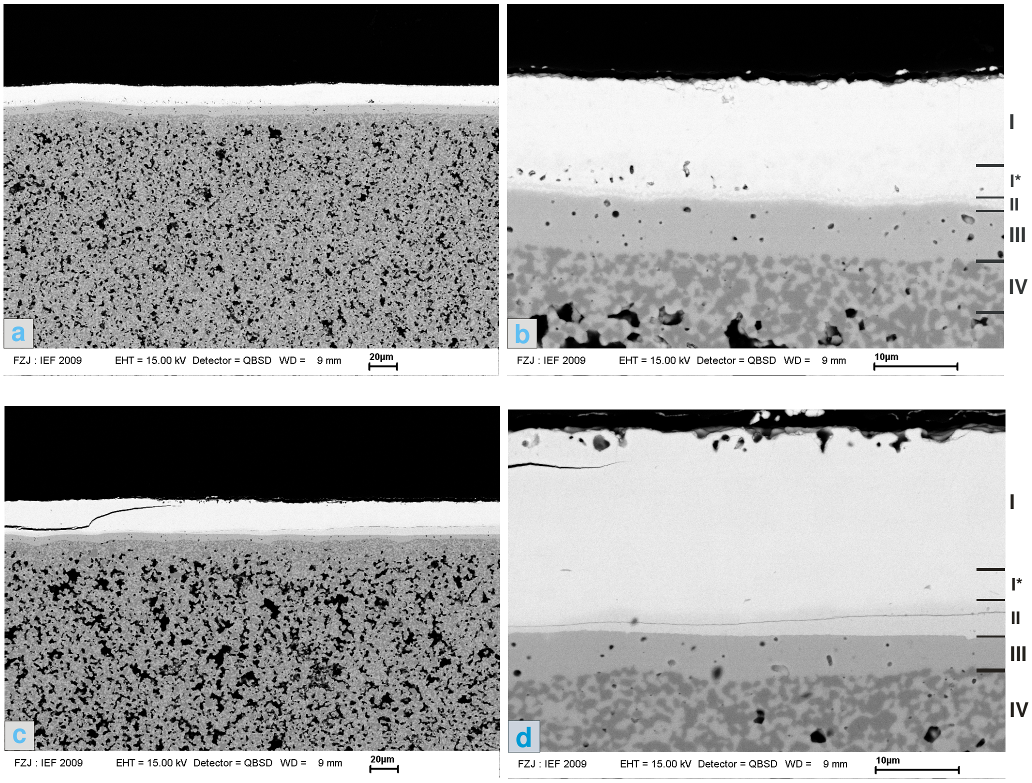

Figure 4 SEM micrographs of samples (a-b) BCY10-2020-YSZ and (c-d) BCY10-2040-YSZ

It is clear from both samples that the barium carbonate layers do react with the Y-doped ceria layer to form a dense thin layer. In both cases, the reaction continues into the Y-stabilized zirconia layer with the reaction going further in the sample with the thicker barium carbonate layer. The tolerance factors calculated for $BaCeO_3$ and $BaZrO_3$ were 0.95 and 1.00, respectively. The tolerances factors of both perovskite structures are clearly high enough that the BaO reacts readily with both the doped ceria and zirconia.

XRD analysis of the BCY10-2020-YSZ sample is shown in Figure 5(a) and it can be noted that no $BaCO_3$ or BaO were deteced leading one to believe that all of the available Ba was used for reaction with either the Y-doped ceria or zirconia (both of which were detected on the surface). In future research, adjustment of the layer thickness could result in a more precise stoichiometry and less extra-reaction with excess BaO.

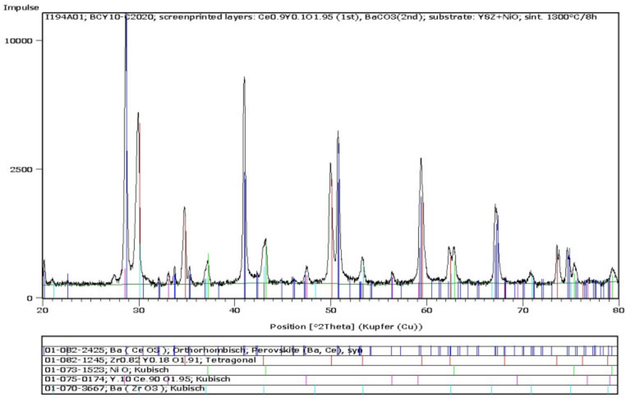

Figure 5. XRD analysis of samples BCY10-2020-YSZ

Since there was only success with $BaCeO_3$ based materials and these are relatively vulnerable towards reaction with CO_2 it was decided not to characterize the conductivity of any of these films within the framework of the project.

3.1.2. 50mol% Indium and Scandium doped $BaTiO_3$

Structural and functional properties of 50 mol% In and Sc doped $BaTiO_3$, i.e. $BaTi_{0.5}In_{0.5}O_{3-\delta}$ and $BaTi_{0.5}Sc_{0.5}O_{3-\delta}$ have been compared with an emphasis on the proton conducting properties. 50 mol% indium doped $BaTiO_3$ adopts a primitive cubic perovskite structure in comparison to the tetragonal $BaTiO_3$ and orthorhombic brownmillerite $Ba_2In_2O_5$. Thermogravimetric measurements of the materials upon exposure to high water vapour showed that the materials dissolve proton by hydration of oxygen vacancies, reaching approx. 57 % of the nominal level of oxygen vacancies. An example of a TG curve is presented in Figure 6.

The total conductivity increases significantly for both $BaTi_{0.5}In_{0.5}O_{3-\delta}$ and $BaTi_{0.5}Sc_{0.5}O_{3-\delta}$ under humid atmospheres in the low temperature region. This is illustrated in Figure 7 for $BaTi_{0.5}In_{0.5}O_{3-\delta}$. Also the effect on the conductivity of the H/D isotope shift shows that protons are the major charge carrier under wet conditions below ~500°C

The materials are shown to be stable within the temperature range of interest for fuel cell applications. Under oxidizing conditions p- type conductivity is noticed. The materials showed similar conductivity behaviour except that $BaTi_{0.5}Sc_{0.5}O_{3-\delta}$ had significantly higher total conductivity up to 600 °C than $BaTi_{0.5}In_{0.5}O_{3-\delta}$. $BaTi_{0.5}Sc_{0.5}O_{3-\delta}$ shows a total conductivity value of $1.31\cdot10^{-4}$ and $2.68\cdot10^{-4}$ Scm^{-1} at 300 °C and 600 °C, respectively. The scandium containing sample is the most promising candidate for future applications.

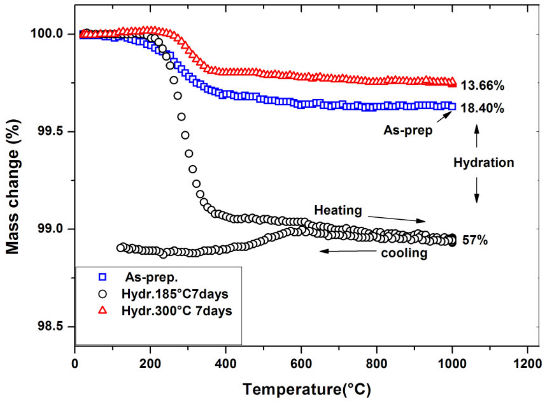

Figure 6. Comparison of TGA results under inert atmosphere of $BaTi_{0.5}In_{0.5}O_{3-\delta}$ *at various hydration conditions. % value is indicated for theoretical filling by protons.*

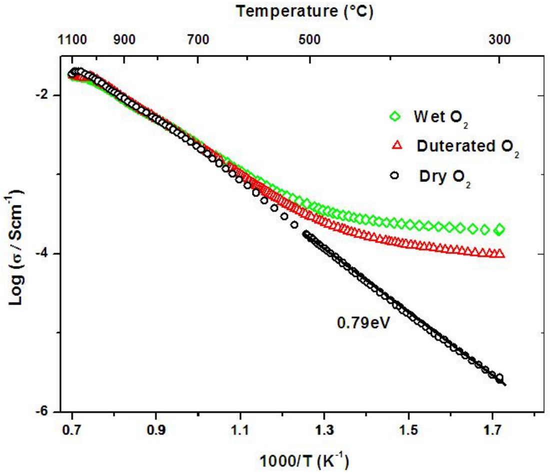

Figure 7 Total conductivity vs. 1/T of as-prepared $BaTi_{0.5}In_{0.5}O_{3-\delta}$ *measured at 10 kHz in wet* (H_2O, D_2O) *and dried* O_2 *with ramping at a rate of 18°/hour.*

3.1.3. ZnO as sintering aid in Yb-doped $BaZrO_3$

The purpose of this study was to investigate the effects of different preparative routes and addition of ZnO has on the densification of $BaZrO_3$-based ceramics and ultimately how this is reflected in the conductivity of the material. For the stoichiometric samples prepared by a sol-gel route, phase pure material was obtained according to XRD data. Figure 8 compares the complex plane plots for the pre-hydrated samples under different environment at 300°C. The Arrhenius plots for pre-hydrated samples are displayed in Figure 9. The data shows that the addition of stoichiometric amounts of Zn^{2+} via a sol-gel synthesis route promotes not only densification but also water incorporation and conductivity in comparison with the solid state sintering route, keeping the same final sintering temperature of 1500°C. For example, pre-hydrated $BaZr_{0.78}Zn_{0.02}Yb_{0.2}O_{3-\delta}$, prepared via the sol-gel method shows total conductivity (σ_{tot}) value of $3.14 \cdot 10^{-5}$ and $3.8 \cdot 10^{-3}$ Scm^{-1}, whereas for the solid state route, σ_{tot} values are $1.74 \cdot 10^{-5}$ and $8.87 \cdot 10^{-4}$ Scm^{-1} under dry Ar (heating cycle) at 300° C and 600° C, respectively.

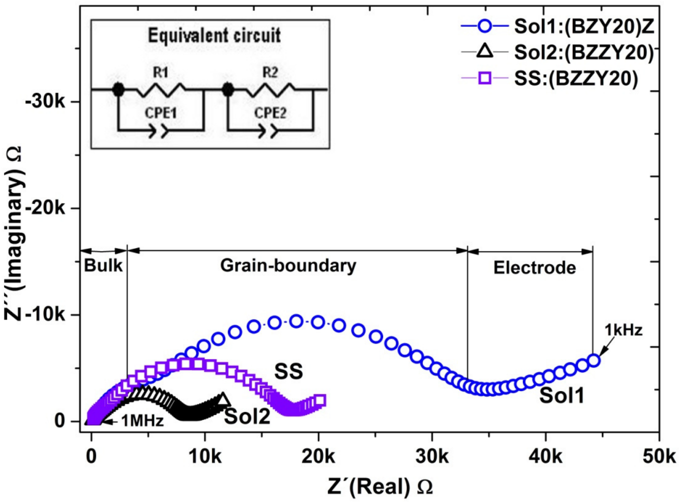

Figure 8. Complex plane plot of hydrated samples for heating cycle in dry Ar at 300°C. Inset: Equivalent circuit used to extract conductivity.

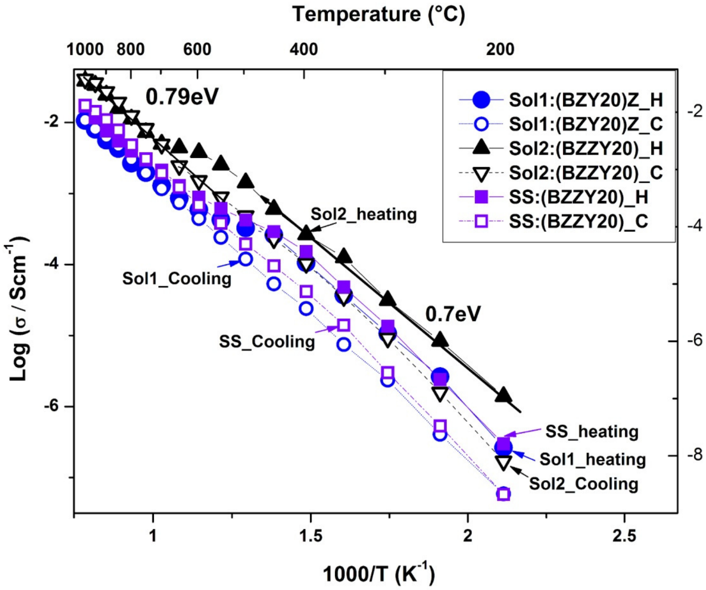

Figure 9. Total conductivity of pre-hydrated samples in dry Ar heating (H, filled symbols) & cooling (C, Open symbols) cycle.

3.1.4. Metallic oxides/Mixed conductors

Mixed conductors are of interest for use as anode and cathode materials in fuel cells and materials combining protonic and electronic conduction may find applications as membranes for H_2 gas separation. We have synthesized metallic perovkites ($SrMoO_3$; $SrVO_3$) and double perovskite structured materials like Ca_2VMoO_6 and Sr_2VMoO_6 by solid state sintering routes. Phase pure Ca_2VMoO_6, for example, show from DC resistivity (cf. Figure 10) measurements metallic behavior with σ at RT being $0.714 \cdot 10^3$ (Scm^{-1}). We will apply doping studies and sol-gel synthesis techniques under controlled atmosphere in order to optimize these materials with respect to purity and conducting properties. One of the challenges was to get the materials sufficiently dense to be able to avoid gaseous leakages in measurements of hydrogen flux. This has so far not been successful.

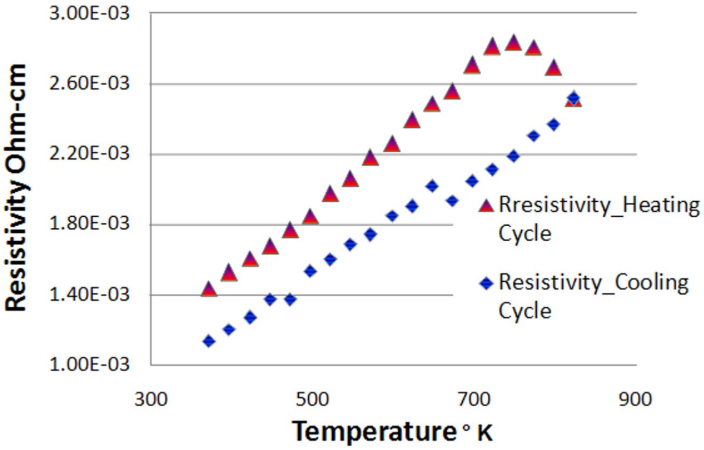

Figure 10. DC resistivity data on Ca_2VMoO_6 shown for heating and cooling cycle.

3.1.5. Oxygen deficient double perovskites: $Ba_2NdSnO_{5.5}$

Double perovskite structured $Ba_2NdSnO_{5.5}$ has been prepared by traditional solid state sintering and sol-gel polymerization. The compound was made phase pure under oxidizing conditions but it is still a challenge to avoid formation of impurity phases. Hydration studies of the compound show a two-step water uptake and the material is a mixed ion electron conductor. To address this behavior, we performed in-situ neutron diffraction studies to better understand the hydration process. Rietveld analysis of x-ray powder diffraction data has been performed. Additional information concerning oxygen vacancy formation and local structure will be obtained by analysis of total scattering neutron data (already collected at Polaris, ISIS).

3.1.6. Solid solution of barium cerate and barium zirconate

Solid solutions of barium cerate and barium zirconate doped with a rare earth cation on the B-site, $BaCe_{(0.9-x-y)}Zr_xRE_yO_{(3-\delta)}$, require sintering temperatures of 1700-1800°C to reach relative densities higher than 95% [7, 8]. Addition of small quantities of a sintering aid (called M) on the B site reduces the sintering temperature by 250 to 300°C e.g. refs. [9, 10, 11]. In a previous work [11], we obtained 95% dense samples at 1450°C with addition of Ni or Co on the B site of $BaCe_{0.2}Zr_{0.7}Y_{0.1}O_{(3-\delta)}$, substituting for Y at level of 1 or 2 mol%. The conductivity of these samples was in the same range as for the Ni- or Co- free compounds sintered at 1700°C [11]. We did also fabricate the materials by solid state reaction sintering and the conductivity behaviour of these materials was really promising.

3.1.7. Conductivity, transport number measurements and hydration thermodynamics of $BaCe_{0.2}Zr_{0.7}Y_{(0.1-\xi)}Ni_{\xi}O_{(3-\delta)}$

These results encouraged us to continue the study of the $BaCe_{0.2}Zr_{0.7}Y_{(0.1-\xi)}Ni_{\xi}O_{(3-\delta)}$, focusing on nickel since this element is commonly used in the anode cermet for PCFC. BCZY27-1Ni and BCZY27-2Ni (for ξ=0.01 and 0.02, respectively) were prepared by solid state reaction compounds (The compounds are denoted as BCZY27-ZNi, where Z corresponds to the molar % of Ni).

The stability towards CO_2 for the materials has been studied by treating samples at 600°C in a wet CO_2 containing atmosphere for 3 weeks. The weights of the powders have been measured regularly and no increase has been observed showing no signs of the formation of barium carbonate; XRD, furthermore, supported this (Figure 11). Consequently, it was concluded that these Ni or Co substituted BZY10 and BCZY27 are stable towards CO_2.

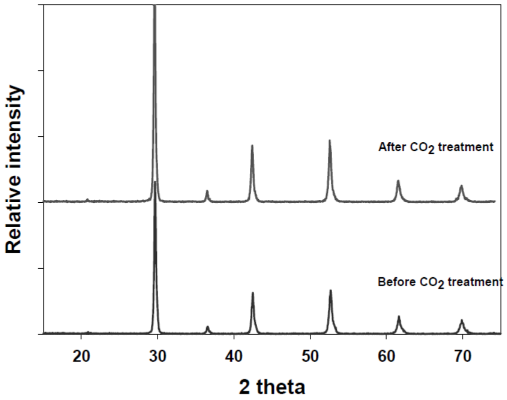

Figure 11: X-ray patterns of the 1% Ni doped BCZY27 before and after being treated in a CO_2 rich atmosphere at 600°C for 3 weeks.

Effects on the total conductivity of water vapor and oxygen partial pressure dependencies were studied as a function of temperature, and the transport numbers of the charge carriers (protons, oxide ions, holes) are determined by the emf technique. Additionally, TEM has been applied to characterize the grain boundaries. Thermodynamic parameters are calculated from conductivity measurements and simultaneous thermogravimetry and differential scanning calorimetry (TG-DSC).

Doped solid solutions of barium zirconate and barium cerate (BCZY27) have been synthesized at 1400°C and sintered at 1450°C rather than 1700°C as normally required, using Ni as sintering aid at level of 1 and 2 % of the B site of the perovskite. Segregation of nickel was observed in the grain boundaries of BCZY27-2Ni, showing that the solubility limit of Ni is between 1 and 2%. TEM has been applied to characterize the grain boundaries. Segregation of nickel was observed in the grain boundaries of BCZY27-2Ni, showing that the solubility limit of Ni is between 1 and 2%. This is illustrated in Figure 12 showing that the signal of Ni increases at the grain boundary.

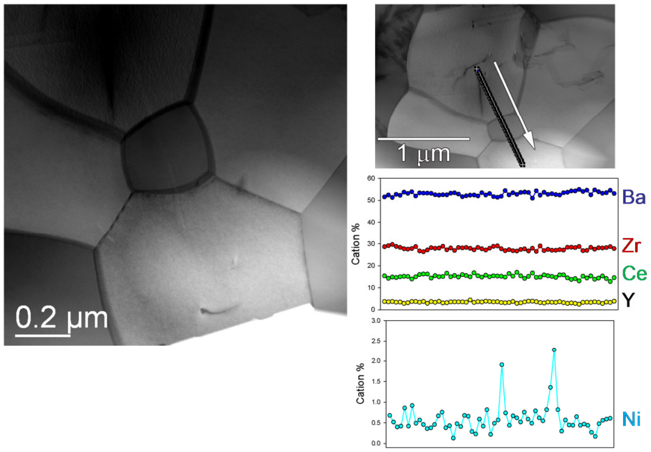

Figure 12 BCZY27-2Ni: Bright field TEM image EDS line scan across two grain boundaries.

Electrical characterization was performed as a function of water vapour and oxygen partial pressures at various temperatures and transport numbers were measured by means of the EMF technique. The two compounds present similar conductivity behaviour: protons are the predominating charge carriers under humid atmospheres below ~650°C. Above this temperature oxide ions starts to dominate the ionic conductivity. Under oxidizing conditions, electron holes contribute, whereas no electronic conductivity was evident under reducing conditions. This is illustrated in Figure 13 showing the pO_2 dependence at different temperature. The transport numbers as a function of temperature under oxidizing and reducing conditions are presented in Figure 14 and confirm this picture. Furthermore, the hydration enthalpy has been determined by two different methods (conductivity and TG-DSC), and was found coherent and about $-125\ \mathrm{kJ \cdot mol^{-1}}$

With bases in the conductivity data and transport numbers as a function of temperature and atmosphere, it is possible to discuss briefly which applications are suitable for the BCZY27-Ni compounds, and what the constraints are. As we have seen, BCZY27-Ni is a pure proton conductor only for temperatures lower than 600°C and for oxygen partial pressure lower than 10^{-5} atm.
For a hydrogen sensor the electrolyte has to present pure proton conduction, even if it is low. BCZY27-Ni could be used for such an application at temperatures below 600°C. A membrane for hydrogen separation must conduct both protons and electrons. An option would be to add the electronic conductor as a second phase i.e. BCZY27-Ni/metal cermet. For a fuel cell, the anode side is exposed to hydrogen, while oxygen/air is present at the cathode side. The OCV of typical experimental fuel cell based on BCZY27-Ni has been calculated at 600°C using the Schmalzried equation [12]:

$$E = \frac{R \cdot T}{F}\left[\ln\left(\frac{p^{*}{}_{p}{}^{1/4} + p_{H_2O}{}^{1/2} \cdot K^{-1/2} \cdot p_{H_2}{}^{-1/2}}{p^{*}{}_{p}{}^{1/4} + p_{O_2}{}^{1/4}}\right) + \ln\left(\frac{p^{*}{}_{n}{}^{1/4} + p_{O_2}{}^{1/4}}{p^{*}{}_{n}{}^{1/4} + p_{H_2O}{}^{1/2} \cdot K^{-1/2} \cdot p_{H_2}{}^{-1/2}}\right)\right]$$

With p^*_n and p^*_p the oxygen partial pressures describing the low and high limit of the ionic domain i.e. when the n-type and p-type respectively are equal to the ionic conductivity and K the equilibrium constant of the reaction of formation of water from hydrogen and oxygen. R, T, F have their usual meaning. Calculations were performed assuming $p(H_2O)=0.01$ atm, $p(O_2)=0.21$ atm and $p(H_2)=1$ atm, i.e. for an H_2/air cell. As n-type conductivity is absent in reducing atmosphere, the p^*_n term was omitted as the calculations showed that the OCV was independent p^*_n when $p^*_n<10^{-30}$ atm. The OCV values for BCZY27-1Ni and BCZY27-2Ni (Table 1) are in the same order than other compounds based on barium cerate and barium zirconate. As shown by Bonanos *et al.* [13], the presence of electronic conductivity (in our case holes) produces only small loss of OCV (less than 50mV at 600°C).

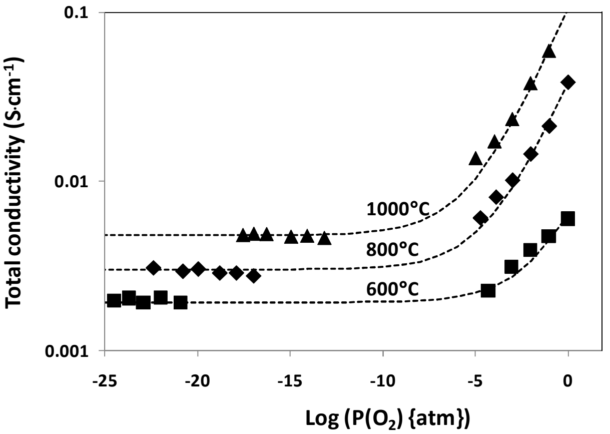

Figure 13. Oxygen partial pressure dependency of the total conductivity for BCZY27-1Ni specimen, in wet atmospheres ($p(H_2O)=0.03$ atm) at 600, 800 and 1000°C. The dotted lines correspond to the fit using equation

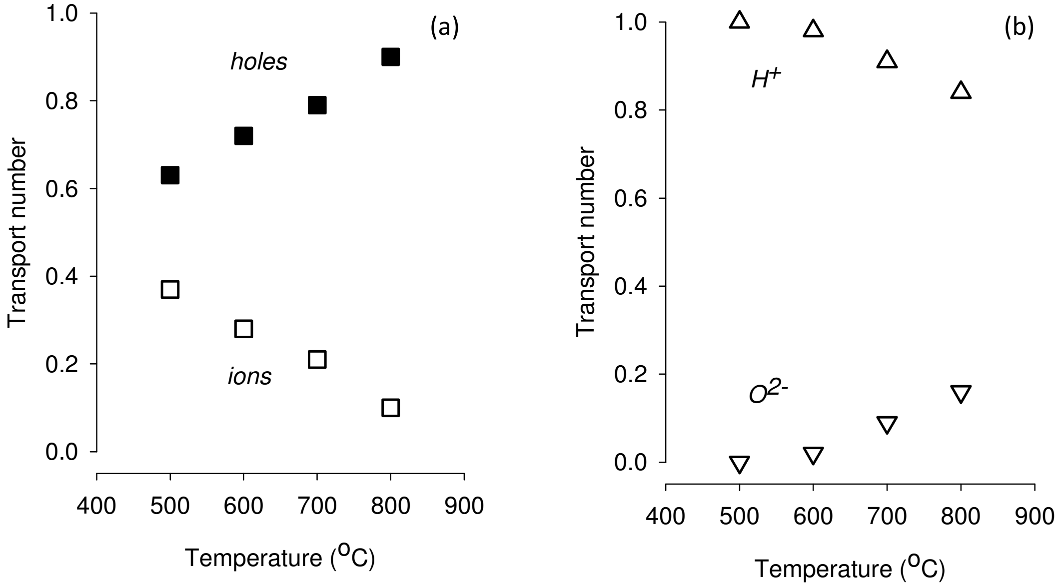

Figure 14 Effective transport numbers vs. temperature for BCZY27-Ni: the results are similar for the two compositions: a) in wet oxidizing atmosphere; b) in wet reducing atmosphere.

Table 1 *Calculation the OCV of a typical experimental fuel cell based on BCZY27-Ni electrolyte using the Schmalzried equation and comparison with values from literature.*

Temperature	600°C				
Compound	BCZY27-1Ni	BCZY27-2Ni	BCY10 [35]	$BaCe_{0.7}Nb_{0.1}Sm_{0.2}O_{3-d}$ [36]	BZY10/Zn [37]
OCV (V)	1.10	1.09	1.145	0.998	0.990

3.2. Properties of $LaNbO_4$ related materials – the approach of acceptor doping

Substitution with aliovalent cations is indeed a frequently used strategy to modify and control the electrical properties of ceramic materials. Therefore, when selecting the type of doping element and its concentration, the targeted defect formation and the structural features of the host crystal lattice have to be taken into account. Acceptors in $LaNbO_4$ are charge compensated by formation of oxygen vacancies [14]. The vacancy formation is accompanied by a local structural relaxation, associated with rearrangement of $[NbO_4]^{3-}$ tetrahedra forming $[Nb_2O_7]^{4-}$ units. Moreover, as shown by [14] for the tetragonal symmetry of $LaNbO_4$, the solution energies of foreign elements into the La- and Nb-sublattices depend on their ionic radii, pointing out that geometrical similarity is energetically favorable.

Looking at the literature of proton conductors there have been a few attempts to empirically correlate hydration thermodynamics and proton transport to physical parameters and structure[15, 16, 17, 18]. The hydration enthalpy was correlated to the ionic radius along the series of Ca doped rare-earth ortho-niobates [1, 19, 20], whereas for perovskite structured oxides other parameters like basicity and electronegativity have been tested[16, 21]. Within one class of materials, variations in the proton mobility generally depend on changes within the structure of which the ionic radius obviously plays an important role. In order to select the elements to (co-)acceptor dope on the A- and/or B-site in $LaNbO_4$, we have therefore chosen to evaluate the ionic radius and the electronegativity. Figure 15 shows the Pauling electronegativity as a function of the ionic radii (according to Shannon [22]) for the selected doping elements, as well as for the parent cations. The materials in the present study have a chemical composition corresponding to the general formula $La_{(1-x)}D_{A(x)}Nb_{(1-y)}D_{B(y)}O_{(4-\delta)}$, where D_A is either Ca or Ba and D_B is one of Ga, Ge, In or Ti (x=0 or 0.01; y=0.01) as summarized in Table 2. Different doping schemes of $LaNbO_4$, A- and/or B-site, were implemented aiming to correlate the conductivity of doped materials with the chemical and structural features of the host-guest matrix. Ultimately, this strategy may lead to an improved understanding from which the conductivity behavior of acceptor doped $LaNbO_4$ materials may be optimized.

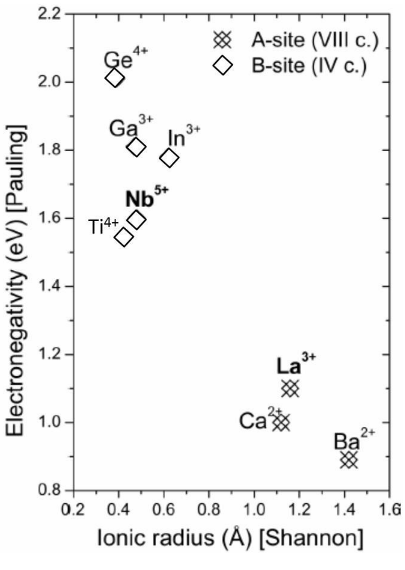

Figure 15. Ionic radii and electronegativities of the elements (co-)doped on A- and/or B-site in $LaNbO_4$.

Table 2. Summary of the systems considered in the present study with the corresponding names of the compounds as used in the text.

Type of doping	**System name (as ref. in text)**	**Nominal composition**	**Name of the compound**
B-site doping	LN-D_B	$LaNb_{0.99}Ga_{0.01}O_{4-\delta}$	LN-Ga
		$LaNb_{0.99}Ge_{0.01}O_{4-\delta}$	LN-Ge
		$LaNb_{0.99}In_{0.01}O_{4-\delta}$	LN-In
		$LaNb_{0.99}Ti_{0.01}O_{4-\delta}$	LN-Ti
A- and B-site co-doping	LCN-D_B	$La_{0.99}Ca_{0.01}Nb_{0.99}Ga_{0.01}O_{4-\delta}$	LCN-Ga
(Ca on A-site)		$La_{0.99}Ca_{0.01}Nb_{0.99}Ge_{0.01}O_{4-\delta}$	LCN-Ge
		$La_{0.99}Ca_{0.01}Nb_{0.99}In_{0.01}O_{4-\delta}$	LCN-In
		$La_{0.99}Ca_{0.01}Nb_{0.99}Ti_{0.01}O_{4-\delta}$	LCN-Ti
A- and B-site co-doping	LBN-D_B	$La_{0.99}Ba_{0.01}Nb_{0.99}Ga_{0.01}O_{4-\delta}$	LBN-Ga
(Ba on A-site)		$La_{0.99}Ba_{0.01}Nb_{0.99}Ge_{0.01}O_{4-\delta}$	LBN-Ge
		$La_{0.99}Ba_{0.01}Nb_{0.99}In_{0.01}O_{4-\delta}$	LBN-In

Much of the focus at three of the partners has been to optimize, characterize and understand the behavior of materials based on $LaNbO_4$. Naturally there are large amounts of data that would have deserved to be part of this report. However, that is not possible and only a fraction of it will be included here. More details from the data are available within the different contributions shown in the publication list.

3.2.1. Solubility limit of Sr and Ca as dopants of the La site in $LaNbO_4$

As state above, the solubility limit of different doping elements is a crucial parameter to optimize the electrical conductivity of acceptor doped systems. In the present project a task was initiated to determine the solubility limit of Ca and Sr and even with both present on the A-site in $LaNbO_4$. The common approach to establish these limits is to vary the concentration of the doping and determine the unit cell parameters as a function of its concentration. According to the behavior of Vegard’s law, unit cell parameters ideally vary linearly with the doping concentration within the solubility range and eventually become independent of the doping level once the solubility limit is exceeded. For the Ca- and Sr-doped $LaNbO_4$ system, these measurements proved difficult and no definite conclusion was made as to the solubility limit, since no simple relation was observed between any of the unit cell parameters and the doping level. This is exemplified in Figure 16 showing the variation in unit cell volume with the level of Sr and Ca doping.

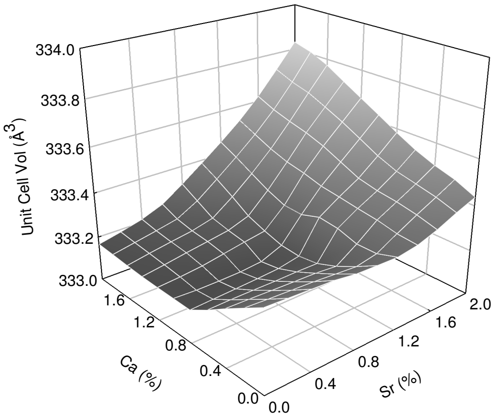

*Figure 16. Unit cell volume as a function of the nominal level of Ca and Sr. As evident, Vegard's law behaviour is not satisfied and no conclusion can be made with respect to the solubility limit***.**

3.2.2. Conductivity of B-site and A- and B-site codoped $LaNbO_4$

As seen from Table 2, several different B-site elements have been tested as potential doping elements for $LaNbO_4$, in addition to the more "conventional" A-site Ca, Sr and Ba, Ti, Ga, In and Ge substituted $LaNbO_4$ were all synthesized and the electrical conductivity was characterized. In particular the effect of Ti and Ti codoped with Ca was thoroughly studied. Since a similar behavior was encountered for the other B-site substituents, the most important findings will be reported here, but since the treatment of the data includes derivation and use of defect chemical models, the paper in Ti doped $LaNbO_4$ is included as part of the appendix (cf. A4). Figure 17 summarizes the conductivity of Ga, Ge and In doped and A-site co-doped with either Ca or Ba.

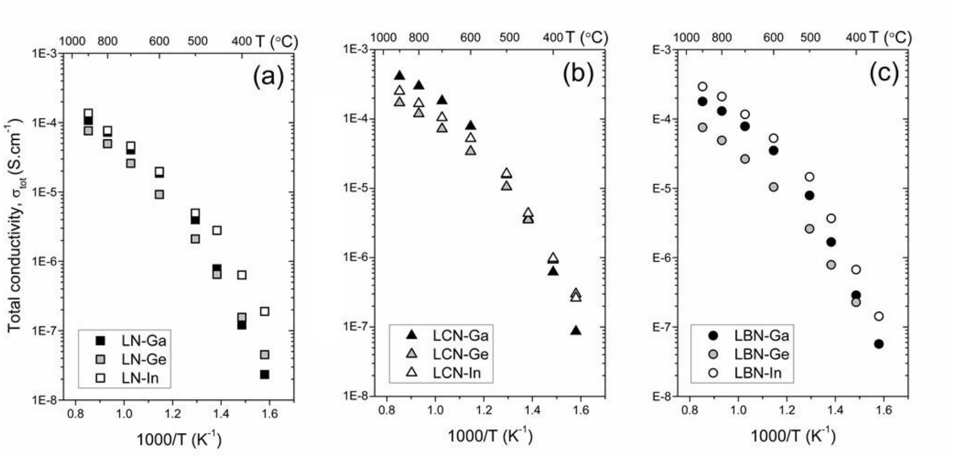

Figure 17. Total conductivities of some of the (a) B-site doped (b) co- Ca A-site and B-site doped, and (c) co- Ba A-site and B-site doped $LaNbO_4$ developed in the present study as a function of the inverse temperature. The data is measured under wet hydrogen.

The highest conductivity encountered within this study was for the material co-doped with Ca and Ga, but since Ca substitution on the A-site alone gave even higher conductivities, we cannot ascertain that this reflects any beneficiary effect of co-doping. The activation enthalpy of proton mobility was in the range of 70-85 kJ/mol. This is higher than for the A-site doped materials and the reasons for this will be further discussed in relation to the behavior of the Ti substituted materials below.

Figure 18 a) shows the shows total conductivity (10 kHz) vs. 1/T for $LaNb_{0.99}Ti_{0.01}O_4$ from 1100 °C to 350 °C in various atmospheres, and b) the bulk conductivity from impedance spectroscopy vs. p_{O_2} at 1000, 900 and 800 °C. Figure 18 c) shows bulk conductivity vs. p_{H_2O} in reducing atmosphere at temperatures from 1200 to 700 °C.

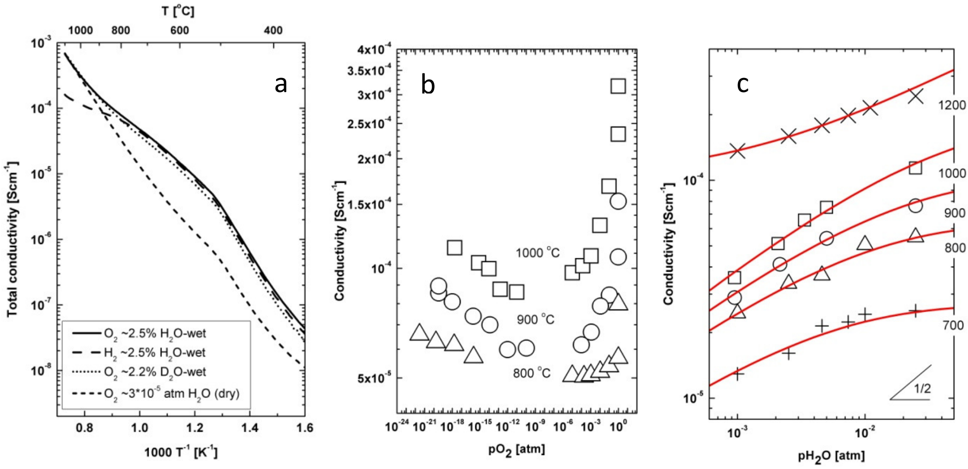

Figure 18 Sample: $LaNb_{0.99}Ti_{0.01}O_4$. a) Conductivity at 10 kHz as a function of 1000/T in H_2O-wet, D_2O-wet and dry O_2 and in H_2O-wet H_2. b) Bulk conductivity as a function of partial pressure of oxygen at 1000, 900 and 800 °C in wet atmospheres. c) Bulk conductivity as a function of partial pressure of water vapour in the temperature range from 1200 °C to 700 °C in reducing atmosphere. Solid lines represent modelled conductivites as a function of p_{H_2O} *based on thermodynamic parameters.*

Similarly Figure 19 a) shows for material codoped with Ca and Ti ($La_{0.99}Ca_{0.01}Nb_{0.99}Ti_{0.01}O_4$) total conductivity (at 10 kHz) vs. 1/T from 1100 °C to 300 °C in wet hydrogen and bulk conductivity from impedance spectroscopy in wet and dry oxygen. Figure 19 b) shows bulk conductivity vs. p_{O_2} at 1000, 900 and 800 °C. Figure 19 c) shows bulk conductivity vs. p_{H_2O} in reducing atmospheres in the temperature range from 1200 to 700 °C. It is worth highlighting from Figure 19 a) that the conductivity of $La_{0.99}Ca_{0.01}Nb_{0.99}Ti_{0.01}O_4$ is very different in hydrogen and oxygen atmospheres. The behaviour under oxidising conditions is similar to that of $LaNb_{0.99}Ti_{0.01}O_4$. However, under reducing conditions the conductivity is considerably higher, less temperature dependent, and with no indications of the 2nd order phase transition. The dual phase nature of $La_{0.99}Ca_{0.01}Nb_{0.99}Ti_{0.01}O_4$, observed by SEM and XRD, is also reflected in the electrical measurements and indicates that both phases are percolating the sample. Here, the small conductivity dependence on temperature under reducing atmospheres resembles that of $LaNb_3O_9$ [22], where n-type conductivity predominates, and the mixed p-type and proton conductivity in oxidising atmosphere resembles that of $LaNbO_4$.

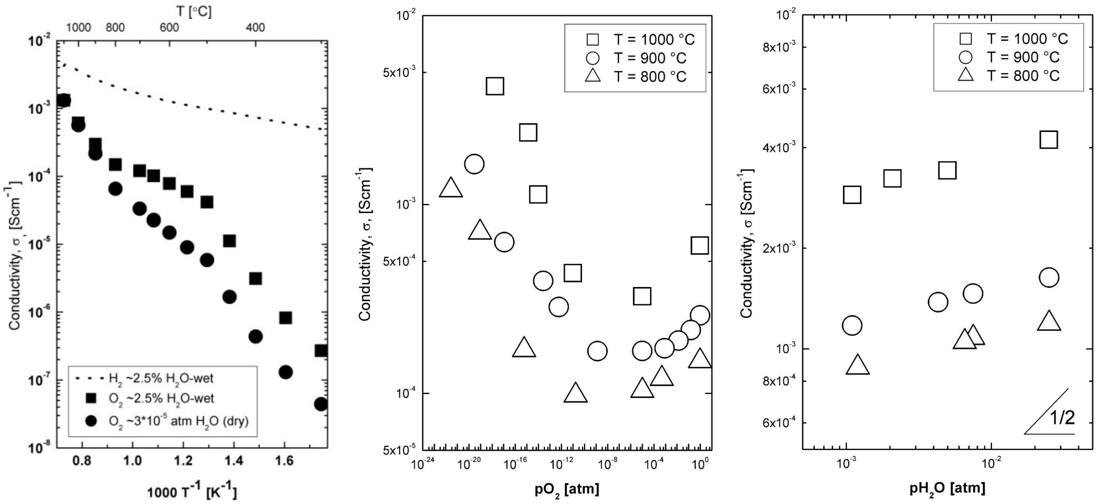

Figure 19 Sample: $La_{0.99}Ca_{0.01}Nb_{0.99}Ti_{0.01}O_4$. a) Conductivity at 10 kHz in H_2O-wet H_2, bulk conductivity deduced from impedance spectroscopy in H_2O-wet O_2 and in dry O_2, all as a function of inverse temperature. b) Conductivity as a function of partial pressure of oxygen in wet atmospheres. c) Conductivity as a function of partial pressure of water vapour in reducing atmosphere.

3.2.3. Defects and defect associates in acceptor doped $LaNbO_4$

The careful analysis of the conductivity data for these A and B-site acceptor doped $LaNbO_4$ materials and the comparison to the literature data for the 1%Ca doped version, show that the apparent proton transport seems more activated and also that the effect of water vapor on the conductivity is more exothermic for the B-site doped materials. Mather et al [14] have studied by computational approaches association between acceptor substituents, oxygen vacancies and protons. They find that the attraction certainly varies with the different substituents and also that there is a difference between A and B site. It seems clear that the formation of defect associated proton-B-site acceptors (Ti) is stronger than for the A-site (Ca). This corresponds well with our experimental observations and the mathematical relations derived to model. We did furthermore look into the difference between the number of positions of the protons in the monoclinic and the tetragonal polymorph of $LaNbO_4$ and how this affected the hydration thermodynamics.

In order to derive the formalism necessary to derive physicochemical parameters representing the hydration thermodynamics, the association thermodynamics, the enthalpy of mobility of the different species a rather extensive derivation was accomplished. This includes a model for the point defect chemistry implementing the formation of the larger structural entities representing the oxygen vacancy charge compensating the acceptor and the defect associate between the acceptor and the protons. The modeling was performed both with and without the associated species and the parameter set fitted to represent the conductivity behaviour (variations in conductivity with temperature and p_{H_2O}) of $LaNb_{0.99}Ti_{0.01}O_4$ is presented in Table 3. These data correspond to the high temperature tetragonal structure only, due to the limited temperature window (between 500 and 350 °C) for the monoclinic phase.

Table 3 Thermodynamic parameters for hydration and mobility of protons in Ti- and Ca-doped $LaNbO_4$.

$LaNb_{0.99}Ti_{0.01}O_4$	ΔS^0_{hydr} **[J/mol K]**	ΔH^0_{hydr} **[kJ/mol]**	ΔH^0_{assoc} **[kJ/mol]**	μ_{0,H^+} **[cm²K/Vs]**	$\Delta H_{mob,H^+}$ **[kJ/mol]**	$\mu_{0,v_O^{\bullet\bullet}}$ **[cm²K/Vs]**	$\Delta H_{mob,v_O^{\bullet\bullet}}$ **[kJ/mol]**
Non-assoc. defect model *	-143± 15	-152±14	N/A	90 ± 5	86 ± 4	1.2 ± 0.5	61 ± 10
Assoc. defects model **	- 173± 8	-145± 5	-65 ± 2	8 ± 2	55 ± 3	2 ± 0.5	60 ± 5
$La_{0.99}Ca_{0.01}NbO_4$ [2]	-130 ± 10	-115±10	N/A	35 ± 10	55 ± 5	15 ± 5	60 ± 5

** model consisting of non-degenerate non-associated H^+, O^{2-} and electronic charge carriers.*
*** model consisting of associated and "free" H^+, O^{2-} and electronic charge carriers.*

Figure 20 shows the measured total conductivities of $LaNb_{0.99}Ti_{0.01}O_4$ and the partial conductivities generated from the parameters for the associated defects model presented in Table 3, as a function of inverse absolute temperature under a) wet oxidising conditions and b) wet reducing conditions for $LaNbO_4$.

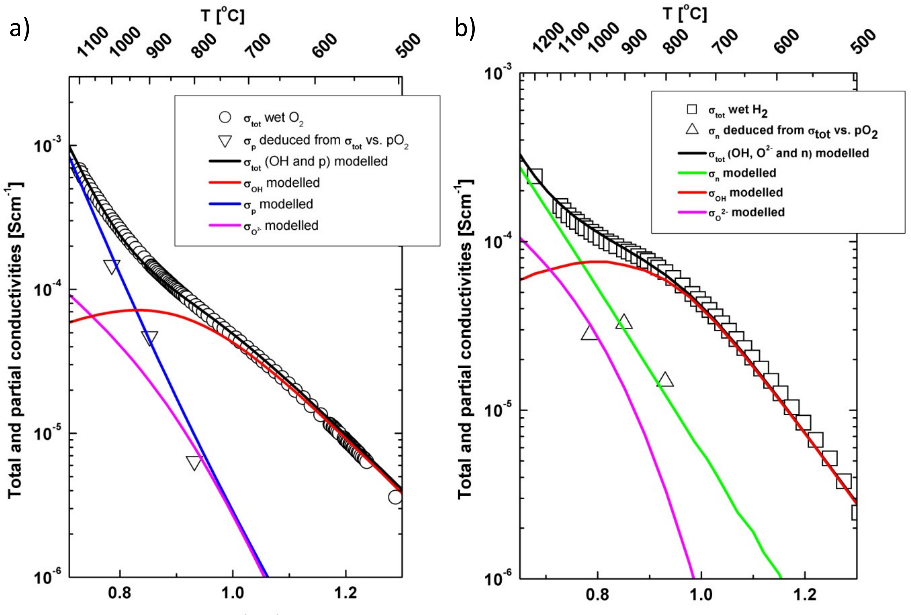

Figure 20 Sample: $LaNb_{0.99}Ti_{0.01}O_4$. Conductivities as a function of inverse absolute temperature. a) In wet O_2: Measured 10 kHz (○) and partial electronic (∇) conductivities. b) In wet H_2: Measured 10 kHz (□) and partial electronic (Δ) conductivities. Modelled total, partial electron, partial proton and partial oxide ion conductivities are represented as lines and generated from thermodynamic and mobility parameters from Table 3.

In order to investigate effects of acceptor doping on the A and/or B site of $LaNbO_4$, Figure 21 compares p_{O_2} -dependences of the conductivity at 800 and 1000 °C for the present $LaNb_{0.99}Ti_{0.01}O_4$ and $La_{0.99}Ca_{0.01}Nb_{0.99}Ti_{0.01}O_4$ with $La_{0.99}Ca_{0.01}NbO_4$ [2] and undoped $LaNbO_4$ [23]. It is evident that the undoped $LaNbO_4$ in all cases exhibits significantly lower conductivity than the acceptor doped versions. $La_{0.99}Ca_{0.01}NbO_4$ has the highest ionic conductivity while under the most reducing conditions the $La_{0.99}Ca_{0.01}Nb_{0.99}Ti_{0.01}O_4$ exhibits a considerable n-type contribution due to a secondary phase of $LaNb_3O_9$. The Ti-doped material, $LaNb_{0.99}Ti_{0.01}O_4$, shows the lowest overall conductivity of the acceptor doped compositions.

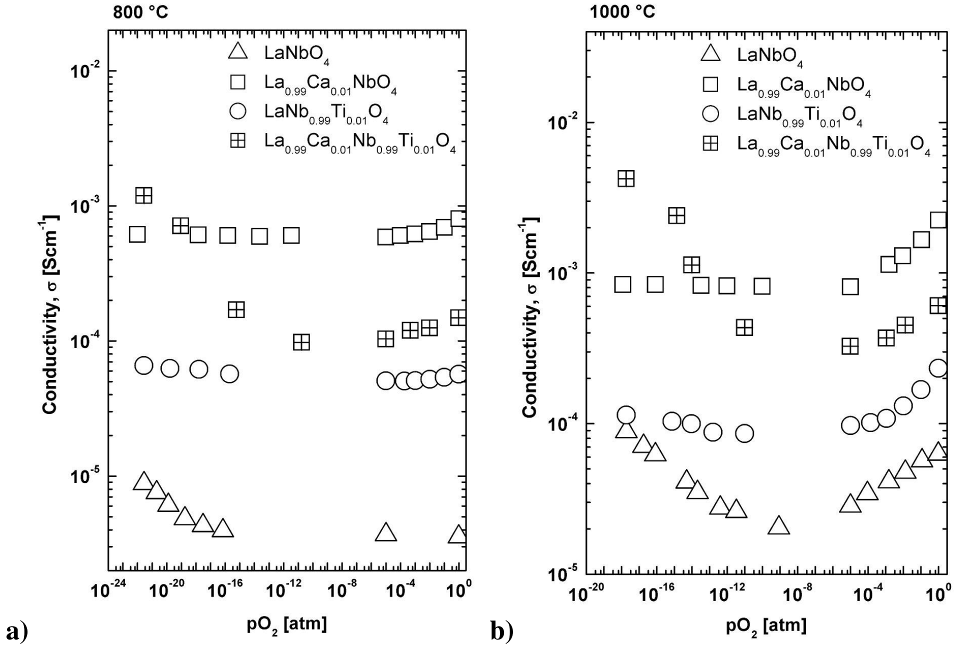

Figure 21 Conductivity as a function of p_{O_2} *in wet atmospheres for* $La_{0.99}Ca_{0.01}NbO_4$, $LaNb_{0.99}Ti_{0.01}O_4$, $La_{0.99}Ca_{0.01}Nb_{0.99}Ti_{0.01}O_4$ *and undoped* $LaNbO_4$ *at a) 800 °C and b) 1000 °C.*

Both $La_{0.99}Ca_{0.01}NbO_4$ and $LaNb_{0.99}Ti_{0.01}O_4$ show contributions from hole (p-type) conductivity in oxidising atmospheres at 1000 and 800 °C. For the undoped sample there is a significant contribution of n-type electronic conductivity coming up at low p_{O_2} whereas the Ti- and Ca-doped samples show little and no n-type conductivity. This reflects as expected that the negative acceptor increases the concentration of positive defects and depresses the concentration of electrons. Going in detail on the features of the p_{O_2} -dependence, indications of n-type conductivity at 1000 °C are present in the case of Ti-doping. One may therefore suggest that the multivalent nature of Ti reduces slightly the effective band gap and consequently increases the concentration of electrons. This behaviour is in agreement with the interpretation of the p_{H_2O} dependence at 1200 °C.

From a defect chemical viewpoint (cf. Eq. A1 and analogously for Ca-doping), it is not obvious that equal acceptor doping concentrations of Ti and Ca in $LaNbO_4$ (e.g. $LaNb_{0.99}Ti_{0.01}O_4$ and $La_{0.99}Ca_{0.01}NbO_4$) should result in a difference in conductivity of approximately one order of magnitude (cf. Figure 21). In principle, a lower solubility for Ti^{4+} than Ca^{2+} in $LaNbO_4$ would explain a difference in proton conductivity, however no segregated secondary Ti-rich phase was detected during microstructural characterization, nor is it likely in this case that a difference in effective acceptor doping level alone can account for the effect on the conductivity.

3.2.4. $LaVO_4$ results and discussion

$LaVO_4$ may similarly as $LaNbO_4$ crystalize in a monoclinic and a tetragonal polymorph. In addition, $LaPO_4$, $LaAsO_4$ all take the monoclinic monazite-type structure. The m-$LaNbO_4$ is slightly different as it forms in the fergusonite-type structure (at T > 500 °C). Consequently, there are differences in the structure of these materials that make it interesting to compare their conductivity behavior and to search for correlations that may increase the general understanding of proton conductivity. On these bases and due to the fact that the conductivity properties of $LaVO_4$ had not been characterized, $LaVO_4$ was chosen for a more academic, fundamental study. Thermodynamic and transport parameters were modeled from the conductivity in order to compare the behavior of $LaVO_4$ with other oxides in the *m*-$LaXO_4$-series.

Samples of nominally undoped $LaVO_4$, $La_{0.99}Ca_{0.01}VO_4$ and $La_{0.95}Ca_{0.05}VO_4$ were synthesized by the solid state route. From the structural microstructural characterization it was shown that the acceptor solubility was, similarly as for the niobates, low and in the order of 1-3 %. The unit cell volume was observed to decrease slightly with the addition of Ca also similar as for the niobates.

The conductvity increases considearbly from nominally undoped $LaVO_4$ to $La_{0.99}Ca_{0.01}VO_4$, whereas the effect of increasing the doping level to 5% ($La_{0.95}Ca_{0.05}VO_4$) was lower than expected. This is in-line with the observations from structural and compositional characterization (XRD and SEM), that the solubility limit of Ca is low. Investigation of the effects of temperature, oxygen and water vapor partial pressures, as well as, on shifts between H_2O and D_2O containing gases revealed that the conductivity of acceptor doped $LaVO_4$ is predominated by ionic charge carriers and that protons are important at low temperatures and under wet conditions. Figure 22 displays the total conductivity in wet oxygen and the partial oxide ion and proton conductivities (left axis), all as a function of inverse absolute temperature. The protonic transport number (right axis) is also plotted as a function of inverse absolute temperature.

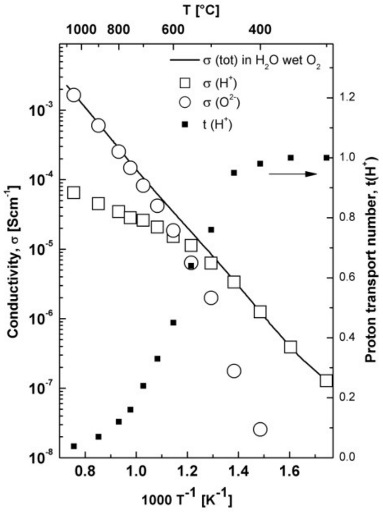

Figure 22 Left axis: Conductivity vs. inverse temperature. AC conductivity in H_2O-wet O_2 (solid line), partial oxide ion (open circles) and proton conductivity (open squares). Right axis: Protonic transport number vs. inverse temperature (closed squares).

Thermodynamics of hydration and transport parameters for the charge carriers in $La_{0.99}Ca_{0.01}VO_4$ (Table 4) were determined by fitting models for the defect chemistry and transport properties to the total and partial conductivity data (cf. Figure 22) as outlined in e.g. [1]. The enthalpy of proton mobility, $\Delta H_{\mathrm{mob,H^+}}$, for $La_{0.99}Ca_{0.01}VO_4$ was found to be 75 ± 10 kJ/mol with a pre-exponential of 50 ± 5 cm^2 K/Vs. The standard enthalpy of hydration, $\Delta H^0_{\mathrm{hydr}}$, was found to be -110 ± 10 kJ/mol and standard entropy of hydration, $\Delta S^0_{\mathrm{hydr}}$ without correction for proton site degeneracy and oxide ion vacancy clustering, was found to be -130 ± 10 J/mol K. Based on the structural similarities between the monazite-type materials in the series, one may assume the same number of stable proton sites for $LaVO_4$, $LaAsO_4$ and $LaPO_4$ [10, 13, 14]. In the study of Ti-doped $LaNbO_4$, we introduced a correction term for proton site degeneracy, $N_{\mathrm{H^+}}$, and oxygen vacancy clustering, $N_{v_O^{\bullet\bullet}}$, for the hydration equilibrium constant:

$$K_{\mathrm{hydr}} = \frac{\left[(HVO_4)^{\bullet}_{VO_4}\right]^2}{p_{H_2O}\left[(V_2O_7)^{\bullet\bullet}_{2VO_4}\right]\left[(VO_4)^{x}_{VO_4}\right]} = \exp\left(\frac{\Delta S^0_{\mathrm{hydr}} + R\ln\left(\frac{(N_{\mathrm{H^+}})^2}{N_{v_O^{\bullet\bullet}}}\right)}{R}\right)\exp\left(-\frac{\Delta H^0_{\mathrm{hydr}}}{RT}\right)$$

The corrected standard entropy of hydration, $\Delta S^0_{\mathrm{hydr,corr}}$, for $La_{0.99}Ca_{0.01}VO_4$ was found to be -142 ± 10 J/mol K.

3.3. Hydration thermodynamics and transport parameters in the $LaXO_4$-series.

Based on the several investigations done within the consortium and from literature data we will in the following discuss the hydration thermodynamics and transport parameters in A-site acceptor substituted $LaXO_4$ series of materials with structural similarities to $LaNbO_4$. Table 4 summarizes physicochemical parameters for protons and oxygen vacancies based on experimental and computational approaches.

*Table 4 Thermodynamic and transport parameters from modelling of conductivity data of $La_{0.99}Ca_{0.01}VO_4$, and corresponding literature values for acceptor doped $LaNbO_4$ [2], $LaTaO_4$ [31], $LaAsO_4$ [30] and $LaPO_4$ [27, 32]***.**

	$\Delta S^0_{\mathrm{hydr}}$ **[J/mol K]**	$\Delta H^0_{\mathrm{hydr}}$ **[kJ/mol]**	T_{dehydr} **(K_{hydr} = 1)**	$\mu_{0,\mathrm{H^+}}$ **[cm^2K/Vs]**	$\Delta H_{\mathrm{mob,H^+}}$ **[kJ/mol]**	$\mu_{0,v_O^{\bullet\bullet}}$ **[cm^2K/Vs]**	$\Delta H_{\mathrm{mob},v_O^{\bullet\bullet}}$ **[kJ/mol]**
$LaVO_4$	-130 ± 10 -142 ± 10 ^{I}	-110 ± 10	573 °C	50 ± 5	75 ± 10	120 ± 20	85 ± 10
$LaAsO_4$ [30]	-111 ± 9	-102 ± 5	646 °C	72 ± 12	86 ± 3	-	-
$LaPO_4$	-90 ^{a}	-83 ^{a}, -200 ^{b}	649 °C ^{a*}	-	84 ^{a}, 77 ^{b}, 94 ^{c}	-	-
$LaNbO_4$ * [28]	-	-		-	35-57 ^{II}, 60 ^{III}	-	-
$LaNbO_4$ ** [2]	-130 ± 10	-115 ± 10	612 °C	35 ± 10	55 ± 5	15 ± 5	60 ± 5
$LaTaO_4$ *** [31]	-120 ± 10	-100 ± 10	560 °C	10 ± 5	50 ± 5	15 ± 5	70 ± 5

* *LT monoclinic polymorph,* ** *HT tetragonal polymorph,* *** *HT tetragonal polymorph and octahedral oxygen coordination,*
^{I} *corrected for proton site degeneracy and oxygen vacancy clustering,* ^{II} *experimental,* ^{III} *computational*

The standard entropy of hydration is typically reported in the range from -100 to -160 J/mol K and has been assigned to the loss of one mol of water vapor [24, 25, 26]. It is widely accepted that protonic defects reside on oxygen sites as hydroxide ions. From a configurational viewpoint the different number of possible proton sites in the monazite- and the fergusonite-structured materials (4 and 2 O sites, respectively) and the different oxygen vacancy clustering in the two polymorphs could affect the hydration thermodynamics. Based on the correction term in the expression for K_{hydr}, this would result in ~15 J/mol K higher entropy of hydration for *m*-$LaNbO_4$, compared to $LaPO_4$, $LaAsO_4$ and $LaVO_4$. This change in standard entropy of hydration is small in comparison with the reported uncertainties of the hydration thermodynamic parameters and as expected no distinct difference in reported entropies of hydration was found between the monazite- and the fergusonite- structured materials. The standard entropy of hydration, without correction, for $LaNbO_4$, $LaVO_4$ and $LaAsO_4$ are all reported in the range from -130 to -111 J/mol K (cf. Table 4). The standard entropy hydration for $LaPO_4$ is reported lower than for the other $LaXO_4$-materials (-90 J/mol K [27, 32]) but combined with a relatively low hydration enthalpy (-83 kJ/mol [27]), the equilibrium constant of hydration for $LaPO_4$ is comparable with the others in the series. It may, consequently, be more useful to compare the dehydration temperature, T_{dehydr}, along the acceptor doped $LaXO_4$-series, which shows only small variations (from 560 to 650 °C). Taking into account the uncertainty ranges of these thermodynamic parameters, one may argue that the hydration does not seem to be significantly affected by different B site cations in the $LaXO_4$-series. These findings support the idea that a XO_4-unit is saturated with the incorporation of one proton per unit and, consequently, that the formation energy of a $(H_2NbO_4)^-$-unit is substantially greater than for a $(HNbO_4)^{2-}$-unit and therefore unlikely to be formed in a dilute acceptor doped $LaXO_4$. It is worth noting that due to the low solubility of acceptors in the series (about 1 mol%), determination of water uptake by thermogravimetric techniques has not been successful, and consequently hydration thermodynamics have been only determined indirectly from conductivity measurements.

The proton mobility parameters for fergusonite-type structured *m*-$LaNbO_4$ change with temperature (enthalpy of proton mobility changing from approximately 35 (at ~ 520 °C) to 57 (at ~ 205 °C) kJ/mol [28]), whereas it is constant with temperature for the monazite-type materials. On this basis, a direct comparison of the transport parameters between the monazite- and fergusonite-type materials is challenging. However, a correlation between the volume of the tetrahedra, V_{XO_4}, and the enthalpy of proton mobility has been found along the $LaXO_4$-series (cf. Figure 23). This suggests that the energy barrier for proton migration decreases with the increasing inter-atomic distance between the pentavalent X-ion and the proton. In other words, the H^+-P^{5+} repulsion is larger than the H^+-Nb^{5+} repulsion. The experimental findings are in agreement with reported energy barriers of proton migration in $LaNbO_4$ [28] and $LaPO_4$ [29] based on DFT calculations. The proton trajectories exhibiting the lowest energy barriers for long range proton transport have been reported computationally to be of inter-tetrahedral nature and fairly similar in $LaPO_4$ and $LaAsO_4$ [30]. Due to their resembling structures, an inter-tetrahedral proton conduction path is also believed to dominate for $LaVO_4$, hence comparable pre-exponentials of mobility among the monazite-type materials are expected. Fjeld et al. [28] reported a highly anisotropic inter-tetrahedral rate limiting proton path in $LaNbO_4$ which may explain the lower pre-exponential of proton mobility in $LaNbO_4$ [31] compared to $LaAsO_4$ [30] and $LaVO_4$ (cf. Table 4). The lowest pre-exponential of mobility is found for $LaTaO_4$, however due to structural dissimilarities this value is difficult to compare with the others.

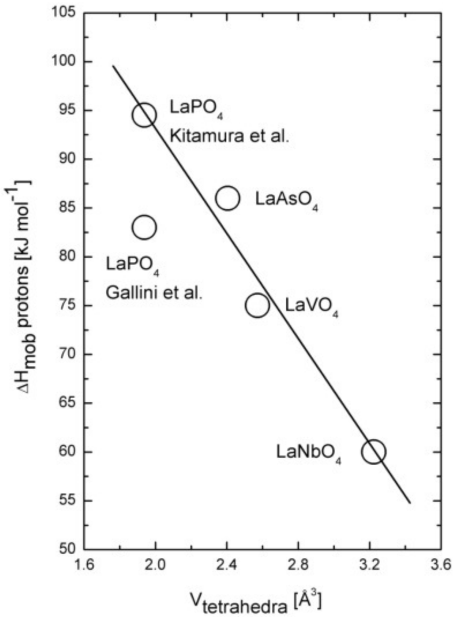

Figure 23 Enthalpy of mobility for protons as a function of tetrahedra XO$_4$volume for acceptor doped LaNbO$_4$ [28], LaVO$_4$, LaAsO$_4$ [30] and LaPO$_4$ [29, 32]. The line is only meant as a guide for the eye.

The partial proton conductivity may according to Nowick and Lee [33] be expressed as an Arrhenius-type equation:

$$\sigma_{H^+}T = \frac{\gamma e^2 \lambda^2 Z \upsilon_0}{k\ V_0}\left[(OH)_O^{\bullet}\right] \exp\left(\frac{\Delta S_{mob,H^+}}{k}\right)\exp\left(-\frac{\Delta H_{mob,H^+}}{kT}\right) = \sigma_{0,H^+} \exp\left(-\frac{\Delta H_{mob,H^+}}{kT}\right)$$

The reference pre-exponentials of proton conductivity, $\sigma_{H^+,0,ref.}$, in Table 5 are calculated according to the former equation and based on the concept of a one-jump rate limiting process with migrating species not affected by trapping [33]. From Table 5 one sees that LaAsO$_4$ has the lowest experimentally determined pre-exponential of conductivity, $\sigma_{H^+,0,exp.}$, followed by LaPO$_4$ whereas LaVO$_4$ shows the highest. Due to their comparable activation energies of conductivity and equal acceptor doping concentrations, the trend in pre-exponential is also reflected in the conductivity as seen in Figure 24. One may speculate whether the lower pre-exponential of proton conductivity in LaAsO$_4$ is due to a slightly more complex migration path involving more steps and therefore less favorable for high proton conductivity than LaVO$_4$. The satisfactory agreement (in the range of $\log\left(\sigma_{0,\exp} / \sigma_{0,\mathrm{ref}}\right) = \pm 0.5$ [33]) between calculated and experimental values of the pre-exponential of conductivity, indicates that protons in LaPO$_4$, LaAsO$_4$ and LaVO$_4$ may be treated as free migrating charge carriers.

Sample density affects the pre-exponential of conductivity, but the reported relative densities among the measured samples are all between 85 and 90 %, a difference too small to account for the observed differences in conductivity

Table 5 Experimental and calculated pre-exponentials of proton conductivity for monazite-type $LaXO_4$ (X = V, As and P).

	Doping	$\sigma_{H^+,0,exp}^{*}$ **(Scm^{-1}K)**	$\sigma_{H^+,0,ref}^{**}$ **(Scm^{-1}K)**	$\log\left(\frac{\sigma_{H^+,0,exp}}{\sigma_{H^+,0,ref}}\right)$	**Ref.**
$LaVO_4$	1 mol% Ca	4709	2420	0.29	This work
$LaAsO_4$	1 mol% Sr	2517	2390	0.02	**[13]**
$LaPO_4$	1 mol% Sr	3586	2310	0.20	**[36]**

* *from linear fit of log(σT) in temperature range where conductivity is dominated by protons.*

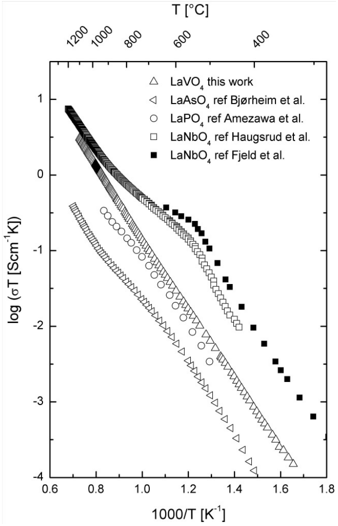

Figure 24 Arrhenius plot of $LaVO_4$ ($p_{H_2O} \approx 0.025$ atm), $LaAsO_4$ ($p_{H_2O} \approx 0.025$ atm) [30] and $LaPO_4$ ($p_{H_2O} \approx 0.041$ atm) [32] compared with data from $LaNbO_4$ ($p_{H_2O} \approx 0.025$ atm) [28, 31] all in oxidizing atmospheres.

3.4. Calsium silicates

The compound $Ca_{3-x}Mg_x(Si_{1-y}Al_yO_4)O_{1-y/2}$. with x=0.07 and y=0.02 was synthesized to compare the results with those of J.M. Porras-Vàzquez *et al.* [4, 5] and A.G. De la Torre *et al.* [6]. Higher aluminum doping contents were also tried in order to increase the oxygen vacancy concentration. The powders were prepared by solid state reaction. The precursors were mixed in ethanol with silica balls overnight, and the mixture was dried and calcined. Different calcination treatments were followed i) 1000°C with 10 hour-dwell, ii) 1200°C for 10 hours followed by 5 hours at 1400°C and iii) 40 hours at 1300°C. The compositions tested are summarized in Table 6 and Table 7. After the calciantion pellets were made by uniaxial pressing followed by sintering at 1500°C for 10 hours. All the temperature ramping was at a rate of 120°Ch^{-1}.

Table 6*: $Ca_{3-x}Mg_x(Si_{1-y}Al_yO_4)O_{1-y/2}$ compositions synthesis during the first synthesis.*

Name	C_3S	$C_3S_{0.2/0.7}$	$C_3S_{0.2/0.5}$	$C_3S_{0.5/0.5}$	$C_3S_{1/0.5}$	$C_3S_{1.5/0.5}$	$C_3S_{0.5/1}$	$C_3S_{1/1}$	$C_3S_{1.5/1}$	$C_3S_{2/1}$	$C_3S_{3/1}$
X	0	0.02	0.02	0.05	0.1	0.15	0.05	0.1	0.15	0.2	0.3
Y	0	0.07	0.05	0.05	0.05	0.05	0.1	0.1	0.1	0.1	0.1

Table 7. ***$Ca_{3-x}Mg_x(Si_{1-y}Al_yO_4)O_{1-y/2}$ compositions synthesis during the first synthesis.***

Name	C_3S	$C_3S_{0.2/0.7}$	$C_3S_{0.15/0.6}$	$C_3S_{0.1/0.4}$	$C_3S_{0.1/0.35}$
x	0	0.02	0.015	0.01	0.01
y	0	0.07	0.06	0.04	0.035

None of the previously describe temperature treatments result in single-phase materials. This was evident from the XRD patterns as illustrated here in Figure 25 for the composition from Table 7 after the second heat-treatment. Another problem with these compounds was that the pellets made for conductivity disintegrated during sintering (cf. Figure 26).

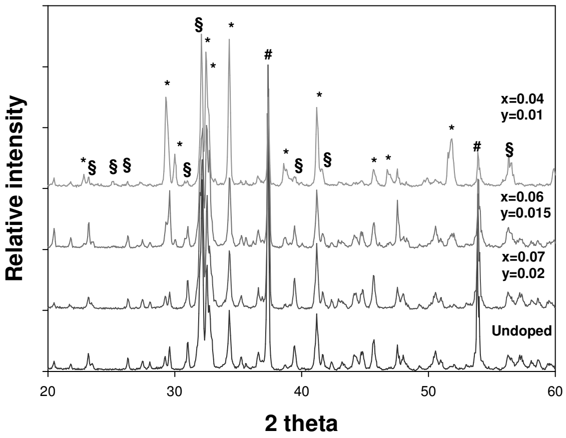

*Figure 25. XRD patterns of $Ca_{3-x}Mg_x(Si_{1-y}Al_yO_4)O_{1-y/2,}$ after second synthesis (1200 and 1400°C). * refers to the C_3S phase, § to C_2S and # to CaO.*

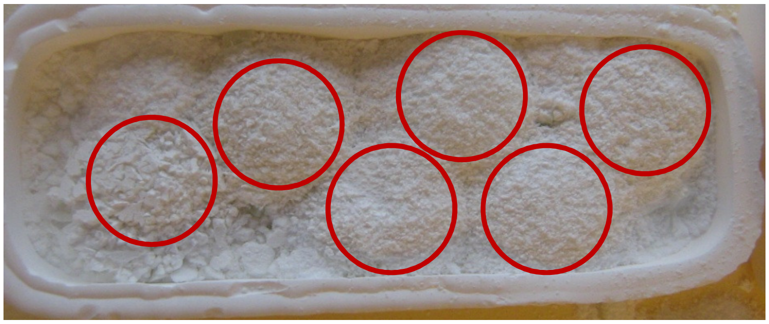

Figure 26. Disintegrated $Ca_{3-x}Mg_x(Si_{1-y}Al_yO_4)O_{1-y/2}$ pellets afer sintering at 1500°C for 10 hours

The disintgration of the pellets can be explained by the presence of C_2S. This compounds present different polymorphs (α, α'$_H$, α'$_L$,β and γ) [34]. Ca^{2+} and SiO_4^{4-} are arranged in a closely similar way for the polymorph α, α'$_H$, α'$_L$ and β. The γ polymorph is far less dense than the others, which results in a dusting phenomenon when cooling. Indeed, the pellet is falling into piece because of the important volume expansion.

Based on all the problems with the formation of secondary phases in the silicates it was decided to stop the attempt to characterize these materials.

3.5. Rare-earth based tungstate materials.

The properties of rare-earth tungstates have been focus for several research projects during the last years and so also for the present project. This is a very interesting family of materials both from a technological and a fundamental point of view. The conductivity characteristics of these materials was revisited by Haugsrud et al [2] in the period 2005-2007 and several interesting features were pointed at. The conductivity behavior of these materials are summarized in Figure 27

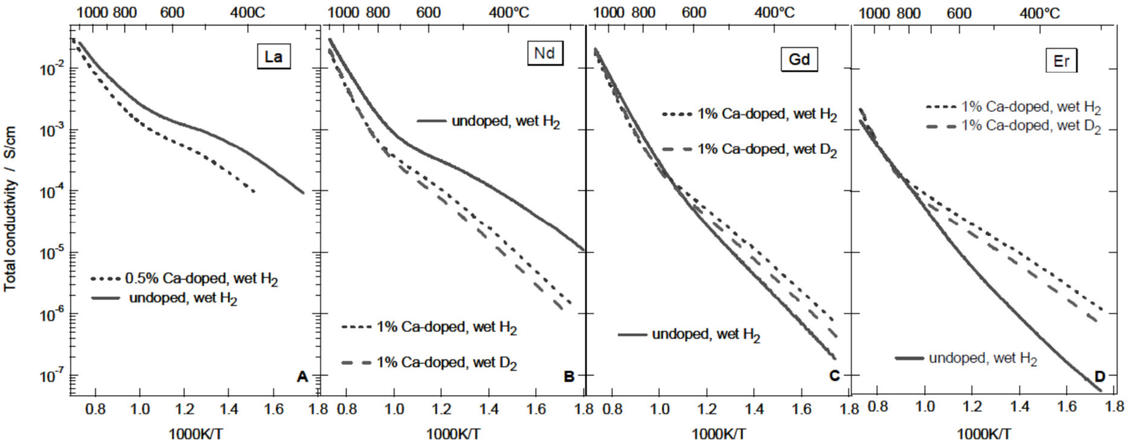

Figure 27. Total ac conductivity (10 kHz) as a function of the 1/T for undoped and Ca- doped, $LnW_{1/6}O_2$, [Ln= La(A), Nd(B), Gd(C), Er(D)] under H_2+2.5% H_2O and D_2+2.5% D_2O atmospheres in the temperature range 300 to 1100°C

There is a clear effect of the H/D isotope shift and conductivity measurements as a function of the water vapor pressure as well as transport number measurements show that protons are the predominating charge carrier in the low temperature range. Interestingly, one should also note from Figure 27 that the conductivity (low temperature region) decreases with the presence of acceptors for the larger rare-earths (La and Nd) whereas for the smaller rare-earths (here Gd and Er) the conductivity behaves as normal - increasing with acceptor substitution. Figure 28 reveals how the different charge carriers vary with temperature under reducing conditions. Clearly the material is a mixed conductor, but with the relatively high and pure proton conductivity below 600°C this material still is interesting as fuel cell electrolyte membranes.

At higher temperature this material has been given promise as a hydrogen gas separation. The hydrogen flux in La_6WO_{12} has been characterized within the framework of the project and is presented in Figure 29 as a function of the inverse temperature. As evident the flux increases with increasing H_2 content in the permeate gas. The flux is also notably higher in wet permeate than in dry permeate and the difference increases with increasing temperature. We believe that this is not due to ambipolar transport of protons and electrons from the feed side to the permeate side, but rather that water in the permeate split and oxide ions diffuses from the permeate to the feed, leaving H_2 in the permeate as an apparent contribution to the flux.

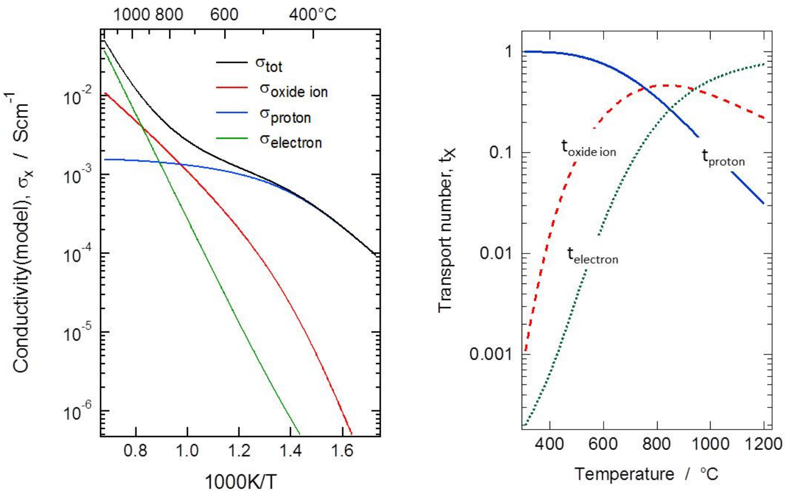

Figure 28 Modeled partial and total conductivities (left) as a function of inverse temperature based on conductivity for La_6WO_{12} under wet H_2. Transport numbers (right) corresponding to the left as a function of temperature.

Some of the important puzzles with the tungstates have been the origin of the hydration and the actual structure and defect structure. As part of the effort to understand these properties of the material, in-situ neutron diffraction studies were initiated at the ISIS beam line in UK. The purpose of the study was to investigate the occupancies in the crystal structure and the whereabouts of the protons.

Figure 30 shows how water affects the unit cell parameter. The two lines approach each other gradually as the material dehydrates with increasing temperature. We are still working on the interpretation of the data and no final conclusion has so far been made.

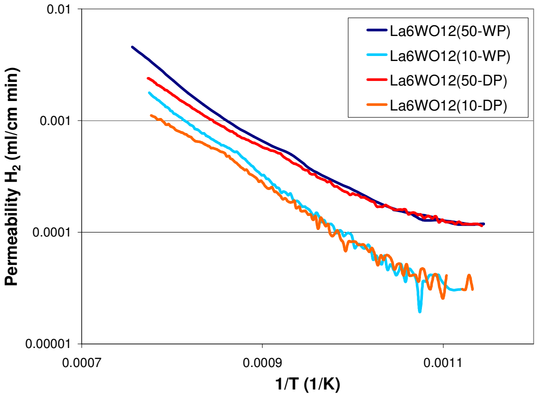

Figure 29, Hydrogen permeability as a function of the inverse absolute temperature measured between 50%H_2-He and 10%H_2-He as feed (wet ~2.5% H_2O) and dry and wet Ar as permeate (DP and WP, respectively)

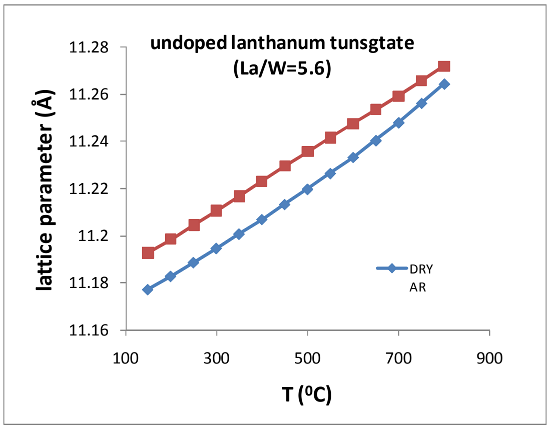

Figure 30. Lattice parameter in lanthanum tungstate with a nominal La/W ratio equal to 5.6. The data are measured under dry and wet (deuterated) Ar.

4. N-INNER - The Non-Science

4.1. The N-INNER project within the PCFC portfolio

The present N-INNER project was one of the first granted project within the portfolio of what eventually was called the Proton Conducting Fuel Cell Package (PCFC package). This is an unofficial cluster of projects with the node at the University of Oslo. The PCFC package consists of several projects funded by the Research Council of Norway and also of the EU project "Efficient and robust fuel cell with novel ceramic proton conducting electrolyte", Effipro. Four out of the five partners in the N-INNER project are partners in Effipro and one may say that the present project was important in initiating the partner consortium for the EU-project.

The different projects in the PCFC cluster was defined so as to focus on the different components of the fuel cell; nanoPCFC electrodes, StackPRO stack design and interconnect, NanIONET the fundamentals of electrode processes, and then finally the N-INNER project with the electrolyte as the central theme. Naturally, this complementary approach has led to many fruitful interactions and a lot of Synergy. The Norwegian projects in the PCFC package have had regular meetings alternating between NTNU, Sintef and UiO. Also the "international" partners were invited to these meetings and updated on progress on the regular internal N-INNER and Effipro meetings. Due to the fact that many of the partners in the international project were the same, two longer joint meetings were organized where the projects had internal meetings, but in addition there were joint sessions focusing on the science and methodologies of the two projects. The initiative of holding these joint meetings certainly increased the knowledge transfer and did "spread the word" of about the N-INNER project and its progress. This also resulted in joint publications across the two projects.

4.2. The N-INNER Symposium on High Temperature Proton and Mixed Proton Electron Conductors for Future Energy Technologies

One aim of the project was to organize a workshop within the theme high temperature proton conductors for future energy technologies. This conference was organized by the coordinator, UiO at Storaas Gjestegård near Kongsberg, from April 12 to 15 2010. The event had approximately 60 attendees mostly from all over Europe. The program of the meeting is included as A5. The event was a great success and was succeeded by the 7th Petite Workshop on the Defect Chemical Nature of Energy Materials in March 2011.

As part of the conference there were also individual meetings for both the N-INNER project and the EU-project EFFIPRO.

4.3. Mobility of researchers

All researchers have been to shorter or longer visits in the one or more of the labs within the consortium. Morten Huse (PhD candidate@UiO) had visits to Risø-DTU and in addition he spent parts of his travel-grant at California Institute of Technology. Sandrine Ricote, (Post doc@Risø-DTU) and Habibur Rhaman (PhD candidate@Chalmers) were both in UiO, and finally, Maryia Ivanova (Pos doc@FZ-Jülich) spent some time at Risø-DTU.

4.4.Relevance to "stakeholders", resources and implementation of the project

In early 2008 the company Protia AS was started in Norway, jointly by the UiO and NTNU as a spin-off with the purpose to commercialize research based on high-temperature proton conductors and mixed proton electron conductors. Focus during the first year(s) was PCFCs based on $LaNbO_4$ electrolytes. Consequently, Protia became an important actor and drive in the progress to develop viable fuel cell technology based on these high temperature proton conductors. Members of Protia have been active also in some of the meetings of the N-INNER. The data and insight from the present project naturally have been important to PCFC efforts of Protia, but perhaps even more so with the present focus of the company more towards chemical membrane reactors based on mixed proton electron conductors.

5. APPENDIX

A1. Dissemination

A1.1. Papers (in total 21)):

New High-Temperature Proton Conductors for Fuel Cells and Gas Separation Membranes
R. Haugsrud, in *Handbook of Fuel Cells* vol. 5 Wiley International (2009), 505-515

Oxygen vacancy ordering within anion-deficient Ceria
S. Hull, S.T. Norberg, I. Ahmed, S.G. Eriksson, D. Marrocchelli, P.A. Madden, Journal of Solid State Chemistry, **182** (2009) 2815

Enhanced sintering and conductivity study of cobalt or nickel doped solid solution of barium cerate and zirconate
S. Ricote, N. Bonanos, Solid State Ionics 181 (2010) 694.

Effect of co-doping on proton conductivity in perovskite oxides $BaZr_{0.9}In_{0.05}M_{0.05}O_{3-\partial}$ (M = Yb^{3+} or Ga^{3+})
I. Ahmed, Seikh M.H. Rahman, P. Steegstra, S. T. Norberg, S.-G. Eriksson, E. Ahlberg, C. S. Knee, and S. Hull, International Journal of Hydrogen Energy, **35** (2010) 6381

Improved Proton Conductivity in Spark-Plasma Sintered Dense Ceramic $BaZr_{0.5}In_{0.5}O_{3-\partial}$
I. Ahmed, F. G. Kinyanjui, P. Steegstra, Z. J. Shen, S. G. Eriksson and M. Nygren, Electrochem. Solid-State Lett., **13** (2010) 130-134

State of the art of ceramic membranes for hydrogen separation
W. A. Meulenberg, M. Ivanova, T. Gestel, M. Bram, H. P.r Buchkremer, D. Stöver, J. M. Serra, in Hydrogen and Fuel Cells, Wiley-VCH Verlag, Weinheim, Edited by Detlef Stolten, ISBN: 978-3-527-32711-9, (2010), pp. 321-349

Proton conducting ceramic membranes: materials and properties
W. A. Meulenberg, M. Ivanova, J. M. Serra, S. Roitsch, *i*n Advanced membrane science and technology for sustainable energy and environmental applications, Part 2 - Membranes for coal and gas power plants and the petrochemical Industry, Editors A. Basile and S. Nunes, ISBN 1 84569 969 6, ISBN-13: 978 1 84569 969 7, Q4 2011

Development of proton conducting SOFCs based on $LaNbO_4$ electrolyte - Status in Norway
A. Magrasó, M.-L. Fontaine, Y. Larring, R. Bredesen, G.E. Syvertsen, H.L. Lein, T. Grande, M. Huse, R. Strandbakke, R. Haugsrud, T. Norby, *Fuel Cells* **11** (2011) 17

Proton conductivity in mixed B-site doped perovskite oxide $BaZr_{0.5}In_{0.25}Yb_{0.25}O_{3-\partial}$
I. Ahmed, F. G. Kinyanjui, Seikh M. H. Rahman, P. Steegstra, S-G. Eriksson and E. Ahlberg, J. Electrochem. Soc. **157** (2010) B1819-B1824

Conductivity, transport number measurements and hydration thermodynamics of $BaCe_{0.2}Zr_{0.7}Y_{(0.1-\xi)}Ni_{\xi}O_{(3-\delta)}$
S. Ricote, N. Bonanos, H.J. Wang, R. Haugsrud, Solid State Ionics 185 (2011) 11.

Proton conductivity in acceptor-doped $LaVO_4$
M. Huse, T. Norby, R. Haugsrud, J. Electrochem. Soc. in print (May 2011)

Conductivity study of dense $BaZr_{0.9}Y_{0.1}O_{3-\delta}$ obtained by spark plasma sintering
S. Ricote, N. Bonanos, H.J. Wang, B.A. Boukamp, accepted Solid State Ionics, special issue SSPC15

Effects of A- and B-site (co-) acceptor doping on the structure and proton conductivity of $LaNbO_4$
M. Ivanova, S. Ricote, W. A. Meulenberg, R. Haugsrud, submitted to Solid State Ionics special issue SSPC15.

Proton conductivity in B-site Ti doped $LaNbO_4$
M. Huse, R. Haugsrud, T. Norby, to be submitted to International Journal of Hydrogen Energy, Proceedings from 7th Petite Workshop on the Defect Chemical Nature of Energy Materials

50 mol% In doped $BaTiO_3$: Characterization of Structure and Conductivity,
Seikh M. H. Rahman, Istaq Ahmed, Christopher S. Knee, Reidar Haugsrud and Sten G. Eriksson, to be submitted to International Journal of Hydrogen Energy, Proceedings from 7th Petite Workshop on the Defect Chemical Nature of Energy Materials

Analysis of the structure of monoclinic and tetragonal $LaNbO_4$ and its relation to proton mobility
M. Huse, A.W.B. Skilbred, M. Karlsson, S.G. Eriksson, T. Norby, R. Haugsrud, C.S. Knee, in manuscript

Electrical conductivity and hydrogen permeation in Ca-doped $La_{0.95}Ni_{2/3}Nb_{1/3}O_{3-\square}$
M. Huse, Y. Larring, M.-L. Fontaine, R. Haugsrud, R. Bredesen, T. Norby, in manuscript

Local and average structure for lanthanum tungstate(La28xW4+xO54+δ). A re-visited model
A. Magraso, J. Polfus, C. Frontera, J. Canales-Vazquez, L.-E. Kalland, S. Islam, S. Erdal, R. Hancke, T.Norby, R. Haugsrud, in manuscript

Improvement of transport properties and hydrogen permeation of proton conducting oxides based on the system $BaZr_{1-(x+0.05)}Y_xMn_{0.05}O_{3-\delta}$
J. M. Serra, S. Escolástico, M. Ivanova, C. Solís, W. A. Meulenberg, S. Roitsch, H. P. Buchkremer, D. Stöver,in preparation

Synthesis and enhanced proton conduction in a 20 mol% ytterbium doped barium zirconate ceramic using Zn as sintering aid
Seikh M. H. Rahman, I. Ahmed and S. G. Eriksson, Accepted The International Conference on Power and Energy Engineering (ICPEE 2011) 29-31, July 2011, Bangkok, Thailand, will be published in" Advanced Materials Research Journal (ISSN: 1022-6680)"

A total scattering and RMC study of 50 mol% In doped $BaTiO_3$
Seikh M. H. Rahman, S. T. Norberg, et al., in manuscript

A1.2. Posters <u>(in total 11):</u>

Solid State Ionics 17 (SSI 17), June 28-July 4 (2009) Toronto, Canada
M. Huse, R. Haugsrud, T. Norby
Proton conductivity in acceptor doped $LaVO_4$

Solid State Ionics 17 (SSI 17), June 28-July 4 (2009) Toronto, Canada
S, Erdal, A, Magrasó, R, Haugsrud, T, Norby
Hydrogen flux in the mixed protonic-electronic conductor La_6WO_{12}

2nd Nordic seminar on Functional Energy Related Materials, NorFERM-2010, Kongsberg, 12.04.10 - 15.04.10, Norway
Seikh M. H. Rahman, I. Ahmed and S.G Eriksson
Zinc as a sintering aid in the Densification and Proton conduction in Ybtterbium doped Barium zirconate ceramic

2nd Nordic seminar on Functional Energy Related Materials, NorFERM-2010, Kongsberg, 12.04.10 - 15.04.10, Norway
M. Huse, R. Haugsrud, T. Norby
Proton conductivity in acceptor doped $LaVO_4$

Solid State Proton Conductor SSPC15, Santa Barbara, USA, August 15-19th 2010
<u>S. Ricote</u>, N. Bonanos, H.J. Wang, B.A. Boukamp
Conductivity study of dense $BaZr_{0.9}Y_{0.1}O_{3-\delta}$ obtained by spark plasma sintering

Solid State Proton Conductors SSPC-15, 15-18 August 2010, Santa Barbara, CA, USA
M. Ivanova, S. Ricote, W. A. Meulenberg, R. Haugsrud, T. Norby,
Conductivity study of A- and B-site (co-)doped $LaNbO_4$

Solid State Proton Conductors SSPC-15, 15-18 August 2010, Santa Barbara, CA, USA
A. Magraso, I. Ahmed, R. Haugsrud,
In-situ high temperature neutron diffraction study of lanthanum tungstate: a proton conductor with a fluorite-type structure.

Solid State Proton Conductors SSPC-15, 15-18 August 2010, Santa Barbara, CA, USA
C. S. Knee, M. Huse, T. Norby, S. G. Eriksson, R. Haugsrud
High flux ND-study of the structural phase transition in $LaNbO_4$

7th International conference on Inorganic Materials, 12-14 September 2010, Biarritz, France
M. Ivanova, S. Ricote, S. Roitsch, D. Sebold, W. A. Meulenberg, J. Mayer,
Influence of the B-site doping element in $La_{0.99}Ca_{0.01}Nb_{0.99}B_{0.01}O_{4-\delta}$ on the conductivity and microstructure

7th International conference on Inorganic Materials, 12-14 September 2010, Biarritz, France
Seikh M. H. Rahman, I. Ahmed, C. S. Knee, R. Haugsrud and S. G. Eriksson,
In doped $BaTiO_3$

Oorganikerdagar, SLU, Uppsala, Sweden. 16-19 June 2010

Seikh M. H. Rahman, S. Eriksson

Zinc as a sintering aid in the Densification and Proton conduction in Ytterbium doped Barium zirconate ceramic

A1.3. Presentations (in total 24):

Solid State Proton Conductors, Sept. 2008, Kyoto, Japan
R. Haugsrud
Thermodynamics and Transport Parameters of Non-Perovskite Structured High-Temperature Proton Conductors

Norwegian Hydrogen Seminar 2008, Sept 2008, Bergen, Norway;
M. Huse, T. Norby, R. Haugsrud
Development of electrolytes for proton conducting solid oxide fuel cells

Norwegian Hydrogen Seminar 2008, Sept 2008, Bergen, Norway;
T. Norby, M. Huse, R. Strandbakke, A. Magrasó, R. Haugsrud
Efficient and stable proton conducting SOFC (PC-SOFC) for hydrogen and reformed fossil fuels

Marie Cürie Actions: NanoMemCourse, March 2009,Norway
R. Haugsrud
Dense Ceramic Proton Conductors for H_2 separation

MRS Conference Proceeding, 13-17 April 2009, San Fransisco, US
I. Ahmed, H. Rahman, E. Ahlberg, S.-G. Eriksson
Proton Conductivity in Co-doped Perovskite Oxide $\mathrm{BaZr_{0.5}In0._{25}Yb_{0.25}O_{3-\delta}}$

Nanomat Conference 2009, June 2009, Lillehammer, Norway
M.L. Fontaine, Y. Larring, S. Mei R. Bredesen, G.E Syvertsen, H. L. Lein, T. Grande, M. Sunding, D.F. Kepatsoglou, S. Diplas, A.E. Gunnæs, O.M. Løvvik, A. Olsen Arne; A. Magraso, A.W.B. Skilbred, era, T. Norby,
Proton Conducting SOFCs – From Fundamental Understanding to Fuel Cell Stacks

E-MRS 2009 fall meeting, Warsaw, Poland September 2009.
S. Ricote, N. Bonanos
Enhanced sintering of cobalt or nickel doped solid solution of barium cerate and zirconate

4th KIFEE Symposium on Environment, Energy, Materials and Education, Sept. 2009, Trondheim Norway
R. Haugsrud
High Temperature Proton Conductors for Future Energy Technologies

3rd European Fuel Cell Technology and Applications Conference EFC09, December 15-18, 2009, Rome,Italy
St. Gibson, M. Ivanova, W. Meulenberg, D. Sebold, Th. Etsell, D. Stöver,
On the preparation and characterization of ceria-based perovskite layers for potential use in proton conducting fuel cells

DKG-Jahrestagung 2010 und Symposium Hochleistungskeramik 2010, 22-24 March 2010, Hermsdorf, Germany
W. A. Meulenberg, M. Ivanova, J. Mayer, S. Roitsch, J. Seeger, J. M. Serra, D. Stöver
Ceramic Proton conductors for application in fuel cells or as gas separation membranes

2nd Nordic seminar on Functional Energy Related Materials, NorFERM-2010, Kongsberg, 12.04.10 - 15.04.10, Norway
M. Huse, T. Norby, R. Haugsrud
Proton conductivity in acceptor doped $LaVO_4$

18th World Hydrogen Conference WHEC 2010, Hydrogen Separation Membranes, 16-21 May 2010, Essen, Germany
W. A. Meulenberg, M. Ivanova, T. Gestel, M. Bram, H. P.r Buchkremer, D. Stöver, J. M. Serra
State of the art of ceramic membranes for hydrogen separation

E-MRS 2010, Spring Strasbourg, 07.06.10 - 11.06.10, France
R. Haugsrud
Protons in acceptor doped rare-earth niobates.

Visit School of Mines, Colorado, August 12th 2010
S. Ricote, N. Bonanos, R. Haugsrud
Conductivity and transport number measurements on Co and Ni doped solid solutions of barium cerate and barium zirconate

Solid State Proton Conductors SSPC-15, 15-18 August 2010, Santa Barbara, CA, USA
M. Huse, T. Norby, R. Haugsrud
Proton conductivity in acceptor doped $LaVO_4$

Summer School on Ceramic materials for green chemical production and clean power generation (NASA-OTM and MemBrain), 08-10 September 2010, Valencia, Spain
M. Ivanova, S. Ricote, W. A. Meulenberg, H.-P. Buchkremer, R. Haugsrud, T. Norby, D. Stöver,
Effect of doping on the electrical properties of proton conducting ceramics

3rd Chalmers-ISIS Workshop: Neutron Scattering and Materials for Energy Applications; (22-24 Sep2010)Gothenburg, Sweden
A. Magraso, I. Ahmed, C. Frontera, C. Hervoches, J.M. Polfus, R. Haugsrud,
On the crystal structure of proton conducting lanthanum tungstate.

Structure and hydrogen defects in oxides, (14Dec2010) Oslo, Norway
A. Magrasó, I. Ahmed, C. Frontera, C. Hervoches, J. Polfus, R. Haugsrud,
Structure determination of not-La_6WO_{12}

7th Petite Workshop on the Defect Chemical Nature of Energy Materials 14.03.11 - 17.03.11Kongsberg, Norway
A. Magraso, R. Haugsrud
Defects and transport properties of "La_6WO_{12}"- potentials for application

E-MRS 2011, Spring Nice, 09.05.11 - 14.05.11, France

R. Haugsrud
Proton conductors in Energy Technologies.

Erice, Italy, 02-12 June 2011
Seikh M. H. Rahman
50 mol% Sc doped $BaTiO_3$: characterization of structure and conductivity

Oorgandagar", Stenungsund, Sweden,13-15 June 2011
Seikh M. H. Rahman
Comparison of structure and proton conductivity of 50 mol % In and Sc doped $BaTiO_3$,

Solid State Ionics-18, Warsaw, Poland, July 3-8, 2011
Seikh M. H. Rahman
50 mol% In and Sc doped $BaTiO_3$: Characterization of Structure and Conductivity

International Conference on Power and Energy Engineering (ICPEE 2011), Bangkok, Thailand,29-31, July 2011
Seikh M. H. Rahman
Synthesis and enhanced proton conduction in a 20 mol% ytterbium doped barium zirconate ceramic using Zn as sintering aid

A1.4. PhD and Lic Thesis:

M. Huse (PhD), "**Transport and hydration in acceptor doped proton conducting oxides - effect of proton-acceptor associations**" will be defended on September 13, 2011.

Habibur Rahman (Lic), "**Structure and conducting properties of In and Sc doped $BaTiO_3$**", defence November 2011.

A2. The "In-situ solid state transformation approach"

Doped fluorite-structured compounds were synthesized via the solid state route for the screen printing pastes preparation. Doped perovskite-structured compounds were in parallel synthesized, pressed and sintered (usually into pellets or bars) in order to test for a variety of properties including conductivity and for optimization of the technological parameters of the in-situ solid state transformation route. Due to this relative simplicity of this process, it is ideally suited for testing various perovskite compositions before they are manufactured into membranes for gas separation or for use in solid oxide fuel cells.

A2.1. Doped Ceria Synthesis

A solid state synthesis method was used for production of the doped ceria powders. Nano-sized powders of high-purity raw materials (ceria and dopant oxides, Sigma Aldrich) were mixed in stoichiometric amounts, magnetically stirred and ultrasonically mixed in ethanol. The powders were then dried at 80°C in a vented drying oven and calcined at 1250 °C for 6 hours in air.

To test the dopant solubility in the ceria fluorite matrix, various compositions of doped ceria samples were synthesized. The X-ray powder diffraction showed single phase composition for the most of the Y-Sm and Gd-containing compounds.

A2.2. Perovskite Synthesis

Doped ceria-carbonate method (DCC): The starting materials for this process were the pre-doped ceria powders and $BaCO_3$, $CaCO_3$, or $SrCO_3$. Stoichiometric ratios of these powders were mixed and ball milled in ethanol before being dried at 80°C in a vented oven. The powders were then heat treated in zirconia crucibles for 8 or 16 hours at 1400 °C. This two stage approach was chosen because it was more closely related to the final screen printed layer process. This method of powder synthesis, however, did not lead to the formation of mono-phase perovskite powders.

Mixed Oxide Method (MO): Stoichiometric amounts of ceria, dopant oxide, and carbonate were measured for various compositions. The powders were magnetically stirred, ultrasonically mixed, and ball milled in ethanol. After evaporation of ethanol in a vented drying oven at 80°C, the powders were calcined in zirconia crucibles for 8 hours at 1200°C with a 3 K/min ramp rate.

A2.3. In-situ solid state transformation approach

Generally, the essence of the method consists of a chemical reaction between two layers: an initial layer deposited on top of the substrate and a supplementary layer. Main advantage of this approach is the simultaneous carrying out of a chemical reaction and structural transformation (e.g. fluorite-to-perovskite structure) that actually allows avoiding the targeted material synthesis prior the layer deposition and therefore limits the traditional high thermal treatments of such complex multilayered systems down to maximum 2 steps. Figure 31 illustrates the formation of $BaCeO_3$-layer via this approach.

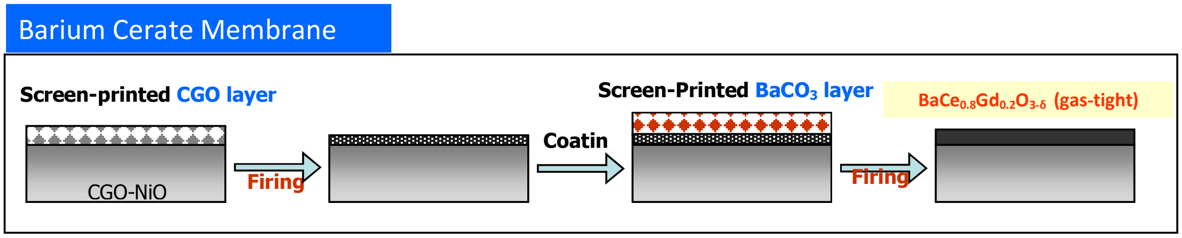

Figure 31. Schematic of a cerate layer formation via the *in-situ* solid state transformation [1,2]

The choice and quality of the substrate and the functional layer(s) might be related to a number of technological difficulties mainly related to the chemical and thermo-mechanical compatibility and stability of the layered structure. Furthermore, the feasible layer thickness obtainable via the method is higher than 10 μm that is limiting in terms of areas of application. The necessity of better experience for optimizing the technological parameters of the approach was however recognized.

A2.4 Material selection

State-of-the art materials with general formula $ACe_{1-x}D_xO_{3-\delta}$ where A stands for Ca, Sr, Ba and D is Sc, Y, Sm, Eu, Gd, Tb as B-site dopant used in amounts of 10, 15, and 20 mol % were at the research focus for multilayered membrane systems development.

A2.5. Substrates Manufacturing

Macroporous substrates were manufacturing by warm-pressing using powders prepared via the Coatmix® procedure [3]. A schematic is presented in Figure 32 illustrating the steps of the technology for powder production.

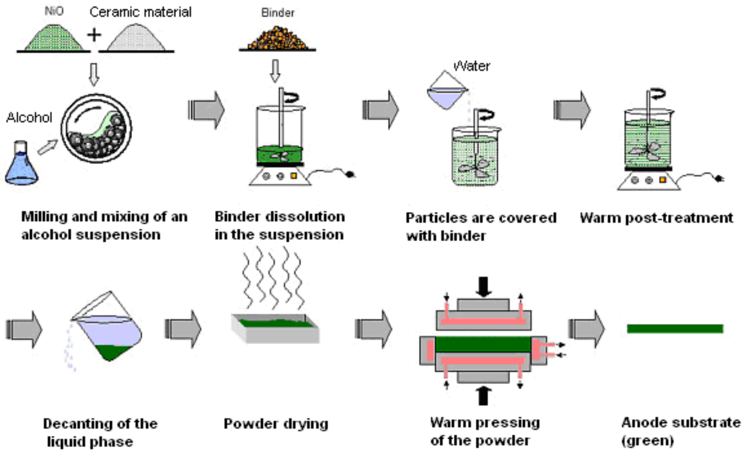

Figure 32. Schematic of the main steps of the Coat-Mix® technology

As substrates NiO-8YSZ cermet was used with a graded porosity and interlayer (or anode functional layer (AFL)) of the same composition with smaller particle sizes (d_{50} ~ 0.2μm).

For the manufacturing of cermet macro porous substrates NiO and ceramic powder were used as starting materials. The agglomerates existing in the NiO powder were destroyed after milling in ethanol and both powders were finely grinded until a homogeneous mud-like alcoholic suspension of the raw materials was obtained. After transfer into the coating container, phenol formaldehyde resin used as a binder was added to the alcoholic suspension and after short heating is was completely dissolved in the alcohol. In the following step acidified water was added slowly and continuously to the mixture. The phenol formaldehyde resin is usually hardly soluble in water and precipitates again until the formation of an insoluble phase. The powder grains were coated with the phenol formaldehyde resin and stick together forming larger agglomerates (Coat mixing). After a subsequent thermal treatment and washing process the precipitation is settled and filtered. The filter cake is transferred on dishes and dried in a vacuum condensation drying furnace at low temperature. The main advantage of this manufacturing method is that with the mixing process no further additives must be used. This leads to well reproducible mixing powders with nearly 100% powder yield.

Powders obtained via the Coat-Mix® technology are easy to process further when sieved below 80 µm. Using warm pressing tool (Figure 33) under low pressure (1MPa) and temperatures above the melting range of the binder (120°C), anode substrates were manufactured.

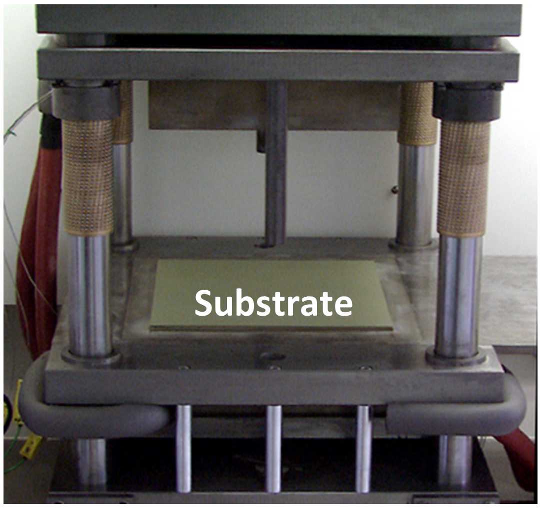

Figure 33. Warm pressing tool used for Coat Mixed substrates manufacturing

The anode functional layer (AFL) was deposited on the pre-sintered substrates (1230°C) by slip-casting (Figure 34) to smooth the surface of substrate.

The substrates manufactured via this method exhibit a homogeneous structure, have the desired pore size and show constant shrinkage behavior after subsequent sintering. Moreover, this manufacturing route has high reproducibility but is time consuming.

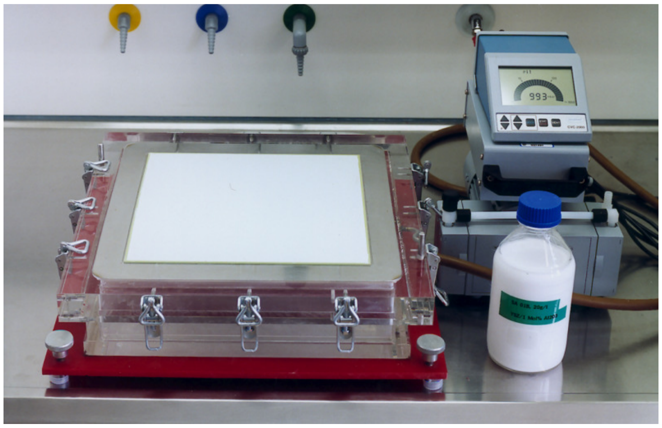

Figure 34. Photograph of the vacuum slip casting facility for manufacturing of the functional layers

A2.6. Paste preparation, screen printing, and in-situ solid state transformation

The screen printing pastes were prepared from the corresponding inorganic powders (CeY10, $BaCO_3$, $SrCO_3$ and $CaCO_3$ powders) with a solution of ethylcellulose (Aldrich) in terpineol (Dupont). Homogeneous fine pastes were achieved by milling of the mixture in a three-roll mill (EXAKT). The binder/solvent solution used was 6% ethylcellulose in terpineol. Binder to powder (B/P) mass ratios and binder to liquid (B/L) volume ratios were adjusted in order to achieve a suitable viscosity for screen printing. Some larger particles and agglomerates were noticed in the carbonate pastes. Compositions of the screen printing pastes are summarized in Table 8.

*Table 8. Prepared Pastes (*B/L = binder/liquid; B/P = binder/powder)*

Paste ID	Powder	Mass	Volume				
		B/L	B/P	Powder	Binder	Solvent	% Powder
Paste 1	$Ce_{0.9}Y_{0.1}O_{2-\delta}$	8.7%	6.8%	56.4%	3.8%	39.7%	14.8%
Paste 2	$BaCO_3$	3.3%	2.5%	57.1%	1.4%	41.4%	22.4%
Paste 3	$SrCO_3$	3.8%	3.5%	52.3%	1.8%	45.8%	22.6%
Paste 4	$CaCO_3$	4.1%	3.5%	54.1%	1.9%	44.0%	27.2%

The pastes were then screen printed onto the substrates using a constant printing speed, squeegee angle and squeegee pressure. 10x10 mm^2 screens with mesh sizes corresponding to printed (wet) thicknesses of 20 and 40 µm were used.

The first layer of $Ce_{0.90}Y_{0.10}O_{1.95}$ (CeY10) paste (Paste 1) was screen printed with a wet thickness of ~20 µm, dried and then sintered at 1300°C for 8 hours. Pastes of $BaCO_3$, $SrCO_3$ and $CaCO_3$ were then deposited as second layers in wet thicknesses of 20 µm or 40 µm, dried and heat treated at either 1300°C or 1400°C for 8 hours.

The NiO-8YSZ substrate screen printed samples and their compositions and synthesis conditions are presented in Table 9.

Table 9. Screen printed samples on NiO-8YSZ substrates

			Layers					
	Substrate		**First**			**Second**		
Sample	**Type**	**Temp.**	**Type**	**Thick.**	**Temp.**	**Type**	**Thick.**	**Temp.**
BCY10-2020-YSZ	NiO-8YSZ	1400°C	$Ce_{0.90}Y_{0.10}O_{1.95}$	20 µm	1300°C	$BaCO_3$	20 µm	1300°C
BCY10-2040-YSZ	NiO-8YSZ	1400°C	$Ce_{0.90}Y_{0.10}O_{1.95}$	20 µm	1300°C	$BaCO_3$	40 µm	1300°C
SCY10-2020-YSZ	NiO-8YSZ	1400°C	$Ce_{0.90}Y_{0.10}O_{1.95}$	20 µm	1300°C	$SrCO_3$	20 µm	1400°C
SCY10-2040-YSZ	NiO-8YSZ	1400°C	$Ce_{0.90}Y_{0.10}O_{1.95}$	20 µm	1300°C	$SrCO_3$	40 µm	1400°C
CCY10-2020-YSZ	NiO-8YSZ	1400°C	$Ce_{0.90}Y_{0.10}O_{1.95}$	20 µm	1300°C	$CaCO_3$	20 µm	1400°C
CCY10-2040-YSZ	NiO-8YSZ	1400°C	$Ce_{0.90}Y_{0.10}O_{1.95}$	20 µm	1300°C	$CaCO_3$	40 µm	1400°C

A.3. Gas mixer

A sketch of the gas mixer is shown in Figure 35. The gas mixer consists of a series of rotameters (Sho-Rate 1355, Brooks Instrument). Under oxidizing atmospheres GAS1 is normally O_2 and GAS2 is Ar. The p_{O_2} is set by repeatedly diluting GAS1 (O_2) with GAS2 (Ar) in three mixing stages (Mix1-Mix3) using the six first flow meters. The lower p_{O_2} -limit is set by the amount of O_2 residuals/impurities in the Ar gas fed to GAS2 and the amount of leakage of air into the gas mixer system, typically $p_{O_2} \sim 1 \cdot 10^{-5}$ atm. The p_{H_2O} in oxidizing atmospheres is set by splitting the gas mixture from Mix3. Here one fraction is bobbled through water saturated by KBr, whereas the other fraction is dried by passing it through a column of P_2O_5. The two gas fractions are then mixed in Mix4 and fed to the measurement cell.

Under reducing conditions GAS1 is normally set to H_2 or HARMIX (5% H_2 in Ar) and GAS2 is set to Ar. The pO_2 of the gas mixture is set by the chemical equilibrium between hydrogen, oxygen and water as expressed below:

$$\tfrac{1}{2}O_2(g) + H_2(g) = H_2O(g) \qquad \text{Eq.4.2}$$

The equilibrium constant for Eq.4.2 varies with temperature and consequently different p_{O_2} are obtained at different temperatures.

$$K_{H_2O} = \frac{p_{H_2O}}{p_{O_2}^{1/2} p_{H_2}} \qquad \text{Eq.4.3}$$

The p_{H_2O} in reducing atmospheres is set by diluting a ~ 2.5 % H_2O-H_2 mixture with dry Ar, in this manner keeping p_{O_2} essentially constant.

Mix5 and Mix6 (flow meters I-L) works in the same manner as Mix3 and Mix 4, however flow meter I may be fed with GAS3 (e.g. H_2) (or gas mixture from Mix4) and diluted by GAS2 (e.g. Ar). By creating a different gas composition with this part of the gas mixer (Mix5 and Mix6), as opposed to the first eight flow meters (Mix1 to Mix4), a gradient in p_{O_2} or p_{H_2O} may be set up across the sample. By sealing a sample to the inner support tube, the chemical gradient may be utilized for e.g. transport number measurements or for fuel cell testing.

By bubbling a gas mixture through water saturated with KBr, the p_{H_2O} is ~ 84% (at 20 °C) of the relative humidity. This results in a p_{H_2O} ~ 0.025 atm at a water bath temperature of 25 °C. Passing an oxidizing gas mixture through a column of P_2O_5 results in a p_{H_2O} ~ $5\cdot 10^{-5}$ atm. By mixing the humidified and dried gas mixtures, the measurement cell may be fed with gas mixtures in the p_{H_2O} range from ~ 0.025 to ~ $5\cdot 10^{-5}$ atm, while keeping p_{O_2} essentially constant. In reducing atmospheres wet H_2 is mixed with Ar, enabling p_{H_2O} in the range from ~ 0.025 to ~ $1\cdot 10^{-3}$ atm, and keeping p_{O_2} essentially constant because the ratio ${p_{H_2}}/{p_{H_2O}}$ is kept constant.

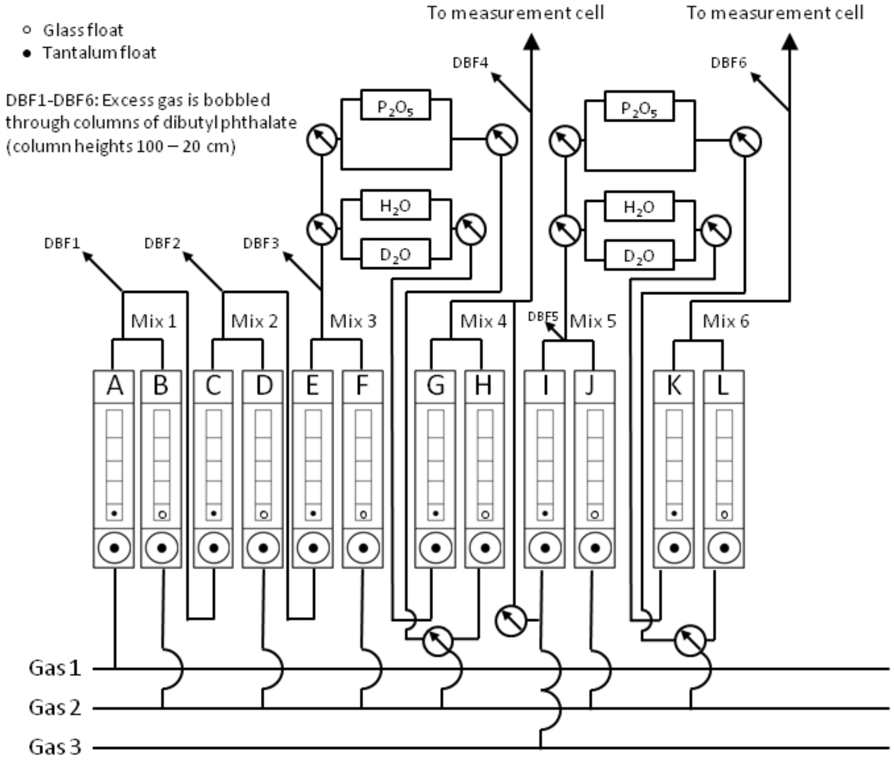

Figure 35. Schematic drawing of gas mixer used during electrical characterisation.

A.4. Results from conductvity characterization and Discussionof thereof, from paper on Ti- and Ca- and Ti codoped $LaNbO_4$

A.4.1. Conductivity of 1 mol% Ti-doped $LaNbO_4$

Electrical characterisation was not performed on the $LaNb_{0.95}Ti_{0.05}O_4$, due to its dual-phase nature.

Figure 36 a) shows total conductivity (10 kHz) vs. 1/T for $LaNb_{0.99}Ti_{0.01}O_4$ from 1100 °C to 350 °C in various atmospheres, and b) shows bulk conductivity from impedance spectroscopy vs. p_{O_2} at 1000, 900 and 800 °C. Figure 36 c) shows bulk conductivity vs. p_{H_2O} in reducing atmosphere at temperatures from 1200 to 700 °C.

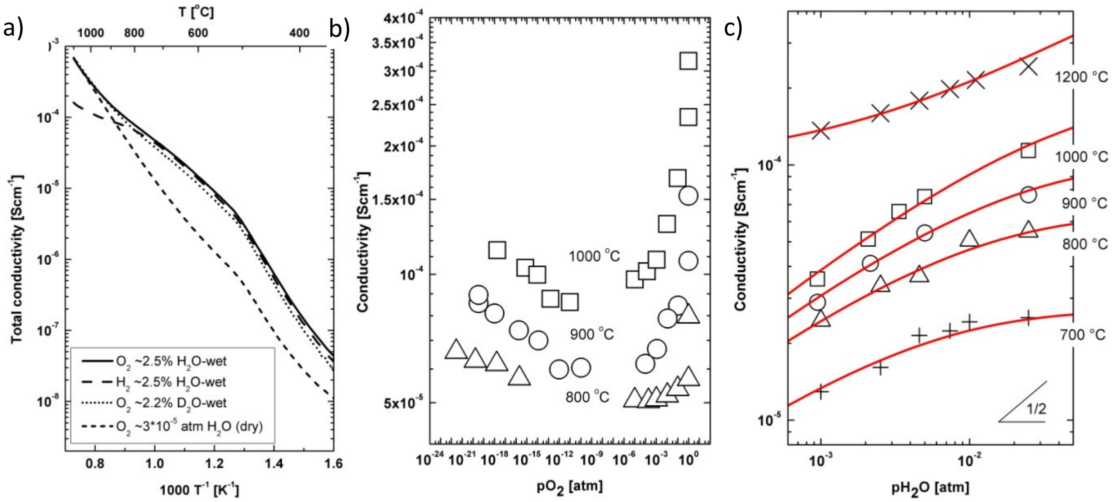

Figure 36 Sample: $LaNb_{0.99}Ti_{0.01}O_4$. a) Conductivity at 10 kHz as a function of 1000/T in H_2O-wet, D_2O-wet and dry O_2 and in H_2O-wet H_2. b) Bulk conductivity as a function of partial pressure of oxygen at 1000, 900 and 800 °C in wet atmospheres. c) Bulk conductivity as a function of partial pressure of water vapour in the temperature range from 1200 °C to 700 °C in reducing atmosphere. Solid lines represent modelled conductivites as a function of p_{H_2O} based on thermodynamic parameters from Table 3.

Generally, $LaNb_{0.99}Ti_{0.01}O_4$ shows mixed electronic and ionic conductivity at high temperatures (T > 750 °C) and dominating ionic conductivity at lower temperatures. Figure 36 a) shows that the conductivity is higher in wet than in dry O_2 atmospheres and that the effect is stronger at low temperatures. The conductivity also increases with increasing p_{H_2O} under reducing conditions, cf. Figure 36 c). At high temperatures the conductivity in wet O_2 is higher than in wet H_2, cf. Figure 36 a). From Figure 36 b) one may see conductivity dependences of p_{O_2} in reducing and oxidising atmospheres indicative of n- and p-type conductivity, respectively. At temperatures below 750 °C the conductivities are equal in wet oxidizing and reducing conditions indicating that the conductivity is independent of p_{O_2} and hence that ionic conductivity predominates. A distinct effect of H/D isotope exchange (difference between σ_{tot} in H_2O and in D_2O-wetted O_2) is observed in the low temperature ionic regime which reveals that protonic conductivity is significant, cf. Figure 36 a).

It is worth noticing from

Figure ***18*** c) that the water vapour dependence on the conductivity levels off towards a p_{H_2O}-independent regime at high water vapour pressures. This reflects that protons change from being minority defects at low p_{H_2O}, to become the majority defect charge compensating the acceptor at high p_{H_2O}. However, at 1200 °C the conductivity exhibits a somewhat different behaviour, being essentially independent of p_{H_2O} at low partial pressures and thereafter increasing gradually with increasing p_{H_2O}. This may be explained by dominating n-type conductivity in both p_{H_2O}-regimes or with possible contributions from oxygen vacancies in the low p_{H_2O}-regime at high temperatures, where both the electron and oxygen vacancy concentrations are independent of p_{H_2O}.One should note that the change in the slope of the conductivity vs. 1/T at approximately 520 °C in

Figure ***18*** a) reflects the 2nd order phase transition, as described previously[35, 36].

A.4.2. Conductivity of Ca- and Ti-doped $LaNbO_4$ (co-doped)

Figure 37a) shows total conductivity (at 10 kHz) vs. 1/T from 1100 °C to 300 °C in wet hydrogen and bulk conductivity from impedance spectroscopy in wet and dry oxygen. Figure 37 b) shows bulk conductivity vs. p_{O_2} at 1000, 900 and 800 °C. Figure 37 c) shows bulk conductivity vs. p_{H_2O} in reducing atmospheres in the temperature range from 1200 to 700 °C.

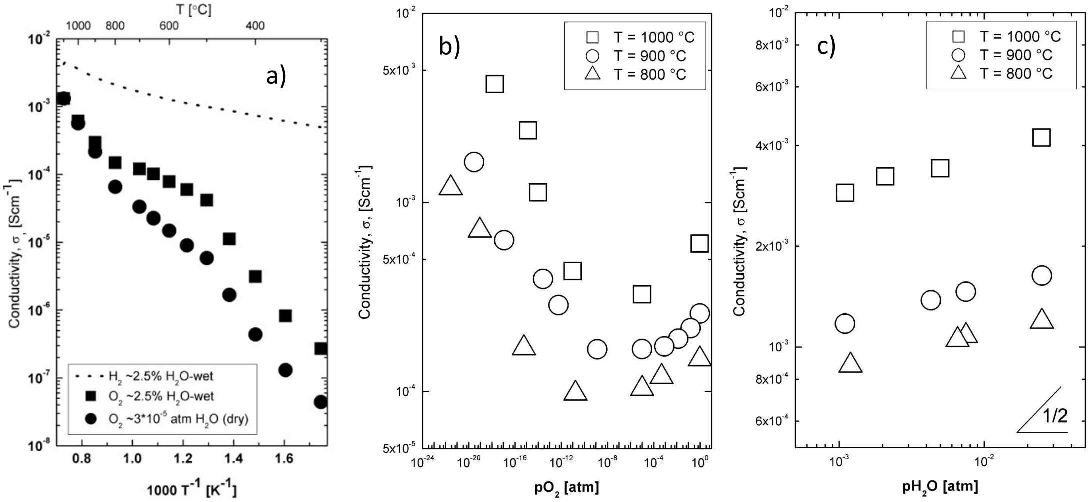

Figure 37 Sample: $La_{0.99}Ca_{0.01}Nb_{0.99}Ti_{0.01}O_4$. a) Conductivity at 10 kHz in H_2O-wet H_2, bulk conductivity deduced from impedance spectroscopy in H_2O-wet O_2 and in dry O_2, all as a function of inverse temperature. b) Conductivity as a function of partial pressure of oxygen in wet atmospheres. c) Conductivity as a function of partial pressure of water vapour in reducing atmosphere.

It is worth highlighting from Figure 37 a) that the conductivity of $La_{0.99}Ca_{0.01}Nb_{0.99}Ti_{0.01}O_4$ is very different in hydrogen and oxygen atmospheres. The behaviour under oxidising conditions is similar to that of $LaNb_{0.99}Ti_{0.01}O_4$. However, under reducing conditions the conductivity is considerably higher, less temperature dependent, and with no indications of the 2nd order phase transition. The dual phase nature of $La_{0.99}Ca_{0.01}Nb_{0.99}Ti_{0.01}O_4$, observed by SEM and XRD, is also reflected in the electrical measurements and indicates that both phases are percolating the sample. Here, the small conductivity dependence on temperature under reducing atmospheres resembles that of $LaNb_3O_9$ [37], where n-type conductivity predominates, and the mixed p-type and proton conductivity in oxidising atmosphere resembles that of $LaNbO_4$.

At a more detailed level one may notice that the conductivity of $La_{0.99}Ca_{0.01}Nb_{0.99}Ti_{0.01}O_4$ is higher in wet hydrogen than in wet and dry oxygen, and that it, at temperatures below 800 °C, is higher in wet than in dry oxygen, cf. Figure 37 a). From Figure 37 b) one may see that $La_{0.99}Ca_{0.01}Nb_{0.99}Ti_{0.01}O_4$ shows mixed electronic (n- and p-type in reducing and oxidising atmospheres, respectively) and ionic conductivity. The conductivity in reducing atmospheres shows a positive p_{H_2O} -dependency, cf. Figure 37 c), which may be explained by mixed n-type and proton conductivity, in agreement with the conductivity behaviour as a function of p_{O_2} , cf. Figure 37b). Under oxidising conditions at high temperatures ($T \geq 800$ °C) p-type conductivity is significant, in accordance with the general observations of p-type conductivity in acceptor doped $LaNbO_4$ under similar conditions [2].

A4.3 Analysis of defects and conductivity in acceptor-doped $LaNbO_4$

The experimental results indicated that acceptor-proton interactions affect the transport properties and hydration thermodynamics of Ti-doped $LaNbO_4$. In the following two sections we will derive expressions for defect concentrations and proton conductivity, following and expanding an approach of Nowick and Lee [33]. Both defect concentrations and conductivity expressions will be solved for two simplified cases for Ti-doped $LaNbO_4$; i) free (non-associated) protons and ii) trapped protons (associated with acceptors).

A4.3.1. Defect concentrations

Substitution with a lower valent cation acceptor introduces an effectively negative charge that must be charge compensated by effectively positive defects, e.g. oxygen vacancies, $v_O^{\bullet\bullet}$. As discussed earlier for *t*-$LaNbO_4$, removing an oxide ion from a tetrahedrally coordinated Nb-ion as a consequence of acceptor doping, results in formation of an oxygen vacancy cluster which can be represented as $(Nb_3O_{11})_{3NbO_4}^{\bullet\bullet}$ [38] or $(Nb_2O_7)_{2NbO_4}^{\bullet\bullet}$ [14]. Substituting Nb^{5+} with Ti^{4+} on the B site in $LaNbO_4$, in absence of H_2O, can then by Kröger-Vink notation using the $(Nb_3O_{11})_{3NbO_4}^{\bullet\bullet}$ representation of the vacancy be expressed as

$$5La_2O_3 + 3Nb_2O_5 + 4TiO_2 = 10La_{La}^{x} + 4(TiO_4)_{NbO_4}^{/} + 2(Nb_3O_{11})_{3NbO_4}^{\bullet\bullet} \qquad \text{Eq.1}$$

where $(TiO_4)_{NbO_4}^{/}$ represents the acceptor dopant (a TiO_4 unit on a NbO_4 site). In wet atmospheres these vacancies may react with water vapour and their positive charge replaced by that of protons in the form of hydroxide ion defects, $(NbO_3OH)_{NbO_4}^{\bullet}$ or, for simplicity, $(HNbO_4)_{NbO_4}^{\bullet}$;

$$H_2O(g) + (Nb_3O_{11})_{3NbO_4}^{\bullet\bullet} = 2(HNbO_4)_{NbO_4}^{\bullet} + (NbO_4)_{NbO_4}^{x} \qquad \text{Eq.2}$$

where $(\mathrm{NbO_4})^x_{\mathrm{NbO_4}}$ is a normal, effectively charge neutral NbO_4 unit. For proton conductors this reaction is exothermic such that low temperatures favour the concentration of protons in the presence of water vapour. The equilibrium constant may be related to the activities of products and reactants as well as the standard Gibbs energy, entropy and enthalpy changes of hydration through

$$K_{\mathrm{hydr}} = \frac{a^2_{(\mathrm{HNbO_4})^{\bullet}_{\mathrm{NbO_4}}} \cdot a_{(\mathrm{NbO_4})^x_{\mathrm{NbO_4}}}}{a_{\mathrm{H_2O}} \cdot a_{(\mathrm{Nb_3O_{11}})^{\bullet\bullet}_{3\mathrm{NbO_4}}}} = \exp\left(-\frac{\Delta G^0_{\mathrm{hydr}}}{RT}\right) = \exp\left(\frac{\Delta S^0_{\mathrm{hydr}}}{R}\right)\exp\left(-\frac{\Delta H^0_{\mathrm{hydr}}}{RT}\right) \qquad \text{Eq.3}$$

By assuming ideal dilute solutions (i.e., non-interacting defects), the activity of a species, a_i, may be equated with its concentration over the standard concentration, here coming out as site fractions, X_i, and partial pressure ratio:

$$K_{\mathrm{hydr}} = \frac{a^2_{(\mathrm{HNbO_4})^{\bullet}_{\mathrm{NbO_4}}} \cdot a_{(\mathrm{NbO_4})^x_{\mathrm{NbO_4}}}}{a_{\mathrm{H_2O}} \cdot a_{(\mathrm{Nb_3O_{11}})^{\bullet\bullet}_{3\mathrm{NbO_4}}}} = \frac{X^2_{(\mathrm{HNbO_4})^{\bullet}_{\mathrm{NbO_4}}} \cdot X_{(\mathrm{NbO_4})^x_{\mathrm{NbO_4}}}}{p_{\mathrm{H_2O}} \cdot X_{(\mathrm{Nb_3O_{11}})^{\bullet\bullet}_{3\mathrm{NbO_4}}}} = \frac{\left(\dfrac{\left[(\mathrm{HNbO_4})^{\bullet}_{\mathrm{NbO_4}}\right]}{\left[(\mathrm{NbO_4})^x_{\mathrm{NbO_4}}\right]}\right)^2 \dfrac{\left[(\mathrm{NbO_4})^x_{\mathrm{NbO_4}}\right]}{\left[(\mathrm{NbO_4})^x_{\mathrm{NbO_4}}\right]}}{\dfrac{p_{\mathrm{H_2O}}}{p^0} \dfrac{\left[(\mathrm{Nb_3O_{11}})^{\bullet\bullet}_{3\mathrm{NbO_4}}\right]}{\left[(\mathrm{NbO_4})^x_{\mathrm{NbO_4}}\right]}} \qquad \text{Eq.4}$$

The individual defect concentrations (represented by square brackets) are thus divided by their respective standard state, here first chosen as the concentration of normal $(\mathrm{NbO_4})^x_{\mathrm{NbO_4}}$ sites, whereas the standard state of partial pressure of water vapour is p^0 = 1 bar. It may be noted that the standard entropy of hydration, as expressed in Eq.4, is of vibrational nature and does not contain configurational entropy of the defects.

Based on detailed information of stable defect sites, from e.g. DFT calculations, and by careful selection of standard states for protons and oxygen vacancies, the contribution from change in configurational entropy of hydration may be estimated. This will be exemplified for Ti-doped $LaNbO_4$ in the following.

The standard concentration of protons in mole fraction may be taken as $N_{\mathrm{H^+}}\left[(\mathrm{NbO_4})^x_{\mathrm{NbO_4}}\right]$, which is the product of the proton site degeneracy and the concentration of NbO_4 units per formula unit. The proton site degeneracy may in turn be expressed as the product of the number of NbO_4 units per NbO_4 site (reason for this seeming triviality will become clearer later), the number of oxygen sites available for protonation per NbO_4 unit, and the number of proton positions available per oxygen site, divided by the number of protons per NbO_4 unit when saturated, as expressed below:

$$N_{\mathrm{H^+}} = \frac{n_{\frac{\mathrm{NbO_4}}{\mathrm{NbO_4}}} \cdot n_{\frac{\mathrm{O}}{\mathrm{NbO_4}}} \cdot n_{\frac{\mathrm{H}}{\mathrm{O}}}}{n_{\frac{\mathrm{H}}{\mathrm{NbO_4}}}} \qquad \text{Eq.5}$$

It is believed that the formation energy of a $\left(H_2NbO_4\right)^-$ unit is substantially greater than for a $\left(HNbO_4\right)^{2-}$ unit and therefore unlikely to be formed in a dilute acceptor doped $LaNbO_4$, hence a NbO_4 unit is saturated by the incorporation of a single proton. Following the arguments above, *t*-$LaNbO_4$ has a proton site degeneracy of N_{H^+} = 8 since all four oxygen sites are identical, each oxygen exhibits two energetically comparable proton sites (only 0.13 eV in energy difference [28]). In contrast, *m*-$LaNbO_4$ has two different oxygen sites per NbO_4 unit (0.41 eV energy difference and an uneven statistical distribution of protons over the two sites is expected). Consequently one may expect a proton site degeneracy of ~ 4 for *m*-$LaNbO_4$.

The standard concentration of oxygen vacancy clusters may be set to $N_{v_O^{\bullet\bullet}}\left[\left(NbO_4\right)^x_{NbO_4}\right]$, where $N_{v_O^{\bullet\bullet}}$ may be expressed as the product of the number of possible oxygen vacancies per NbO_4 unit and the number of orientations the oxygen vacancy cluster can take per NbO_4 unit.

$$N_{v_O^{\bullet\bullet}} = n_{\frac{v_O^{\bullet\bullet}}{NbO_4}} \cdot n_{\frac{O}{NbO_4}} \qquad \text{Eq.6}$$

For *t*-$LaNbO_4$ an oxygen vacancy can be seen as shared by three NbO_4 units, $\frac{\left(Nb_3O_{11}\right)^{\bullet\bullet}_{3NbO_4}}{NbO_4} \rightarrow n_{\frac{v_O^{\bullet\bullet}}{NbO_4}} = \frac{1}{3}$, and the cluster may take four unique orientation, hence $N_{v_O^{\bullet\bullet}}$ = 4/3. In *m*-$LaNbO_4$, the cluster may take two unique orientations and it follows that $N_{v_O^{\bullet\bullet}}$ = 2/3. By expressing the concentrations as mole fractions and assuming that the concentration of oxygen vacancies and protons remain small compared with that of the NbO_4 sites one may set $\left[\left(NbO_4\right)^x_{NbO_4}\right] \approx 1$. The equilibrium constant for hydration may now be expressed in terms of defect concentrations and linked to thermodynamic parameters.

$$K_{hydr} = \frac{\left[\left(HNbO_4\right)^{\bullet}_{NbO_4}\right]^2}{p_{H_2O}\left[\left(Nb_3O_{11}\right)^{\bullet\bullet}_{3NbO_4}\right]\left[\left(NbO_4\right)^x_{NbO_4}\right]} = \exp\left(\frac{\Delta S^0_{hydr} + R\ln\left(\frac{\left(N_{H^+}\right)^2}{N_{v_O^{\bullet\bullet}}}\right)}{R}\right)\exp\left(-\frac{\Delta H^0_{hydr}}{RT}\right) \qquad \text{Eq.7}$$

Here we have introduced a term $R\ln\left(\frac{\left(N_{H^+}\right)^2}{N_{v_O^{\bullet\bullet}}}\right)$ correcting for proton site degeneracy and oxygen vacancy clustering. The entropy contribution from proton site degeneracy and oxide vacancy clustering may on the basis of the above be estimated to +32 and +38 J/mol K for *t*- and *m*-$LaNbO_4$, respectively. The alternative of an oxygen vacancy shared over two NbO_4 units forming $\left(Nb_2O_7\right)^{\bullet\bullet}_{2NbO_4}$, as suggested by Mather et al. [14] gives $n_{\frac{v_O^{\bullet\bullet}}{NbO_4}}$ =1/2, and results in only minor configurational differences with respect to the former case.

A4.3.2. Non-associated defects

Provided that oxygen vacancies and protons are the predominating defects compensating the acceptor, the electroneutrality condition can be approximated as

$$2\left[(Nb_3O_{11})^{\bullet\bullet}_{3NbO_4}\right]+\left[(HNbO_4)^{\bullet}_{NbO_4}\right]=\left[(TiO_4)^{/}_{NbO_4}\right]=[Ti]_0=\text{constant} \qquad \text{Eq.8}$$

Here, all defects are assumed non-associated so that the acceptor concentration, $\left[(TiO_4)^{/}_{NbO_4}\right]$, is equal the nominal Ti-content, $[Ti]_0$. Assuming that the concentrations of oxygen vacancies and protons remain small compared with that of the regular NbO$_4$ concentration, a combination of the expression of the hydration equilibrium constant (Eq.7) with the limiting electroneutrality (Eq.8) yields the following expression for the equilibrium concentration of protons:

$$\left[(HNbO_4)^{\bullet}_{NbO_4}\right]=\frac{\left[(NbO_4)^{x}_{NbO_4}\right]K_{hydr}\,p_{H_2O}\left(-1+\sqrt{1+\dfrac{8\cdot\left[(TiO_4)^{/}_{NbO_4}\right]}{K_{hydr}\,p_{H_2O}\left[(NbO_4)^{x}_{NbO_4}\right]}}\right)}{4} \qquad \text{Eq.9}$$

Under these conditions, the concentration of electronic charge carriers is proportional to $p_{O_2}{}^{1/4}$ and $p_{O_2}{}^{-1/4}$ for holes (p-type) and electrons (n-type), respectively, whereas ionic charge carriers are independent of p_{O_2} at constant p_{H_2O}. At low p_{H_2O} the acceptor dopant will mainly be compensated by oxygen vacancies, and protons will be a minority defect with a concentration dependency of $p_{H_2O}{}^{1/2}$. At high p_{H_2O} the concentration of protons becomes constant, given by the acceptor dopant, and the oxygen vacancy concentration then follows a $p_{H_2O}{}^{-1}$-dependency. The concentrations of electrons and holes are in this case proportional to $p_{H_2O}{}^{1/2}$ and $p_{H_2O}{}^{-1/2}$, respectively, at constant p_{O_2}.

A4.3.3. Associated defects; proton-acceptor interactions

In analogy with defect association between acceptor dopants and oxygen vacancies, we may expect association between acceptor dopants and oxygen vacancies and/or protons in LaNbO$_4$. Mather et al. has confirmed this and reported stronger interactions with the protons than with the oxygen vacancies, all based on defect pair binding energies calculated with density functional theory (DFT) [14]. Together with the experimental results in this study, this points in the direction of proton-acceptor interactions having a major effect on the conductivity in Ti-doped LaNbO$_4$. In the following section we will therefore derive defect concentrations taking acceptor-proton interactions into account.

The simplest estimate of the enthalpy of association may be obtained from Coulomb interactions between the two charged point defects. In the case of protons as hydroxide defects and Ti dopants we get:

$$\Delta H_{assoc}=\frac{q_{OH_O^{\bullet}}\,q_{Ti_{Nb}^{/}}}{4\pi\,\varepsilon_0\varepsilon\,R_{Ti_{Nb}-OH_O}}=\frac{e\cdot(-e)}{4\pi\,\varepsilon_0\varepsilon\,R_{Ti_{Nb}-OH_O}} \qquad \text{Eq.10}$$

Here $q_{OH_O^\bullet}$ and $q_{Ti_{Nb}^/}$ are the effective charges of the interacting $OH_O^\bullet$ and $Ti_{Nb}^/$, ε₀ is the vacuum permittivity, ε is the relative permittivity of $LaNbO_4$ and R the distance between the interacting defects. It is evident from Eq.10 that the enthalpy of association increases with decreasing distance between the interacting defects; however the expression does not take into account the type of acceptor dopant other than its effective charge. Utilizing DFT, Islam et al. have expressed proton-dopant binding energies ($E_{binding}$) for several proton conducting oxides as the difference between the energy of the cluster ($E_{cluster}$) and the sum of the energies of the corresponding isolated defects [39]:

$$E_{binding} = E_{cluster} - \sum_{component} \left(E_{isolated\,defect}\right) \qquad \text{Eq.11}$$

Negative values of $E_{binding}$, which means that the defect cluster is stable with respect to the isolated defects, have been reported for protons and a number of B site dopants in $LaNbO_4$ [14]. Stable proton-acceptor clusters have also been reported for perovskites in e.g. $BaZrO_3$ [39].

Proton-acceptor associates can be termed $(HTiO_4)_{NbO_4}^x$ and their formation (association) reaction can then be written

$$(HNbO_4)_{NbO_4}^\bullet + (TiO_4)_{NbO_4}^/ = (HTiO_4)_{NbO_4}^x + (NbO_4)_{NbO_4}^x \qquad \text{Eq.12}$$

The mass action equilibrium coefficient, K_{assoc}, of Eq.12 is:

$$K_{assoc} = \frac{\dfrac{\left[(HTiO_4)_{NbO_4}^x\right]}{\left[(NbO_4)_{NbO_4}^x\right]} \cdot \dfrac{\left[(NbO_4)_{NbO_4}^x\right]}{\left[(NbO_4)_{NbO_4}^x\right]}}{\dfrac{\left[(HNbO_4)_{NbO_4}^\bullet\right]}{\left[(NbO_4)_{NbO_4}^x\right]} \cdot \dfrac{\left[(TiO_4)_{NbO_4}^/\right]}{\left[(NbO_4)_{NbO_4}^x\right]}} = \exp\left(\frac{\Delta S_{assoc}^0 + R\ln\left(\dfrac{N_{H^+}}{N_p}\right)}{R}\right)\exp\left(-\frac{\Delta H_{assoc}^0}{RT}\right) \qquad \text{Eq.13}$$

ΔS_{assoc}^0 is the standard entropy of association (normally assumed to be negligible [40]) and ΔH_{assoc}^0 is the standard enthalpy of association. The term $R\ln\left(\frac{N_{H^+}}{N_p}\right)$ takes into account proton degeneracy and defect cluster orientations. Here N_p is the number of defect pair orientations and N_{H^+} has been explained earlier. For proton-acceptor associates in a $HTiO_4$ unit in *t*-$LaNbO_4$, N_p is assumed to be 8, because of the four equivalent oxygen sites per NbO_4 unit and where each oxygen site exhibit two energetically favourable proton sites. *m*-$LaNbO_4$ also exhibits two energetically favourable proton sites per oxygen site, but only two oxygen sites are favourable for protons per NbO_4 unit, hence N_p is assumed to be 4. Provided that oxygen vacancies and free protons are the predominant defects charge compensating the non-associated acceptor concentration, the electroneutrality reads:

$$2\left[(Nb_3O_{11})_{3NbO_4}^{\bullet\bullet}\right] + \left[(HNbO_4)_{NbO_4}^\bullet\right] = \left[(TiO_4)_{NbO_4}^/\right] \qquad \text{Eq.14}$$

The amount of Ti in the system is the sum of associated and non-associated Ti,

$$\left[(\mathrm{HTiO}_4)^{x}_{\mathrm{NbO}_4}\right] + \left[(\mathrm{TiO}_4)^{/}_{\mathrm{NbO}_4}\right] = [\mathrm{Ti}]_0 \qquad \text{Eq.15}$$

where $[\mathrm{Ti}]_0$ is the nominal Ti concentration.

The individual defect concentrations are found by solving the equation set consisting of the electroneutrality (Eq.14), the mass conservation of Ti (Eq.15) and the expressions for equilibrium constants for association (Eq.13) and hydration (Eq.7). The concentration of free mobile protons has a rather lengthy analytical solution and is therefore better expressed as a 3rd order equation as shown below, which can be used to fit parameters to actual measured defect–dependent data sets under given conditions and limitations.

$$\left[(\mathrm{HNbO}_4)^{\bullet}_{\mathrm{NbO}_4}\right]^3 \frac{2K_{\mathrm{assoc}}\,p^0}{K_{\mathrm{hydr}}P_{\mathrm{H_2O}}\left[(\mathrm{NbO}_4)^{x}_{\mathrm{NbO}_4}\right]} + \left[(\mathrm{HNbO}_4)^{\bullet}_{\mathrm{NbO}_4}\right]^2 \frac{\left(K_{\mathrm{assoc}} + \dfrac{2p^0}{P_{\mathrm{H_2O}}K_{\mathrm{hydr}}}\right)}{\left[(\mathrm{NbO}_4)^{x}_{\mathrm{NbO}_4}\right]} + \left[(\mathrm{HNbO}_4)^{\bullet}_{\mathrm{NbO}_4}\right] - [\mathrm{Ti}]_0 = 0$$

Eq.16

After we obtain the concentration of free protons this way, the concentrations of all other defects can be obtained by insertion into the appropriate equations above. The concentration of non-associated acceptors, $\left[(\mathrm{TiO}_4)^{/}_{\mathrm{NbO}_4}\right]$, is expressed through the concentration of mobile protons, the equilibrium constant for association (Eq.13) and the nominal Ti concentration. The concentration of proton-acceptor associates, $\left[(\mathrm{HTiO}_4)^{x}_{\mathrm{NbO}_4}\right]$, is given via the mass balance (Eq.15) and the concentration of vacancy clusters is found by its correlation to non-associated acceptors and mobile protons in the electroneutrality (Eq.14) and when introducing ordinary equilibria between oxygen vacancies, electrons and holes one may finally express the concentrations of electronic minority defects in a similar manner as shown for the case of non-interacting defects.

A4.4. Proton conductivity

A4.4.1. Non-associated defects, middle temperature

At middle temperatures, where the defect concentrations may be assumed to be in equilibrium (not "frozen-in" defect concentrations) and the thermal energy is assumed to be substantially higher than the formation energy of the defect associates, one may regard the protons as free non-interacting charge carriers. Assuming a fully hydrated material, the limiting electroneutrality may then be written:

$$2\left[(\mathrm{Nb_3O_{11}})^{\bullet\bullet}_{3\mathrm{NbO}_4}\right] << \left[(\mathrm{HNbO}_4)^{\bullet}_{\mathrm{NbO}_4}\right] = \left[(\mathrm{TiO}_4)^{/}_{\mathrm{NbO}_4}\right] \qquad \text{Eq.17}$$

The Arrhenius-type conductivity for non-associated protons, $\sigma_{\mathrm{H^+}}\mathrm{T}$, may be expressed as:

$$\sigma_{\mathrm{H^+}}\mathrm{T} = \frac{\gamma e^2\lambda^2 Z\upsilon_0}{k\;V_0}\left[(\mathrm{HNbO}_4)^{\bullet}_{\mathrm{NbO}_4}\right]\exp\left(\frac{\Delta S_{\mathrm{mob,H^+}}}{k}\right)\exp\left(-\frac{\Delta H_{\mathrm{mob,H^+}}}{kT}\right) = \sigma_{0,\mathrm{H^+},\mathrm{non-assoc}}\left[(\mathrm{HNbO}_4)^{\bullet}_{\mathrm{NbO}_4}\right]\cdot\exp\left(-\frac{\Delta H_{\mathrm{mob,H^+}}}{kT}\right)$$

Eq.18

where γ denotes a geometrical factor, λ the effective proton jump distance, Z the number of possible jump directions, υ_0 the attempt frequency, V_0 the molar volume, and T, e and k have their usual meanings. $\Delta S_{mob,H^+}$ and $\Delta H_{mob,H^+}$ are the activation entropy and enthalpy of proton mobility, respectively. Since the concentration of protons is constant given by the dopant concentration, the conductivity has an activation energy E_a given only by the mobility term $\Delta H_{mob,H^+}$. If we compare Eq.18 with a standard Arrhenius expression for conductivity, the effective activation energy, E_a, may be compared with $\Delta H_{mob,H^+}$ in the latter exponential term and the pre-exponential of conductivity may be compared with the product of the remaining parameters excluding the proton concentration, here expressed as $\sigma_{0,H^+,non-assoc}$.

A4.4.2. Associated defects, low temperatures

At low temperatures, where the conductivity is dominated by protons and the thermal energy is low compared to the formation energy of defect associates and, one may assume close to complete association between protons and acceptors, hence

$$\left[(HTiO_4)^{x}_{NbO_4}\right] >> \left[(HNbO_4)^{\bullet}_{NbO_4}\right] \qquad \text{Eq.19}$$

and consequently the Ti mass balance is given by

$$\left[(HTiO_4)^{x}_{NbO_4}\right] \cong [Ti]_0 = \text{constant} \qquad \text{Eq.20}$$

Assuming wet atmospheres, the mobile non-associated protons are charge compensated by non-associated acceptors and consequently the electroneutrality reads

$$\left[(HNbO_4)^{\bullet}_{NbO_4}\right] = \left[(TiO_4)^{/}_{NbO_4}\right] . \qquad \text{Eq.21}$$

Assuming the above, it may be shown that the Arrhenius expression of proton conductivity with complete association reads

$$\sigma_{H^+,assoc} T = \frac{\gamma e^2 \lambda^2 Z \upsilon_0}{k\ V_0} \left(\frac{\left[(HTiO_4)^{x}_{NbO_4}\right]}{N_p} \right)^{1/2} \exp\left(\frac{\Delta S_{mob,H^+}}{k} \right) \exp\left(- \frac{\left(\Delta H_{mob,H^+} + \frac{1}{2}\Delta H_{dissoc}\right)}{kT} \right) \qquad \text{Eq.22}$$

where $\Delta H_{dissoc} = -\Delta H_{assoc}$. The effective activation energy in the low temperature regime may thus represent the sum of the enthalpy of mobility and half of the enthalpy of dissociation.

A4.4.3. Ratio between the pre-exponentials of conductivity for associated and non-associated protons

We have seen that the two cases (free and associated protons) have different activation energies. After this elaborate analysis it is of interest to use the opportunity to look also at the ratio between the pre-exponentials of proton conductivity for the two cases. Comparison between Eqs. 18 and 22 shows that the ratio is simply

As we have seen for non-associated protons, it was assumed that the acceptor dopant was charge compensated by protons and equal the nominal Ti content, $[\mathrm{Ti}]_0$. From the mass balance of Ti in the case of associated protons (Eq.20) we saw that the proton-acceptor cluster concentration was given by the same Ti content, hence the ratio between the associated and non-associated pre-exponentials of conductivity comes out as:

$$\frac{\sigma_{0,\mathrm{H}^+,\mathrm{assoc}}}{\sigma_{0,\mathrm{H}^+,\mathrm{non-assoc}}} = \left(N_p \cdot [\mathrm{Ti}]_0\right)^{-1/2} \qquad \text{Eq.23}$$

Assuming a number of defect pair orientations of 8, an acceptor doping concentration of 1 mol% ($\mathrm{LaNb_{0.99}Ti_{0.01}O_4}$), and keeping all other parameters constant, the theoretical ratio between the two pre-exponentials is a factor of approximately 3.5. This quantifies the higher pre-exponential of conductivity often observed for materials dominated by associated charge carriers compared to isolated (free) charge carriers.

A4.5. Analysis and discussion of conductivity data

We will now analyse the conductivity data of $\mathrm{LaNbO_4}$ in accordance with the models presented above. The parameter set fitted to represent the conductivity behaviour (variations in conductivity with temperature and $p_{\mathrm{H_2O}}$) of $\mathrm{LaNb_{0.99}Ti_{0.01}O_4}$ is presented in Table 10. These data correspond to the high temperature tetragonal structure only, due to the limited temperature window (between 500 and 350 °C) for the monoclinic phase. $N_{v_O^{\bullet\bullet}} = 4/3$, $N_{\mathrm{H}^+} = 8$ and $N_p = 8$ were used in the fitting procedure together with the standard concentration of the individual defects mentioned earlier. For simplicity, the pre-fix emphasising the high temperature polymorph will be omitted and in the following the material is simply addressed as $\mathrm{LaNbO_4}$.

Table 10 Thermodynamic parameters for hydration and mobility of protons in Ti- and Ca-doped $\mathrm{LaNbO_4}$.

$\mathrm{LaNb_{0.99}Ti_{0.01}O_4}$	ΔS^0_{hydr} **[J/mol K]**	ΔH^0_{hydr} **[kJ/mol]**	ΔH^0_{assoc} **[kJ/mol]**	μ_{0,H^+} **[cm^{2}K/Vs]**	$\Delta H_{mob,\mathrm{H}^+}$ **[kJ/mol]**	$\mu_{0,v_O^{\bullet\bullet}}$ **[cm^{2}K/Vs]**	$\Delta H_{mob,v_O^{\bullet\bullet}}$ **[kJ/mol]**
Non-associated defect model *	-143 ± 15	-152 ± 14	N/A	90 ± 5	86 ± 4	1.2 ± 0.5	61 ± 10
Associated defects model **	- 173 ± 8	- 145 ± 5	-65 ± 2	8 ± 2	55 ± 3	2 ± 0.5	60 ± 5
$\mathrm{La_{0.99}Ca_{0.01}NbO_4}$ [2]	-130 ± 10	-115 ± 10	N/A	35 ± 10	55 ± 5	15 ± 5	60 ± 5

* model consisting of non-degenerate non-associated $\mathrm{H^+}$, $\mathrm{O^{2-}}$ and electronic charge carriers.

** model consisting of associated and "free" $\mathrm{H^+}$, $\mathrm{O^{2-}}$ and electronic charge carriers.

Figure 38 shows the measured total conductivities of $\mathrm{LaNb_{0.99}Ti_{0.01}O_4}$ and the partial conductivities generated from the parameters for the associated defects model presented in Table 3, as a function of inverse absolute temperature under a) wet oxidising conditions and b) wet reducing conditions for $\mathrm{LaNbO_4}$.

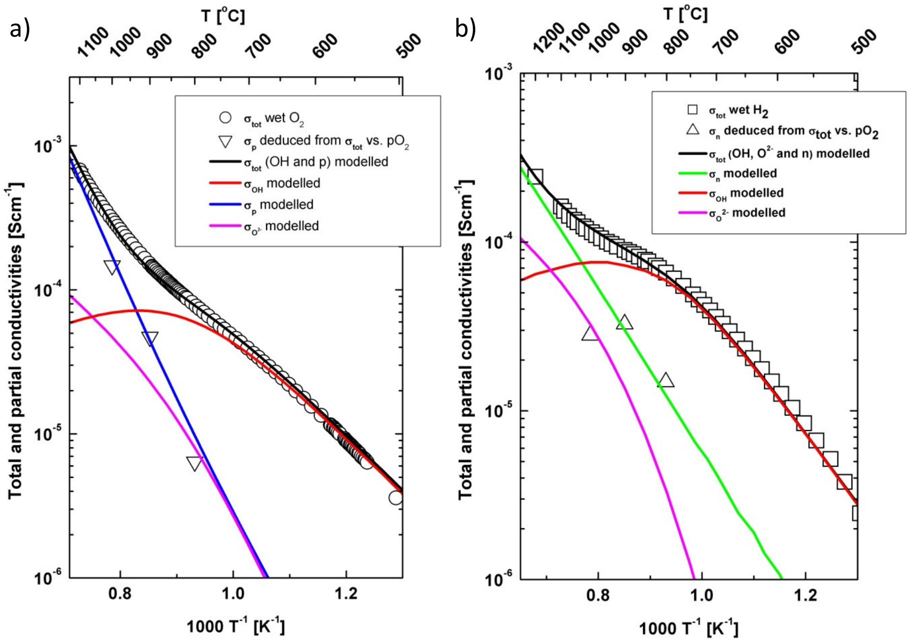

Figure 38 Sample: $LaNb_{0.99}Ti_{0.01}O_4$. Conductivities as a function of inverse absolute temperature. a) In wet O_2: Measured 10 kHz (○) and partial electronic (∇) conductivities. b) In wet H_2: Measured 10 kHz (□) and partial electronic (Δ) conductivities. Modelled total, partial electron, partial proton and partial oxide ion conductivities are represented as lines and generated from thermodynamic and mobility parameters from Table 3.

In order to investigate effects of acceptor doping on the A and/or B site of $LaNbO_4$ Figure 39 compares p_{O_2} -dependences of the conductivity at 800 and 1000 °C for the present $LaNb_{0.99}Ti_{0.01}O_4$ and $La_{0.99}Ca_{0.01}Nb_{0.99}Ti_{0.01}O_4$ with $La_{0.99}Ca_{0.01}NbO_4$ [2] and undoped $LaNbO_4$ [23]. It is evident that the undoped $LaNbO_4$ in all cases exhibits significantly lower conductivity than the acceptor doped versions. $La_{0.99}Ca_{0.01}NbO_4$ has the highest ionic conductivity while under the most reducing conditions the $La_{0.99}Ca_{0.01}Nb_{0.99}Ti_{0.01}O_4$ exhibits a considerable n-type contribution due to a secondary phase of $LaNb_3O_9$. The Ti-doped material, $LaNb_{0.99}Ti_{0.01}O_4$, shows the lowest overall conductivity of the acceptor doped compositions.

Both $La_{0.99}Ca_{0.01}NbO_4$ and $LaNb_{0.99}Ti_{0.01}O_4$ show contributions from hole (p-type) conductivity in oxidising atmospheres at 1000 and 800 °C. For the undoped sample there is a significant contribution of n-type electronic conductivity coming up at low p_{O_2} whereas the Ti- and Ca-doped samples show little and no n-type conductivity. This reflects as expected that the negative acceptor increases the concentration of positive defects and depresses the concentration of electrons. Going in detail on the features of the p_{O_2} -dependence, indications of n-type conductivity at 1000 °C are present in the case of Ti-doping. One may therefore suggest that the multivalent nature of Ti reduces slightly the effective band gap and consequently increases the concentration of electrons. This behaviour is in agreement with the interpretation of the p_{H_2O} dependence at 1200 °C.

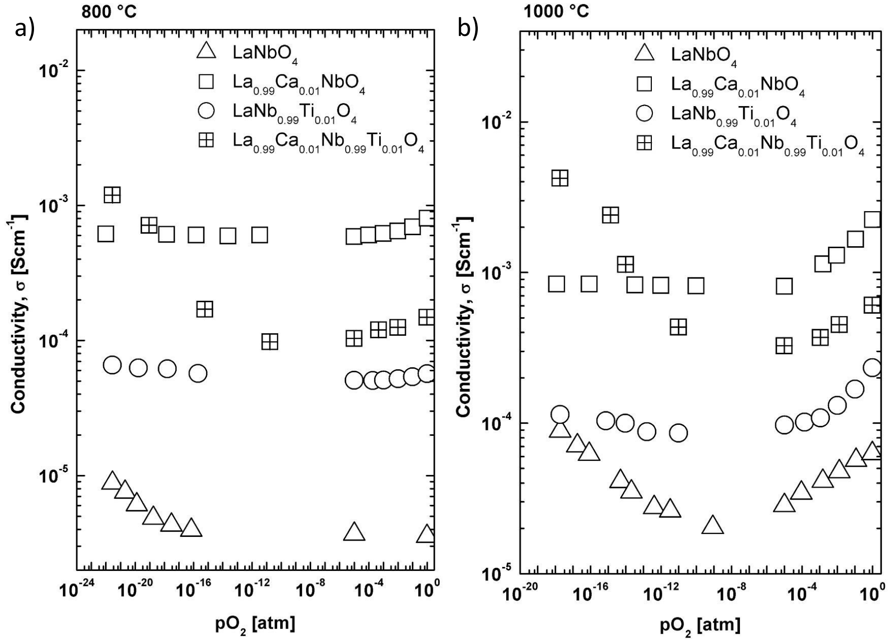

Figure 39 Conductivity as a function of p_{O_2} *in wet atmospheres for* $La_{0.99}Ca_{0.01}NbO_4$*,* $LaNb_{0.99}Ti_{0.01}O_4$*,* $La_{0.99}Ca_{0.01}Nb_{0.99}Ti_{0.01}O_4$ *and undoped* $LaNbO_4$ *at a) 800 °C and b) 1000 °C.*

From a defect chemical viewpoint (cf. Eq.1 and analogously for Ca-doping), it is not obvious that equal acceptor doping concentrations of Ti and Ca in $LaNbO_4$ (e.g. $LaNb_{0.99}Ti_{0.01}O_4$ and $La_{0.99}Ca_{0.01}NbO_4$) should result in a difference in conductivity of approximately one order of magnitude. In principle, a lower solubility for Ti^{4+} than Ca^{2+} in $LaNbO_4$ would explain a difference in proton conductivity, however no segregated secondary Ti-rich phase was detected during microstructural characterization, nor is it likely in this case that a difference in effective acceptor doping level alone can account for the effect on the conductivity.

At any given temperature the equilibrium concentrations of associated and free defects are given by the magnitude of the association enthalpy, as expressed in Eq.13. At sufficiently low temperature, where association may be nearly complete, the total activation enthalpy for conductivity may be expressed as the sum of the enthalpy of mobility and half of the enthalpy of dissociation (Eq.22). Both protons and oxygen vacancies carry effectively positive charge (1+ and 2+, respectively) whereas the acceptor has a negative effective charge. Since both proton-acceptor and oxygen vacancy-acceptor are possible interacting defect pairs in $LaNbO_4$ (due to their respective charges) the binding energy for the individual defect pair is decisive for which that has the greatest degree of interaction. A difference in enthalpy of proton mobility may be seen when comparing the values from the non-associated defect model employed on $LaNb_{0.99}Ti_{0.01}O_4$ with the values for $La_{0.99}Ca_{0.01}NbO_4$ as illustrated in Table 3 (86 ± 4 kJ/mol vs. 55 ± 5 kJ/mol [2]). The enthalpies of oxide ion mobility on the other hand come out equal for the two compositions (60 ± 5 kJ/mol vs. 61 ± 10 kJ/mol). Assuming that A site doped $LaNbO_4$ is not dominated by proton trapping, this indicates that despite the lower effective charge, the acceptor is interacting more with the proton than the oxygen vacancy in $LaNb_{0.99}Ti_{0.01}O_4$. It is believed that the formation of a $(\mathrm{TiNb_3O_{11}})^{\bullet}_{3\mathrm{NbO_4}}$ cluster representing acceptor-vacancy association is energetically unfavourable compared to the one with a proton, due to the high stability and delocalised nature of the $(\mathrm{Nb_3O_{11}})^{\bullet\bullet}_{3\mathrm{NbO_4}}$ cluster. These findings are indeed supported by calculated defect pair binding energies in $LaNbO_4$, where stronger interaction between $\mathrm{OH}^{\bullet}_{\mathrm{O}}$ and $\mathrm{Ti}^{/}_{\mathrm{Nb}}$ than between $\mathrm{v}^{\bullet\bullet}_{\mathrm{O}}$ and $\mathrm{Ti}^{/}_{\mathrm{Nb}}$ are reported in addition to considerably stronger interaction between protons and acceptors in Ti-doped compared to Ca-doped $LaNbO_4$ [14].

Based on the simple expression for coulomb interactions between point defects (Eq.10), an association enthalpy of ~ -40 kJ/mol may be calculated for Ti-doped $LaNbO_4$, compared to ~ -30 kJ/mol for Ca-doping, assuming the same effective charges but different distance between the defects. Hence, the possibility of acceptor-proton interactions in $LaNb_{0.99}Ti_{0.01}O_4$ is higher than in $La_{0.99}Ca_{0.01}NbO_4$ due to the shorter inter-atomic/crystallographic distance between the charge compensating defects. These values are comparable with values calculated for proton "trapping" energies for acceptor dopants in proton conducting perovskites [39]. Although it does not account for the entire increase in enthalpy of mobility observed from $La_{0.99}Ca_{0.01}NbO_4$ to $LaNb_{0.99}Ti_{0.01}O_4$, it suggests that proton–acceptor interactions limit the proton conductivity in Ti-doped $LaNbO_4$ materials.

Assuming an enthalpy of proton mobility equal to that of $La_{0.99}Ca_{0.01}NbO_4$ (55 ± 5 kJ/mol from $La_{0.99}Ca_{0.01}NbO_4$, assumed not to be affected by proton trapping), the higher temperature dependency of the conductivity observed for $LaNb_{0.99}Ti_{0.01}NbO_4$, was accounted for in the associated defects model with an enthalpy of association of -65 kJ/mol. This is because the association enthalpy in the associated defects model affects the effective activation energy of proton conductivity through the concentration of "free" mobile protons.

From Eq.18 and Eq.22, we saw that the difference in apparent activation energy for associated and non-associated proton conductivity is half of the dissociation enthalpy. The disassociation enthalpy, of 65 kJ/mol deduced from the associated defects model, explains nicely the observed difference in apparent activation energy of conductivity of ~ 30 kJ/mol (cf. Table 3) between $La_{0.99}Ca_{0.01}NbO_4$ (non-associated) and $LaNbO_4$ (dominated by proton-acceptor associations). Increased activation energy for proton conductivity has been reported for a number of perovskite-related materials where protons interact with acceptors or other charged defects [41, 42].

A factor ~ 1.6 higher pre-exponential of conductivity is found for B site doped compared to A site doped $LaNbO_4$ (cf. Table 11). This is illustrated in Figure 40 where $La_{0.99}Ca_{0.01}NbO_4$ and $LaNb_{0.99}Ti_{0.01}O_4$ are plotted in the Arrhenius representation. The fact that the pre-exponential of conductivity is higher for $LaNb_{0.99}Ti_{0.01}O_4$, where defect association is affecting the proton conductivity, is expected and in agreement with e.g. Eq.18 and Eq.22. Theoretically the ratio between the pre-exponentials (according to Eq.23) is approximately a factor of 3.5, somewhat higher than what was found experimentally. By employing Eq.23 it is assumed that the conductivity of $La_{0.99}Ca_{0.01}NbO_4$ is not affected by defect association and in the case of $LaNb_{0.99}Ti_{0.01}O_4$ the association has been assumed to be complete. In reality neither of the extremes may be entirely fulfilled and from the experimentally determined ratio of ~ 1.6, one may only conclude that the degree of defect association is relatively higher for $LaNb_{0.99}Ti_{0.01}O_4$ compared to $La_{0.99}Ca_{0.01}NbO_4$.

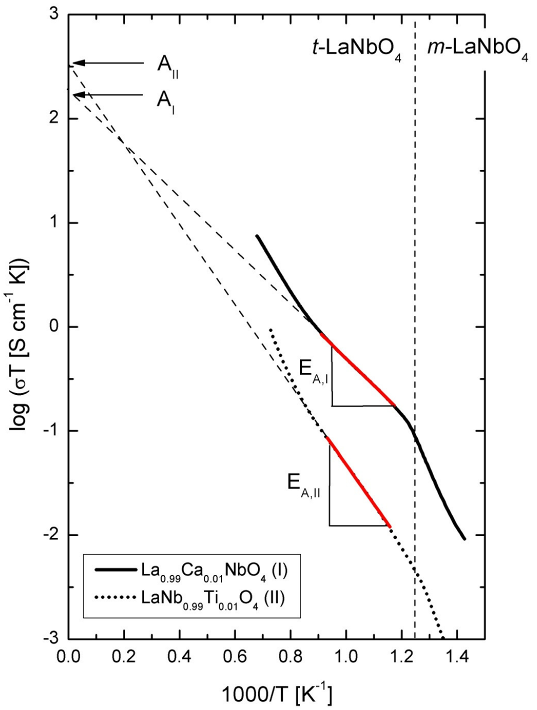

Figure 40 Arrhenius plot of $La_{0.99}Ca_{0.01}NbO_4$ and $LaNb_{0.99}Ti_{0.01}O_4$ in wet O_2. Solid red lines represent linear fits in the temperature region where protons dominate the conductivity. A_I and A_{II} denotes pre-exponential of proton conductivity, and $E_{A,I}$ and $E_{A,II}$ denotes effective activation energy of $La_{0.99}Ca_{0.01}NbO_4$ and $LaNb_{0.99}Ti_{0.01}O_4$, respectively. Dashed lines connecting linear fits and their intercept with 1000/T = 0 are only a guide for the eye.

Table 11 Pre-exponential and activation energy parameters for $LaNb_{0.99}Ti_{0.01}O_4$ and $La_{0.99}Ca_{0.01}NbO_4$.

	$A_{experimental}$ [SK/cm]	$(A_{II}/A_I)_{experimental}$	$(A_{II}/A_I)_{theoretical}$	$E_{A,experimental}$ [kJ/mol]	$E_{A,theoretical}$ [kJ/mol]
$LaNb_{0.99}Ti_{0.01}O_4$	294	1.6	3.5 [a]	78 [c]	86 [b]
$La_{0.99}Ca_{0.01}NbO_4$	184			50 [c]	55 [b]

A_{II} and A_I are the Arrhenius pre-factor of $LaNb_{0.99}Ti_{0.01}O_4$ and $La_{0.99}Ca_{0.01}NbO_4$, respectively.
[a] from Eq.25. [b] based on non-associated model. [c] from slopes in Figure 8.

The pre-exponential term of mobility of B site doped $LaNbO_4$ (cf. Table 11) is a factor of ~ 4 lower than for A site doped. Karlsson et al. report a decrease in the O-H stretch frequency when a proton is in an asymmetric oxygen sublattice (in the vicinity of an acceptor dopant or oxygen vacancy) in $BaZrO_3$ based on IR-measurements and first-principles calculations [43]. This might indicate a reduced attempt frequency and consequently the pre-exponential of mobility in the case of defect associates (e.g. $LaNb_{0.99}Ti_{0.01}O_4$) compared to the non-associated case, as it is expected that the proton migration pathways are not considerably altered. The reported value of ~ 8 cm^2K/Vs in this study is lower than expected for proton conductors based on the vibration frequency of an O-H bond, but one may argue that the high degree of anisotropic conductivity reported by Fjeld et al. in $LaNbO_4$ [28] reduces the effective pre-exponential of proton mobility.

The standard entropy of hydration, ΔS^0_{hydr}, has been discussed in a number of previous publications and is reported between -170 and -90 J/mol K. It is evident that the hydration reaction (Eq.2 and Eq.7) has negative entropies, since one mole H_2O goes from gas to part of the solid. It is however more complex to analyse the magnitude of the entropy change in the two cases ($LaNb_{0.99}Ti_{0.01}O_4$ compared to $La_{0.99}Ca_{0.01}NbO_4$). Analysis of hydration entropy in acceptor doped $BaZrO_3$ both as a function of doping concentration and doping element have not revealed any clear trends [42, 44]. From modelling of the present data set, the standard entropy of hydration of $LaNb_{0.99}Ti_{0.01}O_4$ was found to be -173 ± 8 J/mol K, compared to an apparent entropy of hydration of -130 ± 10 J/mol K for $La_{0.99}Ca_{0.01}NbO_4$ [2]. Taking into account the correction for degeneracy of ~ 32 J/mol K in the former case the two values for standard hydration entropy become comparable. As shown in the expression for the equilibrium constant of hydration (Eq.7), we here propose a way of correcting for degeneracy contributions (possible proton sites vs. saturation and oxygen vacancy clusters) when determining the standard entropy of hydration.

The standard enthalpy of hydration, ΔH^0_{hydr}, has been given much attention in protonics as a measure of the materials' ability to remain hydrated upon heating. For $LaNb_{0.99}Ti_{0.01}O_4$ we have obtained enthalpy of hydration of -145 ± 5 kJ/mol and -152 ± 14 kJ/mol for the associated defects model and non-associated model, respectively. This difference in apparent enthalpy of hydration shows that incorporating acceptor-proton interactions into the model increases the apparent hydration enthalpy, as expected. Comparing the values deduced from the non-associated model, it is interesting to notice that the hydration enthalpy is more negative for $LaNb_{0.99}Ti_{0.01}O_4$ than for $La_{0.99}Ca_{0.01}NbO_4$ (-115 ± 10 kJ/mol) where it is believed that protons are not trapped. This may also be illustrated by comparing the p_{H_2O}-behaviours from 1000 °C and down, where the conductivities of the $LaNb_{0.99}Ti_{0.01}O_4$ level off at high p_{H_2O} whereas a steady slope is observed for $La_{0.99}Ca_{0.01}NbO_4$ [2]. This indicates that the dominance of protons in Ti-doped $LaNbO_4$ sets in at lower p_{H_2O} and remains to higher temperatures than for Ca-doped $LaNbO_4$, in accordance with the expected behaviour of associated vs. non-associated protons [21].

It is expected that if protons are associated with acceptors this will decrease the proton conductivity (through the concentration of free protons) and neutralise the acceptors. The neutralisation of acceptors will in turn also decrease the concentration of oxygen vacancies, however their enthalpy of mobility will remain unchanged, as observed in this study.

The fact that the incorporation of proton-acceptor associations into the model does not account for the entire difference in hydration enthalpy (-145 ± 5 kJ/m vs. -115 ± 10 kJ/mol), suggests that the ratio between the association enthalpy and the enthalpy of proton mobility is not optimal. The enthalpy of proton mobility was set to 55 kJ/mol, from $La_{0.99}Ca_{0.01}NbO_4$ [2], assumed not to be affected by trapping effects. A more negative enthalpy of association combined with a less positive enthalpy of proton mobility will yield similar fits to the conductivity with more comparable values for hydration enthalpy. Hence, the "true" association enthalpy may be expected to be more negative and the "true" enthalpy of proton mobility may be less positive, compared to what reported for $LaNb_{0.99}Ti_{0.01}O_4$ in Table 11. A consequence of the above suggested analysis of lower enthalpy of proton mobility in $LaNbO_4$, is that $La_{0.99}Ca_{0.01}NbO_4$ also to some degree is affected by proton trapping, as also suggested from the analysis of the pre-exponential of mobility.

A5. Program from Symposium

2nd Nordic seminar on Functional Energy Related Materials

NorFERM-2010

N-INNER Symposium on High Temperature Proton and Mixed Proton Electron Conductors for Future Energy Technologies

Monday April 12th		
18:00 – 18:20	**Coffee and refreshments** + **Welcome to NorFERM-2010**	Truls Norby
18:20 – 18:50	High temperature proton conducting solid electrolyte membrane reactors: current experience and perspectives in heterogeneous catalysis and chemical cogeneration	George Marnellos (University of Western Macedonia, Greece)
18:50 – 19:20	Materials science aspects relevant for high-temperature electrochemistry	Tor Grande (NTNU, Norway)
20:00 –	***Dinner followed by social activities***	

Tuesday April 13th			
Session A: Defects and new materials		Chairman: R. Haugsrud	
09:00 – 09:30	A – Tutorial	Self-elimination of doping and defects in cation-disordered oxides	Truls Norby (UiO, Norway)
09:30 – 09:50	A1	Proton conduction in $RE_{5.5}MoO_{12}$ (RE=La, Nd, Gd, Y) compounds	Guilhem Dezanneau (Lab. SPMS, France)
09:50 – 10:10	A2	Hydration of Rutile TiO_2; thermodynamics and Effects on *n*- and *p*-type Electronic Conduction	Skjalg Erdal (UiO, Norway)
10:10 – 10:30	A3	Dynamic DFT study of local structures and proton dynamics in heavily disordered brownmillerite based materials	Karsten Rasim (IMN, France)
10:30 – 10:50	**Coffee and refreshments**		
Session B: $LaNbO_4$		Chairman: T. Grande	
10:50 – 11:10	B1	Proton mobility through a second order phase transition; theoretical and experimental study of lanthanum niobate	Harald Fjeld (UiO, Norway)
11:10 – 11:30	B2	Effect of small offsets in cation stoichiometry in $LaNbO_4$	Guttorm E. Syvertsen (NTNU, Norway)
11:30 – 11:50	B3	Reactivity of lanthanum niobates with nickel oxide	Anna Magrasò (UiO, Norway)

12:00 – 13:00	**Lunch**		
Session C: Electrodes		Chairman: G. Marnellos	
13:00 – 13:30	C – Tutorial	The equivalence of circuits and its relevance to electrical conduction in ceramics	Nikolaos Bonanos (RISØ-DTU, Denmark)
13:30 – 13:50	C1	PC-SOFC cathode characteristics	Ragnar Strandbakke (UiO, Norway)
13:50 – 14:10	C2	Electrochemical properties of PSFC-BCYb composites as cathodes for proton conducting solid oxide fuel cells	Cecilia Solis (CSIC-ITQ, Spain)
14:10 – 14:30	**Coffee and refreshments**		
Electrodes Part II		Chairman G. Dezanneau	
14:30 – 14:50	C3	Electron microscopy study of interfaces of proton conduction fuel cell anodes	Despoina Kepaptsoglou (UiO, Norway)
14:50 – 15:10	C4	Development of oxide cathode materials for SOFCs based on $LaNbO_4$	Vegard Øygarden (NTNU, Norway)
15:10 – 15:30	C5	Surface studies of lanthanum niobate and Ni-$LaNbO_4$ interface model	Kianoosh Hadidi (UiO, Norway)
N-INNER Meeting			
16:00 – 16:10	N-INNER 1	N-INNER - the project	Reidar Haugsrud (UiO, Norway)
16:10 – 16:30	N-INNER 2	Project results Chalmers	Habibur Rahman (Chalmers, Sweden)
16:30 – 16:50	N-INNER 3	Ni doped barium zirconate based system and BZY10 prepared by SPS	Sandrine Ricote (RISØ-DTU, Denmark)
16:50 – 17:10	N-INNER 4	Current status of FZJ activities within N-INNER	Maryia Ivanova (FZ-Jülich, Germany)
17:10 – 17:30	**Coffee and refreshments**		
17:30 – 17:50	N-INNER 5	Hydrogen flux in La_6WO_{12}	Yngve Larring (Sintef, Norway)
17:50 – 18:10	N-INNER 6	Project results UiO	Morten Huse (UiO, Norway)
18:10 – ~18:45	**General Discussion** (N-INNER partners)		

	Wednesday April 14th		
EFFIPRO - 3rd meeting			
09:00 – 09:20	EFFIPRO 1	EFFIPRO management (WP6)	Jørgen Kirksæther

			(UiO, Norway)
09:20 – 10:00	EFFIPRO 2	EFFIPRO introduction and overview	Truls Norby (UiO, Norway)
10:00 – 10:30	EFFIPRO 3	Development of alloy supported proton conducting fuel cells	Marie-Laure Fontaine
10:30 – 11:00	EFFIPRO 4	Review of the proton conductivity of $LaNbO_4$, $LaTaO_4$, $La_2Zr_2O_7$, $LaScO_3$ and La_6WO_{12} class of materials	Christian Kjølseth (UiO, Norway)
11:00 – 11:30	**Coffee and refreshments**		
11:30 – 11:45	EFFIPRO 5	WP 1: Proton conductivity	Reidar Haugsrud (UiO, Norway)
11:45 – 12:00	EFFIPRO 6	WP 2: Precursors and cost	Ruth Astrid Strøm (CerPoTech, Norway)
12:00 – 12:25	EFFIPRO 7	WP 3: Substrate–anode–electrolyte assembly	Nikolaos Bonanos (Risø-DTU, Denmark)
12:25 – 12:45	EFFIPRO 8	WP 4: Novel cathode	Olivier Joubert (IMN, France)
12:45 – 13:05	EFFIPRO 9	WP 5: Kinetics and catalysis	Cecilia Solis (CSIC-ITQ, Spain)
13:05 – 14:30	**Lunch**		
14:30 – 15:30	EFFIPRO 10	Discussion	Truls Norby
15:30 – 16:30	EFFIPRO 11	Discussion with Forum	Truls Norby
16:30 – 17:30	EFFIPRO 12	Board meeting	Rune Bredesen and Jørgen Kirksæther
20:00 –	**Dinner**		

Thursday April 15th			
Session D: Hydrogen permeable membranes		Chairman: Y. Larring	
09:00 – 09:30	D-Tutorial	MEM-BRAIN: Gas separation membranes for zero-emission fossil power plants	Wolfgang Schafbauer (FZ-Jülich, Germany)
09:30 – 09:50	D1	Flux measurement on $LaNbO_4$-$LaNb_3O_9$ ceramic composites	Wen Xing (UiO, Norway)
09:50 – 10:10	D2	Advances in ceramic hydrogen-permeable membranes based on the system Ln_6WO_{12}	Sonia Escolástico (CSIC-ITQ, Spain)
10:10 – 10:30	D3	Hydrogen flux determination using a moisture meter	Henrik Bentzer (RISØ-DTU, Denmark)

10:30 – 10:50	**Coffee and refreshments**		
Session E: Oxygen permeable membranes		Chairman: M. Ivanova	
10:50 – 11:10	E1	Oxygen bulk diffusion and surface exchange in Sr-substituted $La_2NiO_{4+\delta}$	Zuoan Li (UiO, Norway)
11:10 – 11:30	E2	Co and Pr diffusion in $La_{1.9}Sr_{0.1}NiO_{4+\delta}$ and $La_2Ni_{0.8}Cu_{0.2}O_{4+\delta}$ studied by SIMS	Nebojša Čebašek (UiO, Norway)
11:30 – 11:50	E3	An investigation on the oxygen transport properties of $La_{0.2}Sr_{0.8}Fe_{1-x}Ta_xO_{3-\delta}$ (x=0.1 and 0.2)	Ørjan Fossmark Lohne (NTNU, Norway)
11:50 – 12:00	Summary/Concluding remarks		Truls Norby
12:00 – 13:00	**Checkout and lunch**		

Posters:

1. Defects and transport in $Ba_3La(PO_4)_3$

Ragnhild Hancke, Reidar Haugsrud, Truls Norby (UiO, Norway)

2. Protonic conduction in $Sm_{1.92}Ca_{0.08}B_2O_{7-d}$ (B = Ti, Sn, Zr and Ce) pyrochlores and C-type compounds

Karinh Eurenius, Elisabet Ahlberg, Chris Knee (CTH, Sweden)

3. DFT modeling of nitrogen acceptors and imide defects in RE_2O_3 (RE = Sc, Y, La)

Jonathan M. Polfus, Svein Stølen, Truls Norby, Reidar Haugsrud (UiO, Norway)

4. Zinc as a sintering aid in the densification and proton conduction in ytterbium doped barium zirconate ceramic

Habibur Rahman, Istaq Ahmed, Sten Eriksson (CTH, Sweden)

5. Protonic conductivity in non-stoichiometric double perovskite $LaMg_{0,52}Ti_{0,48}O_{3-\delta}$

Camilla Vigen, Truls Norby, Reidar Haugsrud (UiO, Norway)

6. Effect of hydrogen in-diffusion in hydrothermally grown zinc oxide single crystals

Halvard Haug, Bengt Svensson, Truls Norby, Klaus Magnus Johansen (UiO, Norway)

7. Grain boundaries in $BaPr_{0.2}Zr_{0.7}Y_{0.1}O_{3-\delta}$

Kristine Bakkemo Kostøl, Truls Norby, Reidar Haugsrud, Anna Magrasó (UiO, Norway)

8. 'Frozen in' and equilibrium defect structure in acceptor-doped hematite Fe_2O_3

[1]Einar Vøllestad, Truls Norby (UiO, Norway)

9. Metal-oxide interfaces studied by angle-resolved XPS

Martin F. Sunding, Despoina M. Kepaptsoglou, Spyridon Diplas, Truls Norby, Anette E. Gunnæs (UiO, Norway)

10. Determination of hydration enthalpies by TG-DSC

Andreas Løken, Christian Kjølseth, Reidar Haugsrud, Truls Norby (UiO, Norway)

11. Phase segregation in $NiO/LaNbO_4$ composites

Therese S. Stokkan, Anette E. Gunnæs, Despoina M. Kepaptsoglou, Anna Magrasó (UiO, Norway)

12. DFT-modeling of point defects in $TiNb_2O_7$

Liv-Elisif Kalland, Svein Stølen, Truls Norby (UiO, Norway)

13. Fabrication methodology of novel low to intermediate temperature solid oxide fuel cells

Marie-Laure Fontaine, Camilla Haavik, Marit Stange, Yngve Larring, Sen Mei, Paul Inge Dahl, Frode Tyholdt, Rune Bredesen (Sintef, Norway)

14. Electrochemical impedance measurements on nickel doped $SrCe_{0.85}Y_{0.15}O_3$

Henrik K. Bentzer, Nikolaos Bonanos (Risø-DTU, Denmark)

15. Proton conductivity in acceptor-doped lanthanum vanadate

Morten Huse, Truls Norby, Reidar Haugsrud (UiO, Norway)

16. Sandvik Sanergy HT as interconnect material for high temperature proton conducting fuel cells

Anders Werner Bredvei Skilbred, Reidar Haugsrud, Truls Norby (UiO, Norway)

17. PC-SOFC cathode characteristics

Ragnar Strandbakke, Reidar Haugsrud, Truls Norby (UiO, Norway)

X. REFERENCES

---

1 R. Haugsrud, T. Norby *Nature Materials* **5** (2006) 193
2 R. Haugsrud *Solid State Ionics* **178** (2007) 555
3 E. Quarez, S. Noirault, M. T. Caldes, O. Joubert, *J. Power Sources*, **195** (2010) 1136
4 J.M. Porras-Vàzquez, A.G. De la Torre, E.R. Losilla, M.A.G. Aranda, Solid State Ionics 178 (2007) 1073-1080
5 J.M. Porras-Vàzquez, A.G. De la Torre, D. Marrro-Lòpez, E.R. Losilla, M.A.G. Aranda, Dalton Transactions (2006) 2691-2697
6 A.G. De la Torre, R.N. De Vera, A.J.M. Cuberos, M.A.G. Aranda, Cement and Concrete Research 38 (2008) 1261-1269
7 K. Katahira, Y. Kohchi, T. Shimura, H. Iwahara, Solid State Ionics 138 (2000) 91
8 S. Ricote, N. Bonanos, G. Caboche, Solid State Ionics 180 (2009) 990
9 S. Ricote, N. Bonanos, Solid State Ionics 181 (2010) 694
10 A.S. Patnaik, A.V. Virkar, Journal of the Electrochemical Society 153 (7) (2006) A1397
11 M.A. Azimova, S. McIntoch, Solid State Ionics 180 (2009) 160.
12 H. Schmalzried, Solid State Reactions 2nd Ed., (Verlag Chemie, Weinheim 1981).
13 N. Bonanos, K.S. Knight, N. Ellis, Solid State ionics 79 (1995) 161
14 G. C. Mather, C.A.J. Fisher, M. Saiful Islam, Chem. Mater 22 (2010) 5912
15 T. Norby, Solid State Ionics 40/41 (1990) 857
16 K.D. Kreuer, E. Schönherr and J. Maier, Solid State Ionics 70/71 (1994) 278
17 T. Schober, W. Schilling, H. Wenzl, Solid State Ionics 86-88 (1996) 653
18 N. Bonanos, Solid State Ionics 145 (2001) 265
19 R. Haugsrud, B. Ballesteros, M. Lira-Cantú, Truls Norby, J. Electrochem. Soc., 153
20 R. Haugsrud, T. Norby, *Solid State Ionics* **177** (2006) 1129
21 T. Norby, M. Widerøe, R. Glöckner, Y. Larring, *Dalton Trans.* (2004) 3012.
22 R. D. Shannon, Acta Cryst. A32 (1976) 751.
23 T. Mokkelbost, I. Kaus, R. Haugsrud, T. Norby, T. Grande, M.-A. Einarsrud, *J. Am. Ceram. Soc.* **91** (2008) (3) 879.
24 K.D. Kreuer, *Annu. Rev. Mater. Res.* **33** (2003) 333
25 K.D. Kreuer, *Solid State Ionics* **125** (1999) 285
26 K.D. Kreuer, *Solid State Ionics* **97** (1997) 1.
27 S. Gallini, M. Hänsel, T. Norby, M.T. Colomer, J.R. Jurado, *Solid State Ionics* **162-163** (2003) 167
28 H. Fjeld, K. Toyoura, R. Haugsrud, T. Norby, *PCCP* **12** (2010) 10313
29 R. Yu, L.C. De Jonghe, *Journal of Physical Chemistry C* **111** (2007) (29) 11003
30 Bjørheim et al., *to be published*
31 R. Haugsrud, T. Norby, *Solid State Ionics* **177** (2006) 1129
32 N. Kitamura, K. Amezawa, Y. Tomii, N. Yamamoto, *Solid State Ionics* **162– 163** (2003) 161.
33 A.S. Nowick, W.K. Lee, In: A.L. Laskar, S. Chandra, Editors, *Superionic Solids and Solid Electrolytes, resent trends*, Academic Press, Inc., San Diego (1989), p.381-405.
34 Cement and chemistry, H.F.W. Taylor
35 L. Jian, M. Wayman, *J. Am. Ceram. Soc.* **80** (1997) (3) 803.
36 V.S. Stubican, *J. Am. Ceram. Soc.* **47** (1964) 55
37 J. Wood, Defects and Conductivity in Sr-doped LaNb3O9, *Department of Chemistry*, University of Oslo, Oslo. Chap. 5.2.1 p.69 (2007).
38 A. Kuwabara, R. Haugsrud, S. Stølen, T. Norby, *Phys. Chem. Chem. Phys.* **11** (2009) 5550
39 M.S. Islam, P.R. Slater, J.R. Tolchard, T. Dinges, *Dalton transactions* **19** (2004) 3061
40 Y.-M. Chiang, D.P. Birnie, W.D. Kingery, Editors, *Physical Ceramics: Principles for Ceramic Science and Engineering*, Wiley (1996).
41 M.E. Björketun, P.G. Sundell, G. Wahnström, *Phys. rev. B* **76** (2007) (054307)
42 M.E. Björketun, P.G. Sundell, G. Wahnström, *Faraday Discussions* **134** (2006) 247.
43 M. Karlsson, M. Björketun, P.G. Sundell, A. Matic, G. Wahnström, D. Engeberg, L. Börjesson, *Physical Review B* **72** (2005) (094303)
44 K.D. Kreuer, S. Adams, W. Munch, A. Fuchs, U. Klock, J. Maier, *Solid State Ionics* **145** (2001) (1-4) 295.